EXPERIMENTALLY VALIDATED CRYSTAL PLASTICITY MODELING OF TITANIUM ALLOYS AT MULTIPLE LENGTH-SCALES BASED ON MATERIAL CHARACTERIZATION, ACCOUNTING FOR RESIDUAL STRESSES

by

Kartik Kapoor

A Dissertation

Submitted to the Faculty of Purdue University

In Partial Fulfillment of the Requirements for the degree of

Doctor of Philosophy

School of Aeronautics & Astronautics

West Lafayette, Indiana

December 2019

THE PURDUE UNIVERSITY GRADUATE SCHOOL
STATEMENT OF COMMITTEE APPROVAL

Dr. Michael D Sangid, Chair
School of Aeronautics and Astronautics

Dr. Anter El-Azab
School of Material Science and Engineering

Dr. Armand Joseph Beaudoin
University of Illinois at Urbana-Champaign

Dr. Weinong W. Chen
School of Aeronautics and Astronautics

Approved by:

Dr. Weinong W. Chen
Head of the Graduate Program

To my parents and my sister

ACKNOWLEDGMENTS

Firstly, I would like to thank my advisor, Dr. Michael Sangid for his mentoring, guidance and support throughout the course of my graduate studies. His emphasis on producing results, focusing on the bigger picture and helping me realize the relevance of my research has always provided constant motivation to push further. All along my PhD, Dr. Sangid has provided numerous opportunities to present my research at various prestigious conferences throughout the world, which has helped showcase my research to others in the community, as well as meet and network with other researchers in the field. Apart from research, he has always kept an interest in my long-term career goals and offered advice and guidance all along the way. None of this could have been possible without his support and guidance, for which I am extremely thankful.

I would like to acknowledge the funding agencies that provided funding to make all this research possible. Support for this work was primarily provided by DARPA (N66001-14-1-4041) and Pratt & Whitney. Additionally, the high-energy x-ray experiments performed at APS were supported by the US Department of Energy, Office of Science, Office of Basic Energy Sciences (DE-AC02-06CH11357). A special thanks to my committee members Dr. Chen, Dr. El Azab and Dr. Beaudoin for their advice and assistance over these years.

The research I have carried out is heavily based on experimental data provided by our collaborators. I would like to thank our research collaborators at Pratt & Whitney, namely Ryan, Vasisht and Venkat for their great discussions and providing opportunities to share the research with others at Pratt and Whitney. Special thanks to Ryan for always being prompt with any questions I had and helping go through the hurdles of the public release process. I would like to thank Dr. Josh Kacher and Jeremy Yoo at Georgia Tech for collaborating with us and carrying out the TEM imaging. I would like to thank Dr. Todd Book for carrying out characterization of Ti-6Al-4V and for great conversations about Titanium. Thanks to Priya and Diwakar for the data analysis of the X-ray diffraction experiments.

Having a great atmosphere to work is paramount to be productive and successful in graduate school. The collaborative and fun environment existing in our lab has been extremely helpful. A big thank you to Imad, Diwakar, Ajey, Sven, Ronald, Andy, Prithivi, John, Priya, Greg, Ritwik, Saikiran, Noone, Alberto, Bhisham, Michael, Andrea, Steve, Alex, Todd, Sai and Lena.

A couple of years back, I was extremely lucky to be introduced to BJJ by Priya, a sport I since fell in love with. Practicing BJJ has helped me learn lessons that have had a great impact on me as well as my journey through graduate school. Thank you to coach Los and all my teammates at Impactzone for being great friends and always challenging me to become tougher and a better version of myself.

I would like to thank my friends and family: Raj, Shrey, Saumya, Advil, Sree, Tanaya, RnJ and Akhil who were always there whenever I needed them and for motivating and cheering me up during difficult times. A special thanks to Baby Felix and Feline Felix for bringing happiness to our lives, teaching me to be happy with little things and taking my mind off work.

Finally, none of these milestones could have been achieved without the love of my parents and my sister. If not for them, I would not have achieved any of this and any words to describe their sacrifices over the years are insufficient.

TABLE OF CONTENTS

LIST OF TABLES

LIST OF FIGURES

ABBREVIATIONS

ADF	annular dark field
BC	boundary condition
BCC	body center cubic
BOR	burgers orientation relationship
BSE	backscatter electron
CPFE	crystal plasticity based Finite element Modeling
DIC	digital image correlation
EBSD	electron backscatter diffraction
EDM	electron discharge machining
FE	finite element
FIB	focused ion beam
GND	geometrically necessary dislocation
HCP	hexagonal closed pack
HEDM	high-energy diffraction microscopy
HEXD	high-energy x-ray diffraction
HR-DIC	high-resolution digital image correlation
IPF	inverse pole figure
MTR	microtextured regions
PSA	plastic strain accumulation
SEM	scanning electron microcopy
SLM	selective laser melting
STEM	scanning transmission electron microcopy
TEM	transmission electron microcopy
UMAT	user material subroutine
XRD	x-ray diffraction

ABSTRACT

There is a growing need to understand the deformation mechanisms in titanium alloys due to their widespread use in the aerospace industry (especially within gas turbine engines), variation in their properties and performance based on their microstructure, and their tendency to undergo premature failure due to dwell and high cycle fatigue well below their yield strength. Crystal plasticity finite element (CPFE) modeling is a popular computational tool used to understand deformation in these polycrystalline alloys. With the advancement in experimental techniques such as electron backscatter diffraction, digital image correlation (DIC) and high-energy x-ray diffraction, more insights into the microstructure of the material and its deformation process can be attained. This research leverages data from a number of experimental techniques to develop well-informed and calibrated CPFE models for titanium alloys at multiple length-scales and use them to further understand the deformation in these alloys.

The first part of the research utilizes experimental data from high-energy x-ray diffraction microscopy to initialize grain-level residual stresses and capture the correct grain morphology within CPFE simulations. Further, another method to incorporate the effect of grain-level residual stresses via geometrically necessary dislocations obtained from 2D material characterization is developed and implemented within the CPFE framework. Using this approach, grain level information about residual stresses obtained spatially over the region of interest, directly from the EBSD and high-energy x-ray diffraction microscopy, is utilized as an input to the model.

The second part of this research involves calibrating the CPFE model based upon a systematic and detailed optimization routine utilizing experimental data in the form of macroscopic stress-strain curves coupled with lattice strains on different crystallographic planes for the α and β phases, obtained from high energy X-ray diffraction experiments for multiple material pedigrees with varying β volume fractions. This fully calibrated CPFE model is then used to gain a comprehensive understanding of deformation behavior of Ti-6Al-4V, specifically the effect of the relative orientation of the α and β phases within the microstructure.

In the final part of this work, large and highly textured regions, referred to as macrozones or microtextured regions (MTRs), with sizes up to several orders of magnitude larger than that of the individual grains, found in dual phase Titanium alloys are modeled using a reduced order simulation strategy. This is done to overcome the computational challenges associated with

modeling macrozones. The reduced order model is then used to investigate the strain localization within the microstructure and the effect of varying the misorientation tolerance on the localization of plastic strain within the macrozones.

CHAPTER 1. INTRODUCTION

1.1 Overview

Titanium alloys are one of the most widely used alloys in the aerospace industry, especially within the gas turbine engines [1]. Even though these alloys have been in use for decades, their deformation mechanisms and mechanical behavior are still not well understood. There is a lot of variation in their properties and performance based on their microstructure. Time dependent deformation plays a key role in their mechanical behavior, which is seen in their tendency to undergo premature failure due to dwell and high cycle fatigue, well below their yield strength. In addition, along with having inherent anisotropy due to a predominantly HCP crystal structure, a number of different Titanium alloys show varying strain rate sensitivities for the various possible slip systems [2–4]. All these factors have resulted in the need to take a conservative approach during design of critical parts using Titanium alloys, which necessities a more thorough understanding of their deformation mechanics and the development of new suitable tools. Crystal plasticity finite element (CPFE) modeling is a popular computational tool used to understand deformation in these polycrystalline alloys.

With the advancement in experimental techniques such as electron backscatter diffraction (EBSD), digital image (DIC) correlation and x-ray diffraction (XRD), more insights into the microstructure of the material and its deformation process can be attained. This research aims at leveraging data from a number of experimental techniques to develop well-informed and calibrated CPFE models for Titanium alloys, model microstructural features within these alloys at multiple length-scales and gain a comprehensive understanding of their deformation behavior.

1.2 Research contribution

This work builds on to the field of CPFE modeling of Titanium allows by adding the following research contributions:

- Explicitly modeling α and β phases of Ti-6Al-4V and fitting the parameters to multi-scale experiments, to understand the effect of the local orientation of the α and β phases on the material response: The α and β phases of Ti-6Al-4V are modeled explicitly by utilizing different CPFE parameters and slip systems for the two phases with the parameters being

calibrated based on lattice strains measured on different crystallographic planes for both the phases, obtained using high-energy x-ray diffraction (HEXD) experiments coupled with macroscopic stress-strain curves, performed on different pedigrees of Ti-6Al-4V with varying β volume fractions. Using the calibrated models, the effect of the orientation of the α and β phases and their adherence to the BOR (Burgers orientation relationship) on cyclic loading with and without time holds, results in the findings that microstructures following the BOR have the possibility to be more suitable for dwell loading applications compared to microstructures that do not follow the BOR due to higher stress relaxation in the microstructures not following the BOR. However, for cyclic loading with no time holds, the observations from simulations lead to the opposite conclusions, due to localized barriers in the non-BOR microstructures being possible strengthening mechanisms. The consequence of these findings can be used to get a better understanding of what processing route should be chosen in order to tailor the material for specific loading conditions.

- Framework for incorporating residual stresses in CPFE simulations: Due to the lack of methods to incorporate residual stresses into CPFE simulations, two approaches to include residual stresses have been developed and implemented within the CPFE framework.
    - One of the method involves initializing GND densities, calculated using kernel average misorientation (KAM) from the EBSD scans, and the results of this CPFE model are validated with results from the high-resolution digital image correlation (HR-DIC). In this framework, a backstress model is developed based on GND densities, which is more physically realistic and is shown to saturate at a stage that is more representative of the experimentally observed mechanical behavior of the material (contrary to the widely used Armstrong-Frederick model). TEM imaging (carried out by our collaborator Jeremy Yoo) of additively manufactured Ti-6Al-4V shows a higher amount of initial <c+a> dislocations than <a> type dislocations, which is contrary to what is observed in conventional materials and may be attributed to the rapid solidification of the material during additive manufacturing. By using the CPFE simulations initializing GND densities, it is shown that the distribution of initialized GND affects the initial values of backstress and hence the initial hardening, but it does not play a significant role in the evolution of backstress after its saturation.

  - The other is based on the triple decomposition of the deformation gradient (as opposed to the conventional elastic-plastic decomposition in standard CPFE models) with values of grain averaged residual stresses initialized using data from HEDM experiments. The validation of the CPFE simulation is based on comparing the results with the HEDM experiments. This framework was exercised to explore the effects of the true grain morphology, initial residual stress, and physically realistic boundary conditions on the overall reliability of the CPFE predictions.

- Modeling macrozones in Ti-6Al-4V using a reduced order model, calibrated with full-scale CPFE to understand the effect of hard-soft macrozones on the strain localization: Until now, no detailed modeling efforts have been undertaken towards modeling macrozones in Ti alloys. This work takes the first step towards modeling them in industrially relevant Ti-6Al-4V, to better understand the role they play in the material behavior. Due to their large size, the computational challenge posed during their modeling is overcome by establishing a reduced ordered simulation strategy using J2 plasticity coupled with anisotropic elasticity, validated using full-scale CPFE simulations. The reduction in time using the reduced order model compared to full-scale CPFE (from the order of days to run a simulation to hours to run the same microstructural region) is substantial and hence paves the way to model macrozones (which are traditionally considered computationally expensive to model). The results of the reduced order simulations predict high strain localization in the soft macrozone of the hard-soft macrozone combination, suggesting hard-soft macrozone combinations to be potential sites for crack initiation.

CHAPTER 2. LITERATURE REVIEW

2.1 CPFE modeling

Crystal plasticity finite element (CPFE) models have existed for quite some time, with one of the first implementation of crystal plasticity into finite elements (FE) being carried out in the early 1990s by Beaudoin et al. [5] and Kalidindi et al. [6]. Since then, these models have undergone a large number of developments, especially in the past decade. A vast number of models have been developed and used for a wide variety of applications, which have been reviewed by Roters et al. [7]. Broadly speaking, the majority of these applications can be divided into two categories: processing models and models used to understand material behavior. In the case of processing models, most of the literature deals with texture evolution in a number of deformation processes, like in the case of [6,8–11]. On the other hand, there have been a number of CPFE modeling studies to understand material properties and their behavior [12–16]. One of the many notable contributions in this field has been to extend these models to understand fatigue and damage, including predicting fatigue crack initiation in a number of metals and their alloys [17–21]. These models can span from simple phenomenological to more complex ones, like those based on strain gradient approaches [22].

Researchers have improved the representation of the underlying physics of these models [23–25], found new means to identify the CPFE parameters [26–30], incorporated detailed information about the material [31], and used techniques to incorporate exact grain morphologies in CPFE simulations [32–35], in order to get reliable results that match experiments. However, in most of these efforts, three critical pieces of information are often neglected: the effect of initial conditions like residual stresses, the nature of the boundary conditions (BCs) prescribed during the simulations and the representation of the physical microstructure used for the simulations.

2.2 Calibrating and validating CPFE models

Even with a well-informed and physically based CPFE model, experimental validation is essential to completely trust the results of the model. Due to the resolution of DIC being able to capture sub grain level strains, it is an appropriate experimental tool that is used to validate the results of CPFE simulations and a number of studies have done the same. Turner et al. [36]

compare their CPFE results with DIC and observe that their model makes good predictions of surface strains even though the resolution of their DIC experiments is lower than that of the simulations; however the simulations under predict the strain heterogeneity. Lim et al. [37] carry out CPFE simulations on tantalum oligo-crystals, a BCC metal, and compare the results with HR-DIC measurements. They observe good sub-grain level correlation for the heterogeneous strain fields within the material, which may be attributed to the fact that the sample consists of oligo-crystals hence the microstructure is relatively simple and contains very few grains. Tasan et al. [38] use crystal plasticity simulations along with DIC in a dual phase steel sample with a reasonable number of grains to investigate possible sites for damage nucleation near large ferritic grains and low local martensitic fractions and observe a good qualitative match between simulations and experiments. Another comparison in which simulations of a relatively large number of grains are carried out include the one by Mello et al. [39], who utilize a fast Fourier transform based elasto-viscoplastic crystal plasticity formulation to compare the simulations with DIC for a rolled aluminum alloy AA7050-T7451 sample and observe that the statistical nature of the strain fields are well predicted by the simulation but they do not accurately predict the microstructural strain fields when compared grain by grain with the DIC experiments. A number of other studies also focus on comparing surface strains, obtained from digital image correlation (DIC) to those extracted from CPFE simulations [17,36,37,39]. But in order to develop a better and complete understanding of how these models compare with experiments, it is helpful if 3D data, in the form of entire stress or strain tensors is utilized for these comparisons. In recent years, a few studies have utilized high-energy x-ray diffraction microscopy (HEDM) experiments [40–43], which are capable of providing entire tensorial quantities of elastic strains for comparison with simulations [34], [44]. In addition, HEDM can provide complete initial residual stress tensors, which is not possible in the case of DIC.

With the continuous advancement in crystal plasticity modeling approaches, researchers have taken the effort to incorporate more parameters in their models to better capture the physical behavior of the material being modeled [24,25]. Some of the parameters used in the CPFE modeling, like the elastic constants of the material and the strain rate exponents have a direct physical significance and can be determined directly by performing experimental tests. However, there are a number of other constants, specifically in phenomenological CPFE models like the constants used in hardening and backstress equations, which even though have any inherent

physical basis, cannot be measured directly. The only way to obtain these parameters is by fitting them to data obtained from experimental tests, performed on the material. The most widely used method to fit the CPFE parameters involves fitting them to stress-strain curves, which can either be obtained at the polycrystalline (macroscopic) scale [45–47,27,48,49,26,50] or at a lower length scale involving single grains [29,51]. Though using a single stress-strain curve to fit the CPFE parameters is a straightforward way to fit the CPFE parameters, fitting a large set of parameters to a single stress-strain curve does not guarantee a unique solution. Also, in models fit to macroscopic stress-train curves, due to the non-uniqueness of the set of parameters, there is always uncertainty in the simulated quantities [52]. This issue is amplified for the case of multi-phase materials, in which the individual phases have different properties. Bandyopadhyay et al. [52] recognize the inherent uncertainty associated with the mechanical response of the CPFE simulations arising from the uncertainty in the calibration of the CPFE parameters to macroscopic stress-strain curves. They observe variability in the stress along the loading direction, plastic strain accumulation and accumulated plastic strain energy density arising from the variability in the choice of crystal plasticity parameters themselves. This lays the foundation to use a larger experimental data-set consisting of experimentation at multiple length scales to fit the CPFE parameters, because no matter how detailed and physically relevant a CPFE model is, the accuracy of its results is heavily dependent on the choice of the adjustable CPFE parameters selected.

A number of authors talk about fitting CPFE parameters in their models to stress-strain curves [46,47,24,53,25], but there is limited literature that discusses the use of optimization routines to calibrate the parameters from experimental data. One detailed study on fitting CPFE parameters to single crystal nano-indentation experiments has been presented by Chakraborty et al. [29]. They minimize the deviation in the measured and simulated indentation response of individual grains using a Nelder-Mead simplex algorithm and conclude that only one crystal indentation experiment suffices to quantify the two most influential parameters of a phenomenological constitutive plasticity law, using a multi-objective function, which is a combination of the load-displacement response and residual surface topography. However, the CPFE model used in this study has only four constants and hence the scalability to models with larger number of parameters is not known.

Dual phase titanium alloys consist of HCP crystals, which have multiple anisotropic slip systems along with BCC crystals, which have a relatively lower volume fraction. This results in a

large number of CPFE parameters if all the deformation modes in the material are accounted for. Hence, to fit these models, in addition to stress-strain responses, a measurable quantity on different families of crystallographic planes for both the phases of the material is needed to fit the parameters. Though, a number of advanced characterization techniques can be used to get localized information about deformation within the material, e.g. high resolution digital image correlation (HR-DIC) can provide inter and intra-granular strain distribution, which can be used for fitting the CPFE parameters or validate the model [17,39,37,36]. However, it is not possible to get information on individual crystallographic planes on different material phases within the entire sample using HR-DIC. On the other hand, High energy x-ray diffraction (HEXD) is a versatile tool that can fill this gap and provide the material's deformation behavior information in the form of lattice strains on families of crystallographic planes for both the phases in the material [54,55]. Thus, using HEXD experimentation to obtain lattice strains on different crystallographic planes and phases of the material, coupled with macroscopic stress-strain curves for microstructures with varying β volume fraction provides an optimal and complete experimental data set to be used to fit the CPFE parameters in complex two-phase Titanium alloys.

2.3 Boundary conditions in CPFE modeling

It is well known that BCs may have a significant impact on the results obtained from any type of FE simulation. Zhang et al. [33] mention that using an accurate 3D microstructure along with correct BCs, it is possible to estimate the stress tensor in the grains being simulated with some degree of confidence. However, in many studies, the BCs prescribed in a CPFE simulation are generic to describe a microstructure sub-element loaded in uni-axial (uniform) tension. Since most simulations involving comparison with experiments incorporate volumes that are a subset of the actual samples being experimentally tested, it is difficult to extract the exact BCs that will act on the simulation volume. There have been some efforts in this regard by Buljac et al. [56], who propose using digital volume correlation based on 3D synchrotron imaging to extract BCs to be supplied to their FE simulations. Nonetheless, without the assistance of experimental techniques, it is not possible to prescribe the correct BCs to the volume being simulated. This is one of the reasons why a number of simulation studies find the need to impose some sort of simplified BCs and in many cases that may correspond to plane stress or strain.

2.4 Modeling dual phase Titanium alloys

There has been a considerable amount of work done with regard to developing crystal plasticity finite element (CPFE) models for dual phase (α-β) Ti alloys including Ti-6Al-4V. One of the first CPFE models in which slip is idealized and modeled as planar triple slip specifically for the deformation mechanics of Ti-6Al-4V was developed by [57]. The slip idealization involving modeling slip in Ti-6Al-4V as planar triple slip introduces 3 slip systems, 120° from each other to mimic the slip of only the prismatic systems, which are the most active at room temperature in these alloys. This work was then extended into 3D by implementing realistic slip systems for the primary α and the lamellar (α+β) regions by Mayeur et al. [45] and then modified by Zhang et al. [46] and Bridier et al. [47] for cyclic loading and high cycle fatigue. Hasija et al. [27] and Deka et al. [26] also developed models for Ti-6Al and Ti-6242, respectively, which also incorporate slip systems for the primary α and the lamellar (α+β) regions. Dunne et al. [58] developed a physically based CPFE model incorporating GND densities for a HCP material. This concept of incorporating length scale effects using GNDs is adopted in the current paper.

In the studies discussed above, the dual phase (α-β) Ti-alloys are modeled either as an α-Ti single phase material (i.e. neglecting the β due to its low volume fraction) or by utilizing a homogenization scheme, such as [26,45,46], which adds additional slip systems to secondary-α (α + β) regions to account for the β phase utilizing the Burgers orientation relationship (BOR). This is done to keep the model simple and reduce the computational expense. However the possible downside of this approach is that by not explicitly accounting for the β phase, some local microstructural information like strain accumulation and stress anisotropy across the α-β interface may be neglected.

Recently there have been CPFE studies that involve modeling the α and the β phases explicitly and are discussed here in brief. Kasemer et al. [59] model both the α and β phases of Ti-6Al-4V and investigate how the macroscopic properties of the material are affected by incorporating the β-microstructure explicitly into the FE mesh. Zhang et al. [4,60] also model the α and β phases explicitly in their physically based CPFE model for Ti-6242 and utilize this model in conjunction with micro-pillar tests to determine the slip properties of the two phases and then study the effect of local variation in microstructural morphology on strain rate sensitivity and load shedding which is critical for dwell fatigue. Ozturk et al. [61] utilize a fast Fourier transform based elasto-viscoplastic model to analyze the effects of microstructural features on microscopic and

macroscopic behavior of the material for additively manufactured Ti-6Al-4V. Moore et al. [62] analyze the role of the β phase macroscopically in the form of stress-strain responses and microscopically in the form of dislocation densities and hydrostatic stresses for Ti-6Al-4V using crystal plasticity simulations. All of these explicit α-β CPFE models provide a great deal of information about how the β phase affects the properties of these alloys. Except for Zhang et al. [60], these models deal either with a synthetic microstructure or an extremely small realistic microstructure and none of the FE meshing approaches use an actual physically representative mesh for a polycrystal. In addition, the results obtained from these models are not validated with any detailed experimental technique like digital image correlation (DIC) or X-ray diffraction.

2.5 Residual stresses in additively manufactured Ti-6Al-4V

Conventional Ti-6Al-4V can exist in a number of microstructures ranging from a fully equiaxed to a duplex structure depending on the processing route it has undertaken [1]. However in the case of Ti-6Al-4V manufactured using selective laser melting, the fast cooling rate causes a martensitic phase with elongated α grains to form in a lath structure [63]. The nature of additive manufacturing, particularly partial melting and rapid solidification leads to formation of thermal gradients during the manufacturing process which result in an increased presence of residual stresses in the material. These residual stresses can be related to long range stress fields that in turn can be related to the presence of dislocations (specifically geometrically necessary dislocations, GNDs) within the material, implying residual stresses can be related to prior plastic deformation within a given material via GNDs [64].

2.6 Residual stresses and their incorporation into CPFE models

Broadly speaking, residual stress may be classified into three categories based on the length scale in consideration as follows: Type-1, which is generally on the scale of components; type-2, on the grain averaged scale and type-3 at the sub-grain or intra-granular level [65], [66]. This classification of residual stresses across different length scales is illustrated in Fig. 2.1. Most materials have a non-zero value of residual stress due to its processing, handling, and loading history. Even in materials that have been stress relieved or have undergone heat treatment, there will be some amount of residual stress present necessitating the need to initialize residual stresses.

This is true especially in metals and alloys with a HCP crystal structure, as shown by Turner et al. [34], who find that grain level residual stress is not insignificant even in a sample of annealed Ti-7Al. This can be attributed to the fact that the thermal expansion coefficients of the HCP crystal are highly anisotropic [67], hence grain level residual stresses are induced due to thermal expansion and contraction during heat treatment.

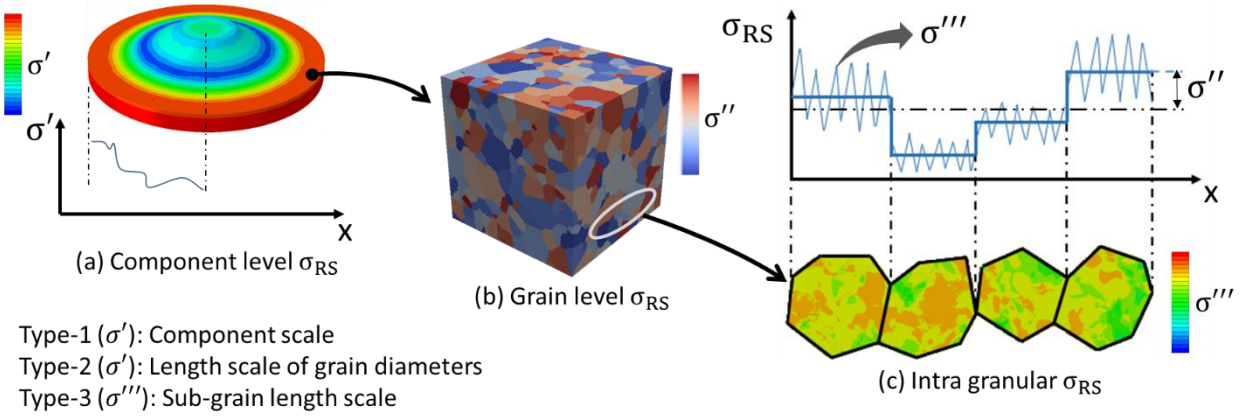

Figure 2.1. Classification of residual stress based on length scale: (a) Variation of residual stresses on a turbine disc at the macroscopic scale; (b) grain by grain variation of residual stress at a point on the disc; (c) variation of residual stress within a set of individual grains (redrawn based on [66])

A number of simulation studies focus on understanding residual stresses and a few even look at incorporating them into CPFE simulations. Turner and Tome [68] utilize an elasto-plastic self-consistent simulation procedure to estimate residual strains in Zircaloy-2 and compare it with neutron diffraction experiments. Musinski and McDowell [69] use an Eigen-strain approach (analogous to thermal deformation) to incorporate residual stresses induced as a result of shot peening. However due to the isotropic nature of these Eigen-strains, only type-1 residual stresses can be incorporated. McNelis et al. [70] introduce a method to estimate the macroscopic residual stress field in a component using high-energy x-ray diffraction experimental data. They utilize a FE framework with an optimization routine to fit the residual stress distribution in a workpiece by ensuring that the macroscopic traction BCs and equilibrium are satisfied, which are treated as constraints in their optimization routine. The objective in their optimization routine is to reduce the difference between the lattice strains obtained from simulations and x-ray diffraction experiments. This optimization technique offers a unique way to estimate the type-1 residual stress

in a material, but the work does not analyze the effect of this initial residual stress on the stress state of the grains during loading. All aforementioned studies provide insights into incorporating residual stresses within simulations, however they do not establish a robust framework to incorporate type-2 residual stresses for a wide variety of conditions. An effort in this direction has recently been made by Pokharel and Lebensohn [71], who propose a method to initialize grain averaged residual stresses in their elasto-viscoplastic fast Fourier transform based crystal plasticity framework. They utilize an Eshelby approximation to get an Eigen-strain field which is then equilibrated using their CP simulations to obtain grain averaged residual stresses. The Eshelby approximation is then modified using a scaling matrix in order to impose residual stresses that match experiments (synthetic experiments in their case). This is a powerful formulation for incorporating residual stresses but cannot be implemented in a commercially available FE code. In more recent work, Chatterjee et al. [2] initialize pre-existing residual stresses in their crystal plasticity simulation of Ti-7Al loaded in tension superposed with bending. In this work, the microstructure is created from HEDM data. The authors incorporate residual stresses by initializing a geometrically necessary dislocation (GND) field in their phenomenological mesoscopic field dislocation mechanics model, which is derived based on the difference in the experimental and simulated bending stresses. They assess the effect of incorporating an initial GND field using two-dimensional manifold learning. Manifold learning is a method of non-linear data-reduction. Using manifold learning, large datasets (stress history of grains in this study) can be reduced to smaller (2D in this study) datasets, making them easy to visualize. This visualization is utilized to compare experiments with simulations. The authors observe that incorporating the initial GND field improves the manifold structure and point distribution (corresponding to the stress history of the grains), indicating improvement in the simulation results compared to the experiments. At this stage, one perceived approach is to simply incorporate residual stress by pre-straining individual grains within the simulation volume. However if this approach is utilized, due to the nature of the FE method, satisfying the equilibrium condition, the residual stresses will relax away. This further strengthens the need for a new formulation to incorporate residual stresses.

It is well known that there is a stress field associated with dislocations present in a material [72]. Since residual stresses generally exist in a material before it has undergone any type of mechanical deformation, the source of these stresses can be attributed to the stress field produced by GNDs present in the material. Traditionally, residual stresses may be divided into three

categories based on the length scale of interest as: type-1 at the component or the sample scale, type-2 at the grain averaged scale and type-3 at the intra-granular scale [65,66]. Based on this classification, another way to look at type-2 residual stresses is by considering them as local deviation in the stress field from the averaged value (individual grain stresses deviating from type-1 residual stresses), similar to the definition of long-range back stresses, which have been defined as the local deviation of stresses from the averaged value by [73]. Since long-range internal stresses have been modeled in CPFE simulations, residual stresses can also be modeled in a similar manner. The relationship between GND densities and long-range backstress is well established as pointed out by [74] who mentions that GNDs contribute to work hardening by creating long-range back stresses. The first step towards incorporating initial GNDs in crystal plasticity simulations has been recently carried out by [75], who initialize the pre-existing residual stress state of the material while simulating the response of a Ti-7Al microstructure subject to tension superposed with bending. The 3D simulation geometry is created based on information about grain positions and orientations, obtained from high energy X-ray experiments. Initial intra-granular residual stresses are calculated based on the difference between the experimentally imposed and the simulated bending stresses which is used to derive an initial GND field in their phenomenological mesoscopic field dislocation mechanics model. The incorporation of residual stresses via the GND field successfully captures the effects of the initial residual stresses present in the material.

For anisotropic plasticity, the GND density needs to be resolved onto individual families of slip systems. Slip systems in HCP materials can be classified into two groups depending on their slip directions: <a> and <c+a>. EBSD-based investigations of <a>-type verse <c+a>-type dislocations in hot rolled Ti-6Al-4V have suggested that <a>-type dislocations are approximately 10 times more common than <c+a>-type dislocations [76]. This is largely due to <a>-type dislocations being more energetically favorable [77]. However, previous studies have observed that <c+a> dislocations can be present in Ti-6Al-4V if various conditions are met, such as low temperature aging [78] and presence of micro-pores [79]. The distribution of <a>-type verse <c+a>-type dislocations in additive manufactured materials is not currently known. In the current work, spatial information in the form of initial GND densities, which is obtained directly from material characterization experiments is initialized in the CPFE model. This initialization of GND densities can be treated as a means to initialize the type-2 level residual stress in the material being simulated.

2.7 Importance of macrozones in failure of Ti alloys

Macrozones have been characterized and studied using a number of experimental techniques, primarily electron backscatter diffraction (EBSD), scanning electron microscopy (SEM), and XRD. Le Biavant et al. [80] studied bimodal Ti-6Al-4V using optical microscopy and SEM imaging to understand the microstructure along with XRD to carry out crystallographic texture analysis. Their analysis reveals that numerous small fatigue cracks form in macrozones which are favorable for prism and basal slip. Humbert et al. [81] analyzed the microstructure of IMI 834, a bimodal Ti alloy and observe macrozones with sharp texture. They studied the possible variant selection during the β to α transformation, which is influenced by the stored elasticity state, and as such, the variant selection follows the minimization of the elastic strain energy. Uta et al. [82] carried out EBSD characterization to understand the orientation distribution and the crystallography of fracture surfaces in IMI 834 subject to dwell fatigue. They observe crack nucleation and propagation in macrozones with mostly primary α grains having their c axes between 10^o and 30^o from the loading axis. Similar to Uta et al. [82], Bridier et al. [83] used EBSD to characterize the microstructure of Ti-6Al-4V, especially the sites for crack initiation during fatigue loading. They observed that fatigue crack formation takes place in macrozones with a [0 0 0 1] texture and suggested that, though crack formation takes place on the basal plane of the α grain, the deformation of macrozones at the mesoscopic scale also plays an important role. Bantounas et al. [84] studied the dependence of c-axis orientation of the macrozone on crack initiation and observed that macrozones with their c-axis close to the loading direction were responsible for faceted fracture and the macrozones with their c-axis being perpendicular to the loading direction act as barriers to faceted crack growth. Echlin et al. [85] carry out high resolution (HR-DIC) on Ti-6Al-4V loaded in-situ and observe strain localization in macrozones well below the macroscopic yield. In cyclic loading they observe early activation of basal slip, which is localized, and further loading leads to prismatic and pyramidal slip across multiple grains within favorably oriented macrozones. Bandyopadhyay et al. [86] carry out HR-DIC experiments on Ti-6Al-4V with MTRs to study the grain level strain localization and accompany it with crystal plasticity simulations to study the effect of high R ratios on MTRs. As with Echlin et al. [85], they also observe activation of multiple families of slip systems, even pyramidal in MTRs with their c-axis nearly parallel to the loading direction leading to the anomalous mean stress behavior on the high cycle fatigue performance experienced by Ti-6Al-4V. In another HR-DIC study, Book et al.

[87] investigated strain localization in additively manufactured Ti-6Al-4V and observe MTR boundaries impede strain transmission, resulting in strain localization. Finally, Britton et al. [76] observe a higher geometrically necessary dislocation (GND) content (approximately twice) in macrozones as compared to the non-macrozone region in Ti-6Al-4V by calculating the intra-granular misorientation using EBSD. The higher GND density indicates that the macrozone may be susceptible to strain localization and hence crack initiation. All of the above reviewed literature suggests that macrozones play a crucial role in strain localization and crack initiation within dual phase Titanium alloys.

2.8 Modeling macrozones

In order to understand the deformation mechanisms in a wide range of Titanium alloys, specifically at the length scale of grains, a number of crystal plasticity models have been developed [4,26,27,45–47,51,57,58,86,88–90] and used to model a number of alloys. Though none of these models have specifically been used to model macrozones, as the authors in these papers limit their simulations to smaller volumes due to the scope of their work, there is nothing inherently missing in these models that prevents their application to model macrozones. Modeling macrozones using continuum level formulations involving grain level deformation is a challenging problem due to the size of the macrozones being orders of magnitude bigger than that of the individual grains. With grains being modeled using hundreds of elements, a single macrozone containing ~1000 grains will contain a minimum of 0.1 million elements within a single macrozone. Though meshing strategies using a coarser mesh may reduce the number of elements, the scale of simulation still remains large. With increasing computing power, it is possible to simulate microstructures with macrozones, albeit such simulations still take enormous computational resources and time to run. This limits the application of crystal plasticity based approaches to model macrozones and paves the way for a reduced order model that does not require such high demands for computational time.

Currently, the means of identifying macrozones within a microstructure is based on the value of the misorientation tolerance used to segment them, which may vary depending on the study in consideration. The process often involves visually identifying macrozones by selecting a region with similar orientations on an EBSD map. Based on literature, the misorientation tolerance used to identify MTRs varies from 15^o [91] to 20^o [92–94]. In this work, a 20° misorientation tolerance is used initially to identify macrozones. Using a 20^o misorientation tolerance, there is

still an outstanding question that needs to be answered: can the deformation within a macrozone be captured by treating the MTR as a single crystal or do the small misorientations within the macrozone play a role in strain localization and hence crack nucleation. In addition, by studying the heterogeneity in the strain accumulation, more insights about deformation within a macrozone can be attained.

Turner et al. [34] emphasize the importance of incorporating initial residual stresses into CPFE simulations. Leveraging their work, the current paper addresses the critical issue of incorporating type-2 residual stresses into crystal plasticity simulations. Further, it also looks at the effect of utilizing physically realistic BCs and grain morphologies. In this study, the results obtained from a simple phenomenological CPFE model are compared with HEDM experiments conducted on Ti-7Al, a single-phase (α-HCP) titanium alloy [95]. The HEDM experiments provide averaged elastic strain (and hence stress) tensors for each grain in the volume being investigated, thereby providing a basis for their comparison with CPFE simulations. The grain by grain comparison ensures that the complete tensorial quantities may be investigated as opposed to a comparison involving only 2D data, like in the case of comparing simulations with DIC. A robust method aimed at initializing type-2 residual stresses in CPFE simulations is proposed and implemented. Its effects along with applying physically realistic BCs, obtained directly from HEDM experiments are evaluated. The implications of this work provide insights into the importance of incorporating initial residual stresses and physically realistic BCs in CPFE simulations. Finally, the effect of using physically realistic grain morphologies obtained from HEDM experiments, as opposed to tessellated grains within the CPFE simulations, on the stress distribution within the simulation volume is investigated.

2.9 Effect of the orientation and morphology of the α and β phases on material properties

Depending on the processing route and the heat treatment used to manufacture them, dual phase titanium alloys can exist in a wide number of microstructural forms. Out of the many possible microstructures, equiaxed and bi-modal microstructures are widely prevalent, due their extensive use in aerospace applications. Owing to the different heat treatment and processing routes used to obtain these two microstructures, the α and β phases of the bi-modal microstructure follow the Burgers orientation relationship (BOR), which aligns the slip systems in the two phases, whereas the α and β phases of the equiaxed microstructure do not follow the BOR. The visual

description of the BOR along with the alignment or misalignment of the α-β slip systems, if the BOR is followed or not is shown in Fig. 2.2. The processing routes used to obtain the two microstructures are similar except for the cooling rates from the recrystallization annealing temperature [1]. A lower rate of cooling results in no lamellas to be formed and the β phase primarily being located at the triple points, resulting in an equiaxed microstructure, whereas a higher cooling rate results in the formation of α lamellae within the β grain, resulting in a bi-modal microstructure.

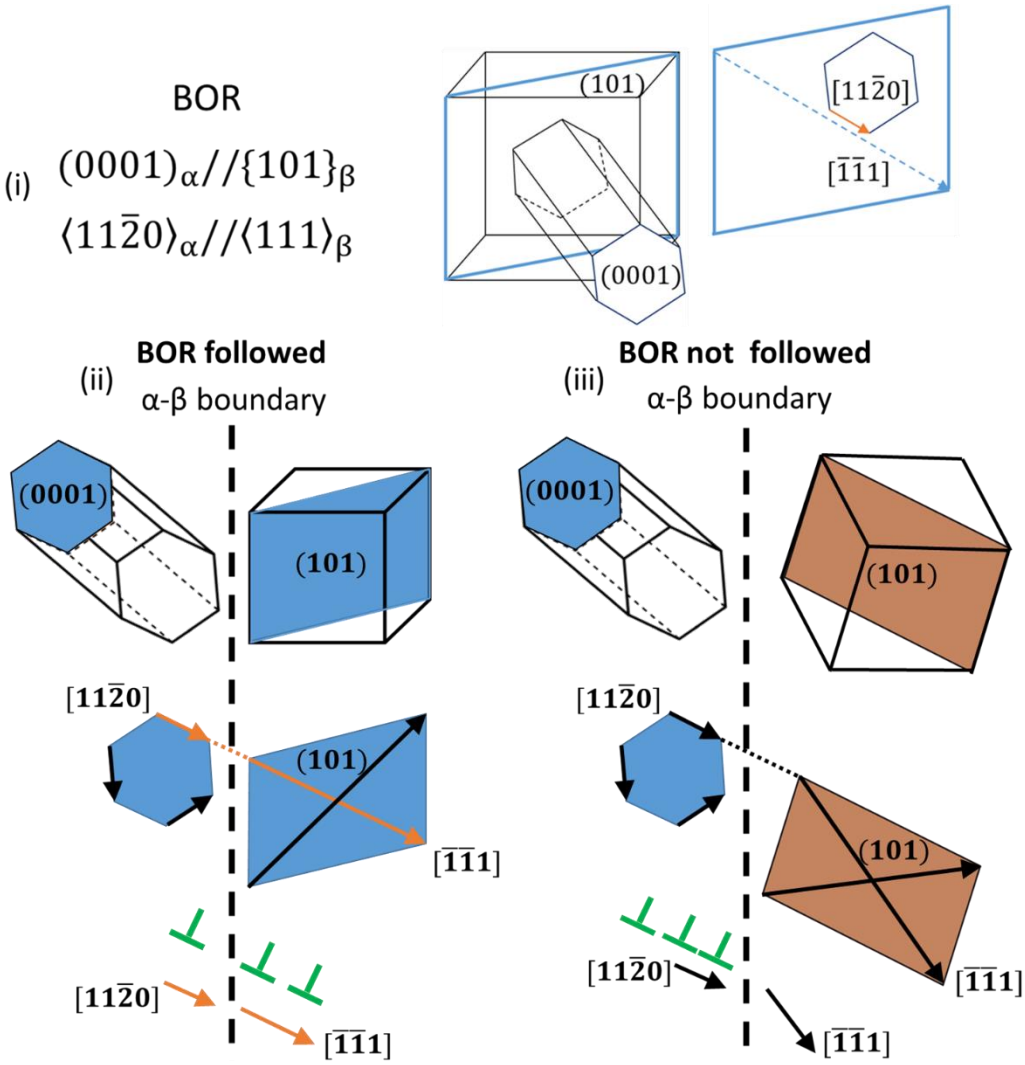

Figure 2.2. Visual representation of the Burgers orientation relationship (Figure recreated from[96]); Detailed look of the α-β interface: (ii) if the BOR is followed, showing aligned slip planes and direction, with easy transmission of dislocations across the interface (iii) if the BOR is not followed, showing non-aligned slip planes and direction, with pileup dislocations at the interface

The primary effect of the existence of the BOR on the deformation in the α-β alloy is the ease of slip transmission across the α-β interface. For the microstructure following the BOR, the slip transmission across the α-β interface is not impeded at the interface due to well-aligned slip systems. Whereas, if the α and the β phases do not follow the BOR, the interface boundary will cause hindrance to slip transfer due to mismatch in their crystallographic orientations. From the point of view of alloy design, formation of the BOR can be controlled by varying the processing route and the heat treatment used to manufacture the alloy [1]. Understanding the effect of the existence of the BOR on specific material properties like time dependent and cyclic loading can provide useful information that can be used to design these α-β alloys for specific applications.

A number of researchers have looked at the effect of orientation, morphology and the volume fraction of the α and β phases in different titanium alloys and its effect on slip transmission and macroscopic properties. Suri et al. [97] compare two colonies of a near-α Ti-5-2.5-0.5 alloy oriented for prismatic slip and observe surprising anisotropy in strength, hardening and creep resistance. Based on detailed TEM characterization, they observe the α/β interface in one colony provides little resistance to transfer of dislocations from the α to the β phase compared to the other colony that shows pile up of edge dislocation at the α/β interface, contrary to the expected behavior (due to the presence of BOR). They then propose a geometric model to explain the observations based on slip transmission across the α/β interface where after sufficient accumulation of dislocations, the dislocations will pass through to the β phase even if the β is not aligned with the α phase. Chan [98] investigated the geometric orientation of the β platelets with respect to the slip system orientation of the α phase by modeling the yielding behavior in α-β colonies of Ti-8Al-1Mo-1V with the β phase modeled with isotropic plasticity. He observed the yield stress of the individual grains increases with the decreasing angle between the slip direction of the α phase and the normal to the β platelets. Further, he conforms the observations of Suri et al. by observing shearing of the β platelets when dislocations impinge on the α-β boundary. Ashton et al. [99] use a strain-gradient based crystal plasticity model for Ti-6242, explicitly modeling the α and β laths, with β phase being modeled with isotropic elasticity, calibrated to micro-pillar compression tests. They analyze the effect of the varying sizes and geometric orientation of the α and β laths on the strength and geometrically necessary dislocations (GND) density and observe higher strength with decreased α ligament size, which is attributed to the increased level of hardening due to GNDs. Further they observe a stronger stress-strain response when the β laths are perpendicular to the

orientation of the α phase slip directions (as opposed to being parallel to it), consistent with Chan [98]. Finally, they comment that modeling the β phase results in lower susceptibility to dwell when compared to modeling only the α phase due to restricted inter-granular load shedding between hard and soft α. Kasamer et al. [59] carry out a detailed parametric study of the geometric features in a β annealed Ti-6Al-4V using a CPFE model with the microstructure being created using Voronoi tessellations. The simulations investigate the dependence of the yield strength on the number of prior β grains in the microstructure, as well as the number of α colonies incorporated within the grain. They observe including remnant β lamellae decreases yield with no effect observed by changing the width of the β lamellae. They also observe low β slip activities in complex morphologies with local micro-texturing (presence of macrozones). Zhang et al. [4,60] also model the the α and β phases explicitly in their physically based CPFE model for Ti-6242, determine the slip properties of the two phases using micro-pillar tests and then study the effect of local variation in microstructural morphology on strain rate sensitivity and load shedding which is critical for dwell fatigue. Looking at a basket weave microstructure, they observe that for a microstructure that follows the BOR, the α phase show considerable effects on structural strain rate sensitivity. They also see reduced strain rate sensitivity with higher number of BOR variants being present in the microstructure. Waheed et al. [100] investigate the load shedding behavior of a specimen containing a rogue grain combination using discrete dislocation plasticity and CPFE modeling and observe that a Widmanstatten microstructure shows less load shedding compared to a colony microstructure. They attribute this to the decrease in dwell sensitivity with the decrease in the mean free path (smaller grain size). Ozturk et al. [61] utilize a fast Fourier transform based elasto-viscoplastic model to analyze the effects of microstructural features on microscopic and macroscopic behavior of additively manufactured Ti-6Al-4V. They observe increasing the α volume fraction enhanced the tensile strength of the material, additionally, increasing the prior β (001) texture decreased the tensile strength. They also observe the α lath thickness as being inversely related to the tensile strength due to decreased slip length. The research works discussed above provide an understanding with respect to the α-β interface and its effect on the macroscopic response of the material. However, these studies do not look at a realistic microstructure at the polycrystalline level. In addition, these studies do not investigate the effect of the difference in the orientation of the α and β phases on time dependent cyclic loading.

CHAPTER 3. INITIALIZING TYPE-2 RESIDUAL STRESSES IN CRYSTAL PLASTICITY FINITE ELEMENT SIMULATIONS UTILIZING HIGH-ENERGY DIFFRACTION MICROSCOPY DATA

In this chapter, a robust method aimed at initializing type-2 residual stresses in CPFE simulations is proposed and implemented. Its effects along with applying physically realistic BCs, obtained directly from HEDM experiments are evaluated. The implications of this work provide insights into the importance of incorporating initial residual stresses and physically realistic BCs in CPFE simulations. Finally, the effect of using physically realistic grain morphologies obtained from HEDM experiments as opposed to tessellated grains in CPFE simulations on the stress distribution within the simulation volume is investigated.

3.1 HEDM experiments

The experimental data used in this study is obtained from the work of Turner et al. [95], which is an open source dataset. In order to get a better understanding of the comparison of simulations with experiments and for the benefit of the readers, the experimental technique is discussed here in brief. For the detailed experimental procedure, the readers are directed to [95]. HEDM is a non-destructive technique utilizing x-rays generated in a synchrotron source to analyze a region of interest within a sample to get grain level continuum data [40–43,101,102] . The technique may be classified as near-field HEDM (nf-HEDM) or far-field HEDM (ff-HEDM) based on the position of the x-ray detector from the sample. Nf-HEDM offers detailed information about grain morphology and intra-granular misorientation with the x-ray detector being placed close to the specimen as opposed to ff-HEDM, which provides the complete strain tensor (and hence the stress tensor) for an individual grain, grain averaged crystallographic orientation and grain centroids, with the detector being placed farther away from the sample, which is evident in the nomenclature of the two techniques.

The diffraction data was collected in-situ at four load steps including the residual state during the tensile loading of the specimen with ff-data being collected for all four load steps and nf-data being collected only at load step 3, with the load steps corresponding to specific points on the stress-strain curve, shown in Fig. 3.3. This is done due to the large amount of time taken to perform nf-scans coupled with the fact that the sample is loaded to a value just before its yield

point, as shown by the experimental stress-strain curve in Fig. 3.3, and there would not be significant changes in grain morphology from load step 0 to 3. Even though the specimen is loaded marginally below its yield point, a number of grains will plasticize due to varying grain orientations that exist within the sample. The volume interrogated by the ff-HEDM technique consists of a rectangular box with dimensions of 1 mm x 0.6 mm x 1 mm, composed of 605 grains. The nf-data originally consisted of 240 grains but after data reduction, which involved setting a threshold on the confidence index and ensuring the nf-grains are contained within the ff-volume, the nf-grains are reduced to 39 in number. This combined nf and ff data is utilized to create the FE mesh and get information about the evolution of strain in each grain with the nf-data being utilized only for obtaining the grain morphology of the nf-grains and the strain and grain centroids being determined from the ff-data.

3.2 FE mesh generation

The first step towards carrying out a CPFE simulation involves generating a physically realistic microstructural mesh that will be used to run the simulations. Since both nf and ff-HEDM data is available, in order to fully exploit the available information, both these data sets are utilized to generate the FE mesh. The procedure to create the microstructural mesh is similar to the one utilized by [34] with a few variations, which are introduced to improve the computational efficiency of the simulations. Firstly, the total volume of interest (1 mm x 0.6 mm x 1 mm) is partitioned into three zones and each zone is meshed using hexahedron elements as shown in Fig. 3.1. The center region with a fine mesh of element size 5 μm x 4 μm x 5 μm corresponds to the region of the nf-data and the top and bottom regions with a coarser mesh of element size 10 μm x 10 μm x 10 μm corresponds to the region of the ff-data. Hexahedron elements are used to ensure that element distortion and volumetric locking does not take place during loading as may be the case if tetrahedral elements are utilized [103]. However, the main motivation to use hexahedron elements is the following: since the nf-data is in the form of voxels, creating microstructural grains can be easily achieved by a one to one assignment of the nf-voxels to the nearest hexahedron FE element, as discussed in the next paragraph. Further, due to the higher accuracy of the hexahedron elements, they are suitable for comparing meshes with different sizes, as will be discussed in Section 3.7. Since two sizes of finite elements are used, there will be mismatch in the number of nodes across the ff to nf region, which will result in the simulation not being feasible to run. To

resolve this issue, *tie* constraints, available within Abaqus are utilized to ensure displacements of the nodes at the transition region are consistent.

Since the nf-data is collected in the form of voxels, a microstructural mesh corresponding to the nf-region is created by assigning each nf-voxel to the closest finite element in the nf-zone. This one to one assignment results in the creation of a microstructural mesh for the nf-grains. Since only 39 nf-grains are available, there will be a number of finely meshed elements (in the nf-zone) along with all the coarse meshed elements (in the ff-zone) that will not have any nf-data point corresponding to them. These remaining elements are utilized to create the ff-microstructure by assigning them to the nearest ff-grain centroid, based on the distance between the element and the ff-grain centroid. The elements belonging to the same grain are grouped together to form a microstructure with tessellated grains. The final microstructural mesh with the ff and nf grains consists of 2,400,000 elements and is shown in Fig. 3.2. It may be argued that the procedure of tessellating the ff-grains inside a fixed volume does not result in the recreation of the exact microstructure of the material, however the grain neighbors and relative grain sizes would be similar to the actual microstructure and hence the comparison between simulations and experiments would be feasible. Further, the dependence of accurate grain morphologies on simulation results are discussed in Section 3.7.

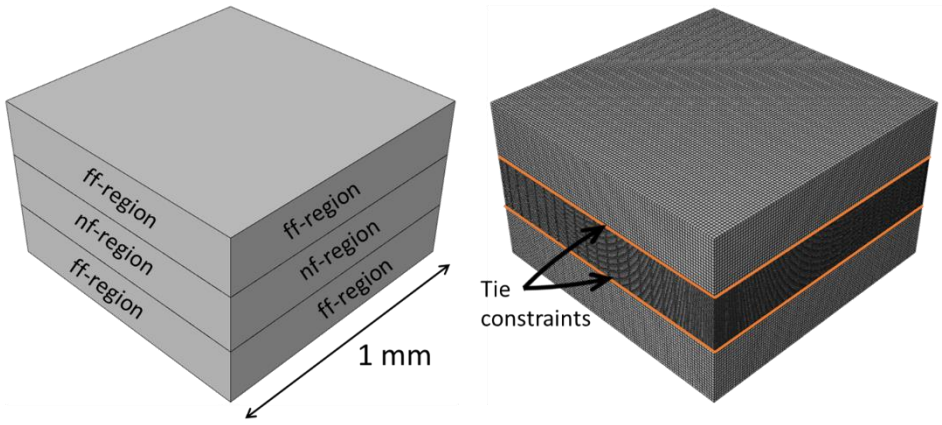

Figure 3.1. Volume of interest divided into 3 zones with a fine mesh for the nf-grains and a coarse mesh for the ff-grains

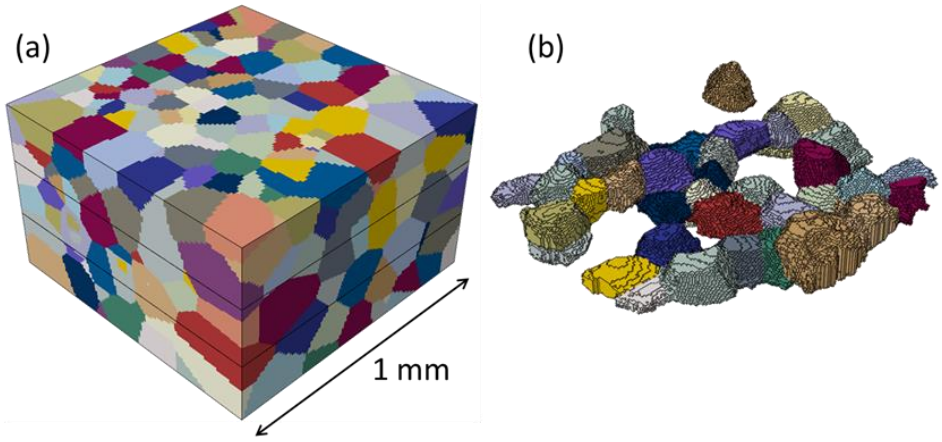

Figure 3.2. FE microstructural mesh showing grains colored according to grain IDs: (a) Entire simulation volume containing ff and nf grains; (b) nf-grains separated from the simulation volume

3.3 Crystal plasticity model

The CPFE model used in this work is a simple rate-dependent phenomenological model based on [6,27,104,105] and is discussed here in brief. The kinematics of the deformation are captured by the standard multiplicative decomposition of the deformation gradient as follows.

$$\mathbf{F} = \mathbf{F^E}.\mathbf{F^P} \tag{3.1}$$

Where $\mathbf{F}$ is the total deformation gradient. The decomposed part $\mathbf{F^E}$ corresponds to the elastic part of the deformation gradient, capturing the rigid body motion and stretch of the lattice and $\mathbf{F^P}$ corresponds to the plastic part, which captures the dislocation motion or glide in the crystal lattice. The plastic velocity gradient in the intermediate configuration is evaluated by the following equation.

$$\mathbf{L^P} = \dot{\mathbf{F}}^{\mathbf{P}}.(\mathbf{F^P})^{-1} = \sum_{\alpha=1}^{N_{sys}} \dot{\gamma}^{\alpha}(\mathbf{s_0^{\alpha}} \otimes \mathbf{n_0^{\alpha}}) \tag{3.2}$$

With s_0^{α} and n_0^{α} being the slip plane normal and direction for the α^{th} slip system respectively and $\dot{\gamma}^{\alpha}$ being the shearing rate for the α^{th} slip system. The flow rule, relating the shearing rate on a slip system to the resolved shear stress is represented using a power law represented by Eqn. 3.

$$\dot{\boldsymbol{\gamma}}^{\boldsymbol{\alpha}} = \dot{\boldsymbol{\gamma}}_{\mathbf{0}} \left|\frac{\boldsymbol{\tau}^{\boldsymbol{\alpha}}}{\mathbf{g}^{\boldsymbol{\alpha}}}\right|^{\mathbf{m}} \mathbf{sgn}(\boldsymbol{\tau}^{\boldsymbol{\alpha}}) \tag{3.3}$$

Where τ^{α} and $g^{\alpha}$are the resolved shear stress and slip system resistance for the α^{th} slip system, respectively. And m is the inverse rate sensitivity exponent. The slip-system resistance is made to evolve according to an Armstrong-Frederick hardening model as follows [106].

$$\dot{\mathbf{g}}^{\boldsymbol{\alpha}} = \mathbf{H}\sum_{\boldsymbol{\beta}=\mathbf{1}}^{\mathbf{N}} \mathbf{q}^{\boldsymbol{\alpha\beta}} \left|\dot{\boldsymbol{\gamma}}^{\boldsymbol{\beta}}\right| - \mathbf{H_D}\mathbf{g}^{\boldsymbol{\alpha}} \sum_{\boldsymbol{\beta}=\mathbf{1}}^{\mathbf{N}} \left|\dot{\boldsymbol{\gamma}}^{\boldsymbol{\beta}}\right| \tag{3.4}$$

In the above equation, H and H_D are the direct and dynamic recovery coefficients associated with isotropic hardening. $q^{\alpha\beta}$ may be referred to as the hardening coefficient responsible for interaction between different slip systems. It is kept at 1 for self-hardening and 0 for latent hardening due to the planar nature of slip observed in these titanium alloys [107]. N is the number of slip systems incorporated in the model, corresponding to the basal and prismatic slip systems which are primarily active in these materials, thus N=6. To keep the CPFE model simple, the pyramidal slip systems (both 1^{st} and 2^{nd} order) are neglected as they have a very high critical resolved shear stress value, often 1.1 to as high as 15 times that of prismatic and basal slip systems [45]. In addition, since the sample is loaded only until marginally below its yield point, the activation of the pyramidal slip systems is highly unlikely. The simulations carried out in this work do not involve cyclic loading or even large amounts of plasticity, hence the choice of the constitutive model will not play a big role in the results and this modeling framework can be modified at any stage to incorporate different constitutive relations.

This CPFE model is incorporated in a commercially available FE software, Abaqus via a user material subroutine (UMAT). Most of the CPFE parameters are estimated from literature. The critical resolved shear stress values are taken from [108] and the elastic constants from [109]. Recent studies in titanium alloys have shown that the strain rate sensitivities of the basal and prismatic slip systems are not the same [60], [2]. For the current work, the inverse rate sensitivity exponent for the basal slip system is taken to be double that of the prismatic slip system value based on [2]. These constants along with the hardening constants are further optimized using a Genetic algorithm based optimization routine to ensure that the simulated stress-strain curve matches the one obtained from experiments [50]. The values of all the parameters after fitting along with the elastic constants used in the simulations are given in Table 3.1.

Table 3.1. Optimized crystal plasticity parameters used for simulations

Parameter	Value	
	Basal	Prism
$\dot{\gamma}_0$ (1/s)	0.001	
m	50	25
H (MPa)	6100	6100
H_D	10	10
$g^{\alpha}(0)$ (MPa)	200	180
C_{11} (MPa)	162400	
C_{12} (MPa)	92000	
C_{44} (MPa)	46700	
C_{13} (MPa)	69000	
C_{33} (MPa)	180700	

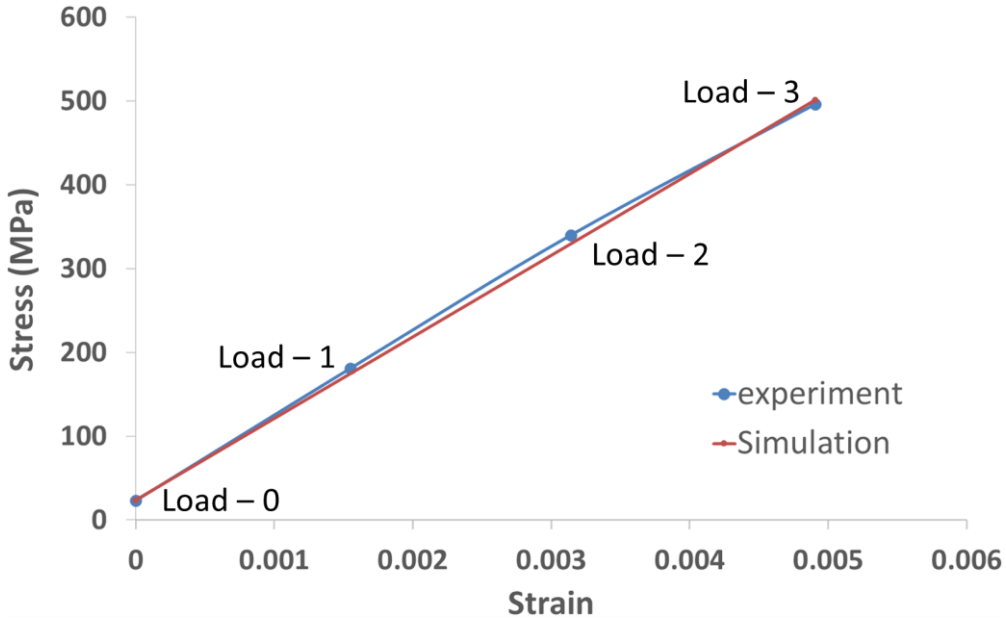

Figure 3.3. Experimental and simulated stress-strain curves, with the simulation corresponding to a simple uniaxial CPFE simulation with constants from Table-3.1

3.4 Initializing residual stresses

We propose a universal and detailed mathematical treatment for initializing residual stresses in CPFE simulations which is discussed as follows. The presence of initial residual stresses does not cause any deformation in the material, hence the initial total deformation gradient at the start of the simulation is set to be the identity tensor.

$$\mathbf{F} = \mathbf{I} \tag{3.5}$$

As discussed in Section 3.3, conventionally, the total deformation gradient is multiplicatively decomposed into its elastic and plastic parts. However, if residual stresses exist, the elastic part of the deformation gradient cannot equal the identity tensor as the stresses in the simulation are calculated from strains, which are in turn evaluated from $\mathbf{F^E}$.

$$\mathbf{F^E} \neq \mathbf{I} \tag{3.6}$$

Using the initial grain averaged strain tensors from HEDM and a small strain assumption, the initial elastic part of the deformation gradient ($\mathbf{F^E}$) is evaluated by solving the equation below, where $\boldsymbol{\varepsilon}$ is the elastic strain tensor obtained from HEDM.

$$\boldsymbol{\varepsilon} = \frac{\mathbf{1}}{\mathbf{2}}\left(\mathbf{F^{E^T}} + \mathbf{F^E}\right) - \mathbf{I} \tag{3.7}$$

The strain tensor measured at Load 0 is the sum of residual strains and the strains caused as a consequence of the initial loading of the specimen. To determine the exact residual strain tensor ($\boldsymbol{\varepsilon_{res}}$), the strain caused due to loading is subtracted from the experimentally measured strain tensor. Where the strain caused due to tensile loading, $\boldsymbol{\varepsilon_{applied}}$ is evaluated by calculating an elastic solution corresponding to loading the specimen to 23 MPa (which corresponds to the tensile load applied at Load 0)

$$\boldsymbol{\varepsilon_{res}} = \boldsymbol{\varepsilon} - \boldsymbol{\varepsilon_{applied}} \tag{3.8}$$

Based on the elastic-plastic decomposition of $\mathbf{F}$, when an initial $\mathbf{F^E}$ is prescribed, in order to maintain $\mathbf{F}$ as the identity tensor, a counter deformation needs to be accounted for by $\mathbf{F^P}$ (thus $\mathbf{F^P}$ not being equal to the identity tensor). However, if we investigate closely, $\mathbf{F^P}$ not being equal to the identity tensor would result in plastic deformation at the beginning of the simulation, which does not necessarily correspond to the residual stress, as residual stress is caused due to previous irreversible deformation. This leads to setting the value of $\mathbf{F^P}$ at the start of the simulation to be the identity tensor. To ensure $\mathbf{F^P}$ equals the identity tensor while $\mathbf{F^E}$ does not, an alternative methodology is proposed. The total deformation gradient is multiplicatively decomposed into three components as follows.

$$\mathbf{F} = \mathbf{F^E F^R F^P} \tag{3.9}$$

This decomposition is very similar to the elastic-plastic decomposition described in Section 3.3, with an additional deformation gradient, $\mathbf{F^R}$, introduced to maintain $\mathbf{F}$ as well as $\mathbf{F^P}$ equal to the identity tensor. It is very important to note that in this approach, the initial residual stress is caused only as a consequence of $\mathbf{F^E}$ ($\mathbf{F^E}$ being calculated from the HEDM data using the elastic

strain tensor, $\boldsymbol{\varepsilon}$). $\mathbf{F^R}$ does not produce a stress field and is only introduced as a sort of *Eigen deformation gradient* (Similar to Eigen strains introduced by Eshelby [65]) to ensure both $\mathbf{F}$ and $\mathbf{F^P}$ equal the identity tensor at the initial time step.

Since only grain averaged elastic strain (and hence the associated stress) values are extracted from the HEDM data, the value of the initial $\mathbf{F^E}$ prescribed to each element is constant for an entire grain. This distribution of stress (single value for an entire grain) will result in equilibrium not being satisfied within the volume in consideration. To investigate the stress distribution in the simulation volume that would exist if equilibrium is enforced, a simple CPFE simulation is set up by supplying an initial grain averaged $\mathbf{F^E}$ to elements of individual grains along with zero displacement imposed at the top surface. The other BCs include fixing the bottom surface and 2 side surfaces as shown in Fig. 3.6. This BC is chosen as it best represents the BC that the volume in consideration experiences at the initial load state (Load 0). The results for this equilibration simulation are presented in Fig. 3.4 and Fig. 3.5, with Fig. 3.4 being a plot of the equilibrated grain averaged residual stresses in the loading direction plotted against grain identification numbers, IDs, and Fig. 3.5 provides a visual representation of this stress in the nf-grains. For the results, we focus only on the 39 nf-grains and not on all the 605 grains, as plotting all 605 grains would make interpreting the graphical results difficult. The deviation bars in Fig. 3.4 indicate the maximum and minimum element values of stresses that exist within a grain, which suggests that in order to satisfy equilibrium, the stress in a grain is redistributed and deviates from the averaged value. Looking at the stress distribution in individual grains in Fig. 3.5, it is observed that the maximum stress values occur at the grain boundaries, which is not surprising, as we would expect higher incompatibility between neighboring grains due to the difference in their crystallographic orientations and associated anisotropy of their elastic and plastic response.

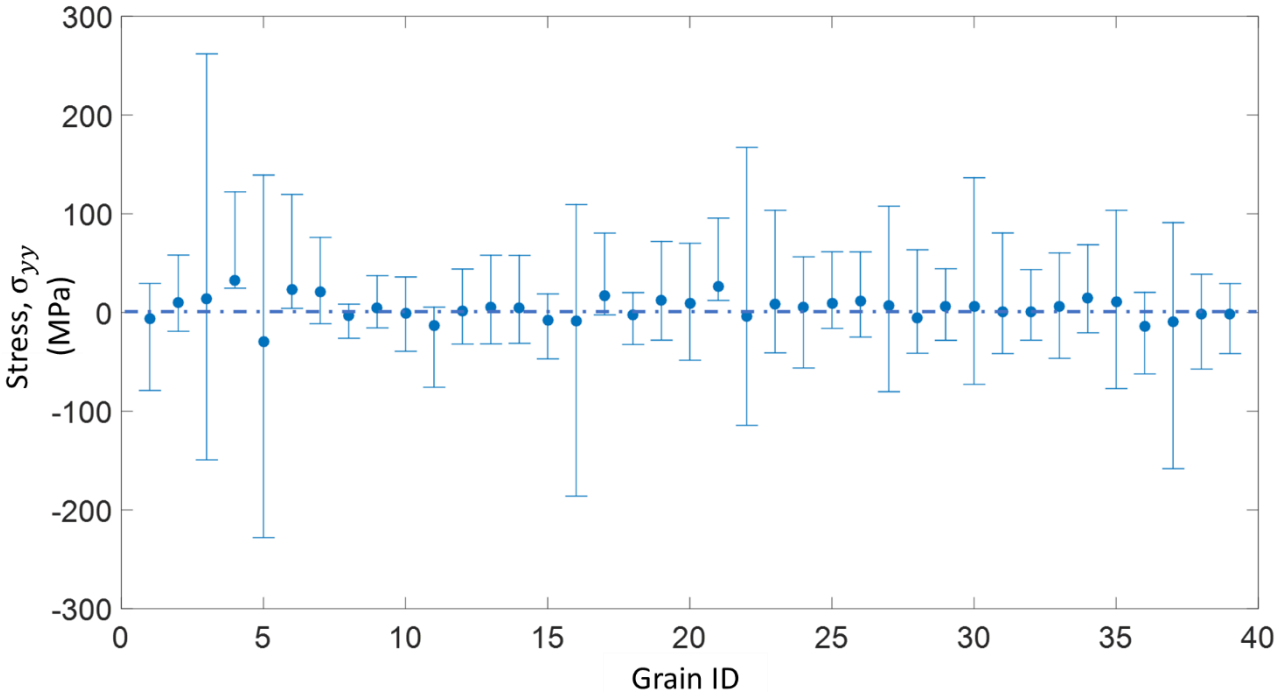

Figure 3.4. FE equilibrated grain averaged initial residual stress values plotted against grain-ID, with deviation bars indicating the maximum and minimum values within a grain. The dashed line corresponds to zero stress.

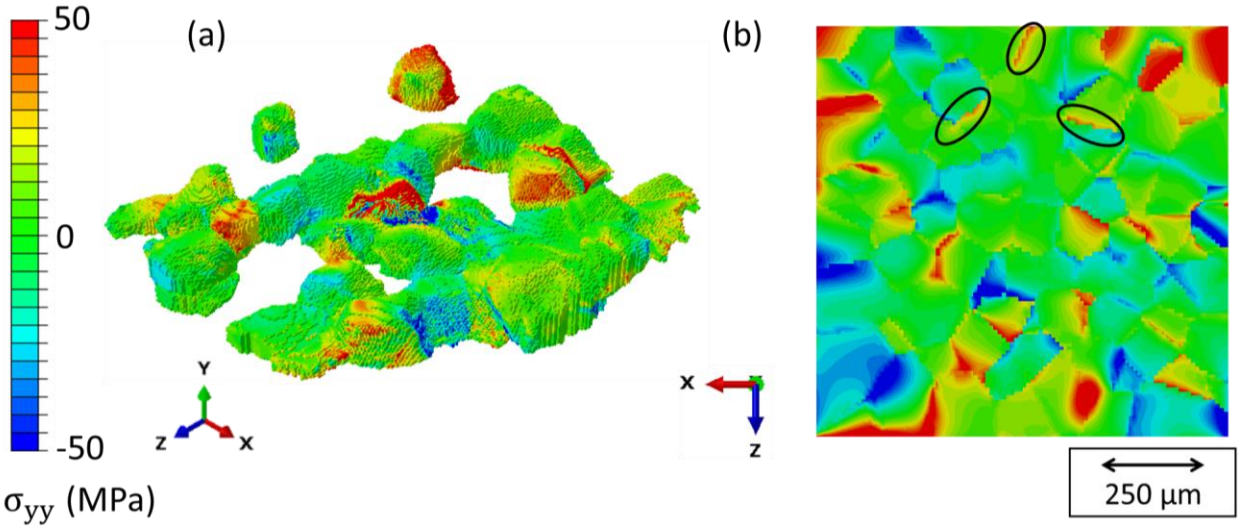

Figure 3.5. Stress in loading direction after FE equilibration: (a) nf-grains; (b) Bottom surface of the simulation volume showing high stress concentration at the grain boundaries. Note: Legend max and min values do not correspond to the actual max and min values of the stresses. Stresses higher/lower than the max/min are represented in the same color as the legend max-min (i.e. saturated values)

These simulation results correspond to the redistributed $\mathbf{F^E}$ that has satisfied equilibrium and hence is the distribution of residual stresses that exists within the grains. Since the FE solver ensures that equilibrium is satisfied, this is the distribution of $\mathbf{F^E}$ (and hence the residual stress) that is utilized to run the CPFE simulations. After the redistribution of stresses in order to satisfy equilibrium, elements within a grain show deviation from the grain averaged value highlighted by the bars in Fig. 3.4. Though this is expected, grains 3, 5, 16 and 22 show considerably large spread in intra-granular stress values compared to other grains. The location of these grains with large error bars in the simulation volume is shown in Fig. 3.6a and it is observed that they are located together and can be considered as a cluster (Fig. 3.6b) for further analysis.

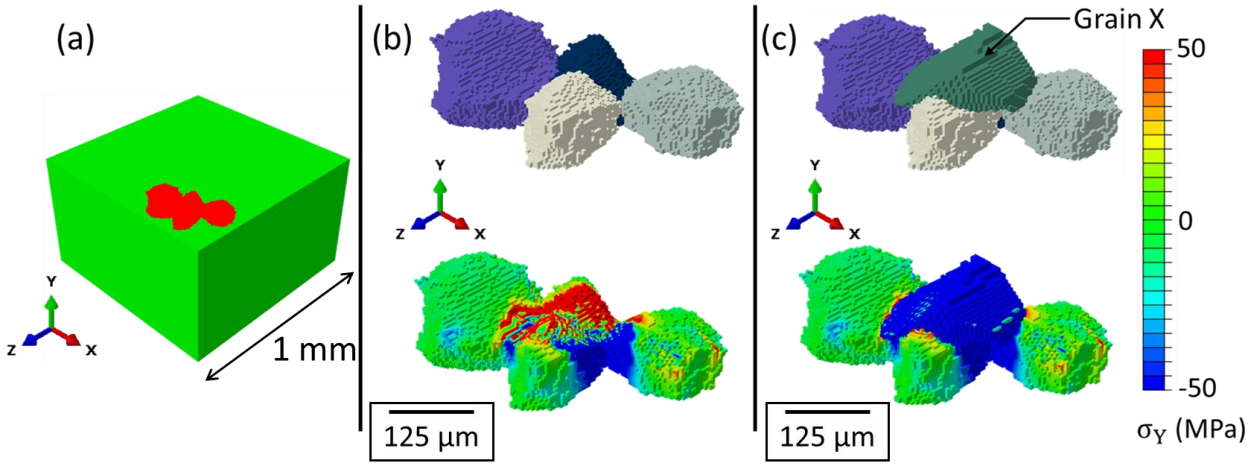

Figure 3.6. (a) Location of the grains with large deviation bars within the simulation volume; (b) grain cluster separated from the simulation volume along with its simulated stress (at Load 0, after equilibration) distribution in the loading direction; (c) Grain neighboring the cluster along with its stress distribution in the loading direction (at Load 0, after equilibration)

To examine the reason for the large deviation bars, the neighboring grains of this grain cluster are investigated. It is observed that this grain cluster has a relatively large grain as its neighbor, shown in Fig. 3.6c, referred to as grain X. The residual stress state of this neighboring grain (Grain X), obtained from HEDM experiments is as follows:

$$\sigma = \begin{bmatrix} -109.4 & 110.2 & 40.8 \\ & -249.7 & -3.0 \\ symm & & 102.1 \end{bmatrix} \text{MPa}$$

The high amount of residual stresses in Grain X causes the grain cluster neighboring it to have extreme values of stresses close to its grain boundaries in order to satisfy equilibrium. The

method to initialize residual stresses presented here focuses on incorporating type-2 residual stresses into CPFE simulations. However, this method can be extended to include type-3 residual stresses without requiring any changes to the methodology, provided type-3 residual stress data is available in some form.

3.5 Physically realistic boundary conditions

As discussed in Chapter 2, in most cases, if the actual BCs are not available for modeling the mesoscopic response, the ones prescribed to run the CPFE simulations need to be based on some assumptions. Since the sample in discussion was subjected to uniaxial tension during the HEDM experiment, if physically realistic BCs were not available (as is the case with a number of CPFE simulations that are not coupled with HEDM or other experiments), the BCs imposed on the volume in consideration would correspond to the case of tensile loading, as motivated by [64]. Although the sample considered in this study is constraint free on all the four sides (X and Z faces of the specimen), corresponding to the experimental conditions. Hence the BCs shown in Fig. 3.7 would be more relevant, as fixing the displacement BCs on any of the sides would introduce artificial constraints.

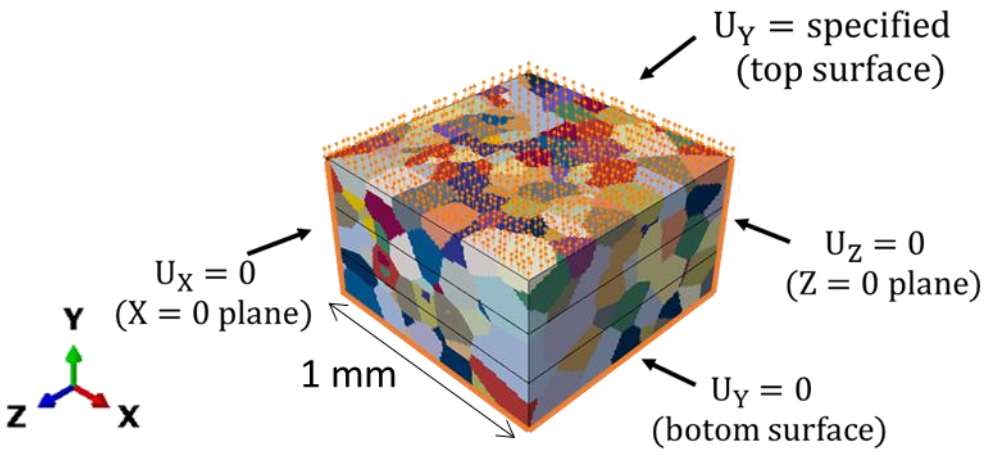

Figure 3.7. Simple BCs applied to simulation volume for tensile loading

Since the current study focuses on a set of 605 grains within a larger sample with grains having varying orientations, due to the neighbor constraint effects of the grains surrounding the volume in consideration, it is highly unlikely that the simulation volume is under a perfect tensile

load. To obtain physically realistic BCs, the simulation volume is loaded in stress-control (instead of displacement control) with a unique stress value, based on a fitting routine, being applied to each of the 107 grains that touch the top surface. The fitting routine is used to specify stress values for each of the top 107 grains such that their final stress state is similar to the one observed experimentally. It may be argued that imposing experimentally observed stress would bias the correlation between simulations and experiments. However, to study this correlation, the results of only the 39 nf-grains, which are significantly away from the top or bottom surface are utilized. Thus, imposing experimental stresses on the top surface will in no way bias the correlation between experiments and simulations.

3.6 Results

A simple and reliable way to visualize the correlation between experiments and simulations is to plot grain averaged quantities (like stresses) obtained from simulations against experiments. An exact correlation between the two would result in the data points corresponding to all the grains lying on a 45˚ line. To quantify the improvements due to the incorporation of new BCs and initializing residual stresses, a measure of error is introduced: the deviation (distance) of a given point from the 45˚ line, which can be computed using the metric for distance of a point from a 45˚ line passing through the center of the coordinate axis. The total deviation for the quantity being plot is then evaluated by summing up this calculated value for all the grains being plot, as described in Eqn. 10.

$$\text{Deviation} = \frac{1}{\text{no. of grains}} \sum_{n=1}^{\text{no.of grains}} \left| \frac{x_n - y_n}{\sqrt{2}} \right| \tag{3.10}$$

Where x_n and y_n are the values of the grain being plot, with x_n corresponding to the experimental value and y_n being the simulation value. To understand how well the simulated data compares with experiments, three quantities are chosen for comparison: stress in the loading direction (σ_{yy}), hydrostatic stress (σ_{Hyd}) and coaxiality (Φ), which are defined as follows.

$$\sigma_{Hyd} = \frac{(\sigma_{xx} + \sigma_{yy} + \sigma_{zz})}{3} \tag{3.11}$$

$$\Phi = \text{acos}\left(\frac{\bar{\sigma}_{\text{sample}} \cdot \bar{\sigma}_{\text{grain}}}{\left|\bar{\sigma}_{\text{sample}}\right| \left|\bar{\sigma}_{\text{grain}}\right|} \right) \tag{3.12}$$

Where $\overline{\sigma}$ refers to as the stress vector defines as:

$$\overline{\sigma} = [\sigma_{xx}, \sigma_{yy}, \sigma_{zz}, \sigma_{xy}, \sigma_{xz}, \sigma_{yz}] \tag{3.13}$$

Since the experimental sample is subject to pure tensile loading in the y-direction, its macroscopic stress vector would be: $\overline{\sigma}_{\text{sample}} = [0, 1, 0, 0, 0, 0]$. The value of $\overline{\sigma}_{\text{grain}}$ is obtained either from the HEDM experimental data or CPFE simulations.

Two simulations are carried out: a simple CPFE simulation with no initializations (Case 1) and another CPFE simulation with initialized residual stresses and physically realistic BCs (Case 2). Fig. 3.8 shows the grain averaged stress in the loading direction (σ_{yy}) for the experiment and the simulation with initialized residual stresses and physically realistic BCs. The plot corresponding to the stress values in loading direction is shown in Fig. 3.9. The values of the summed error for the stress in loading direction along with hydrostatic stress and coaxiality are given in Table 3.2.

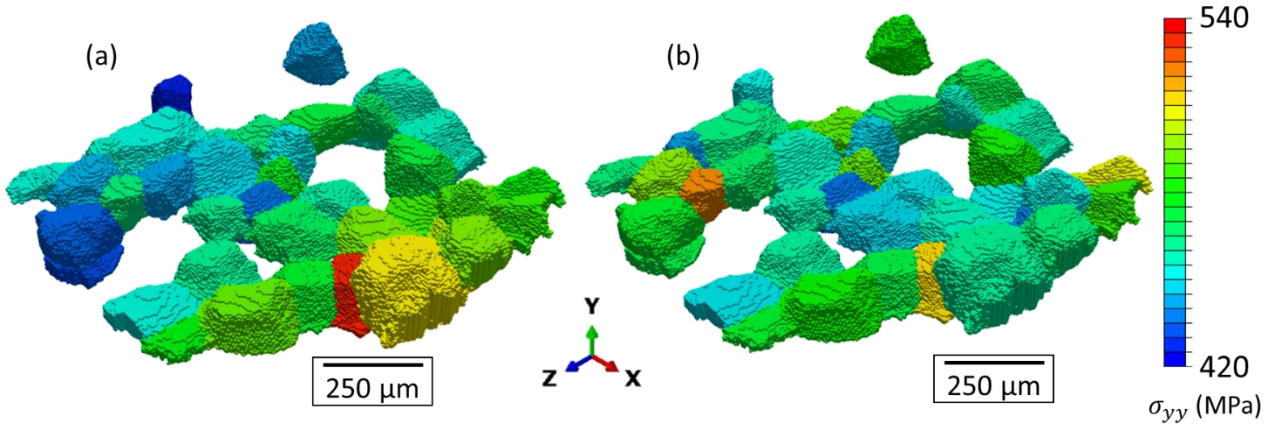

Figure 3.8. Grain averaged stress, σ_{yy} in loading direction: (a) Simulation (b) Experiments for CPFE simulation with initialized residual stresses and correct BCs

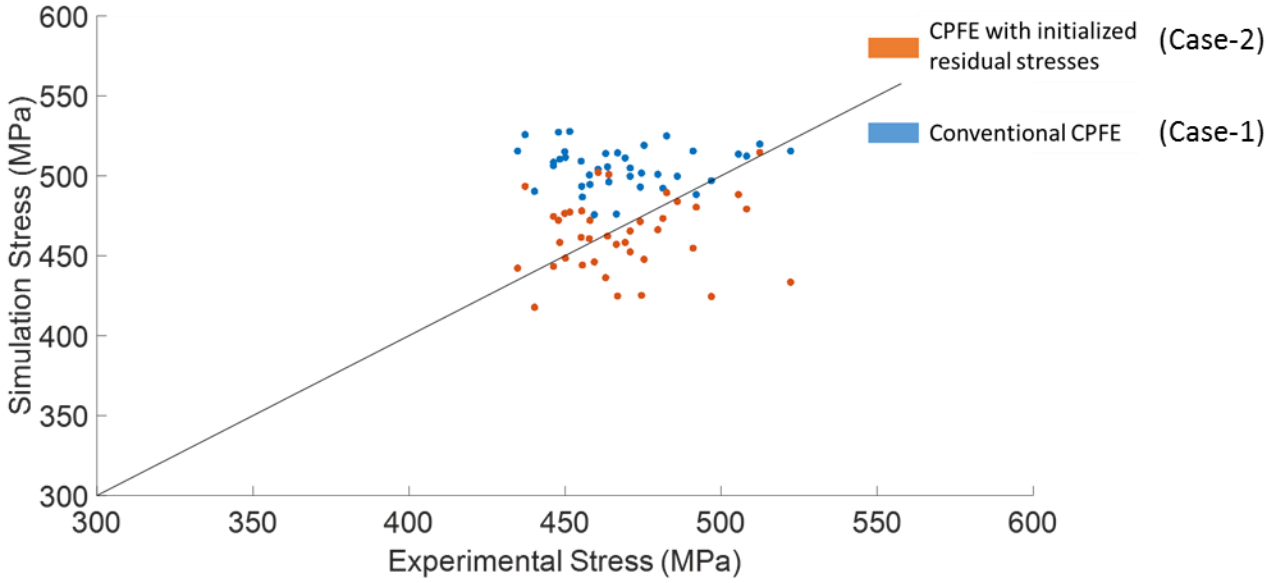

Figure 3.9. Simulation vs. experiment plot for stress in loading direction, σ_{yy}

Table 3.2 Values of the summed error for the grains in consideration

Summed error	**Case 1**	**Case 2**
Stress in loading direction (σ_{yy})	46.4 MPa	14.9 MPa
Hydrostatic stress (σ_{Hyd})	121.2 MPa	77.1 MPa
Coaxiality (Φ)	1.9°	1.8°

3.7 Discussion

Based on the values of the summed error for the quantities being analyzed, it is evident that by utilizing a simple CPFE model without any initialization and with simple BCs (Case 1); the quantities obtained from the simulations provide a poorer match with experiments. Initializing residual stresses and adding physically realistic BCs (Case 2) improves the correlation between experiments and simulations, which is evident by the fact that the points corresponding to the grains line up with the 45˚ line (Fig. 3.8) and is quantitatively represented by the decrease in the value of the summed error in Table 3.2.

Though incorporating residual stresses along with addition of physically realistic BCs results in improvement in correlation with experiments, there is still some error that exists between the two. One possible reason for the deviation may be attributed to the HEDM strain data itself. In

general, the HEDM strain measurement is limited by the resolution of the x-ray detector. For the current experiment, this resolution was in the order of $5e-4$ (in terms of lattice strain). The residual strains, which correspond to the zero load state are inherently small as the sample is not loaded at this state. The resolution of the detector coupled with low strains in the residual state results in a higher noise to signal ratio which may induce some errors in measurements.

In the current study, only the stress state of the nf-grains is chosen for comparison with that of the experiments. One of the main reasons for comparing only the nf-grains for the analysis was that the nf-grains provide exact grain morphologies. The morphological detail, though beneficial, has a downside that the process of carrying out nf-scans is time consuming (24 hours for the current dataset) as opposed to ff-scans which can be completed in minutes (12 minutes for the current dataset). In studies where grain morphology is of prime importance, carrying out nf-scans is inevitable. However the main application of the experimental dataset utilized in this work was to compare it with results obtained from simulations. The comparison between experiments and simulations in the current study only involves grain averaged quantities, hence it is possible that the entire grain morphology may not be beneficial considering the amount of time it takes to obtain this information, resulting in the following question: Does having a physical grain morphology as opposed to tessellations created from centroidal data offer any additional useful information about the stress distribution within the simulation volume? To answer this question, results utilizing two FE meshes, one with all the grains created using centroidal tessellations and the other with the 39 nf-grains created using the experimental data with physical grain morphology (as described in Section 3.2) are compared with each other. Figure 3.10 shows the comparison between the two FE meshes for the 39 grains considered for the results, one with the exact grain morphology obtained from the nf-data and the other with the tessellated grains created from the ff-centroid data. It is observed that the location of the grains is captured well by the tessellations but the grain sizes are not correctly represented. Since the tessellated grains do not provide exact grain morphology, using an extremely fine mesh does not serve any purpose and hence a coarser mesh, with an element size of 10 μm x 10 μm x 10 μm (as opposed to 5 μm x 4 μm x 5 μm for the mesh of the nf grain microstructure) is utilized for the same, as would be the case if only ff-data was available. In general, the difference in the mesh size may introduce differences in stress distributions, however the new tessellated mesh still contains 600,000 elements and is considered to be fine enough not to induce errors, especially since hexahedron elements are used to create the mesh.

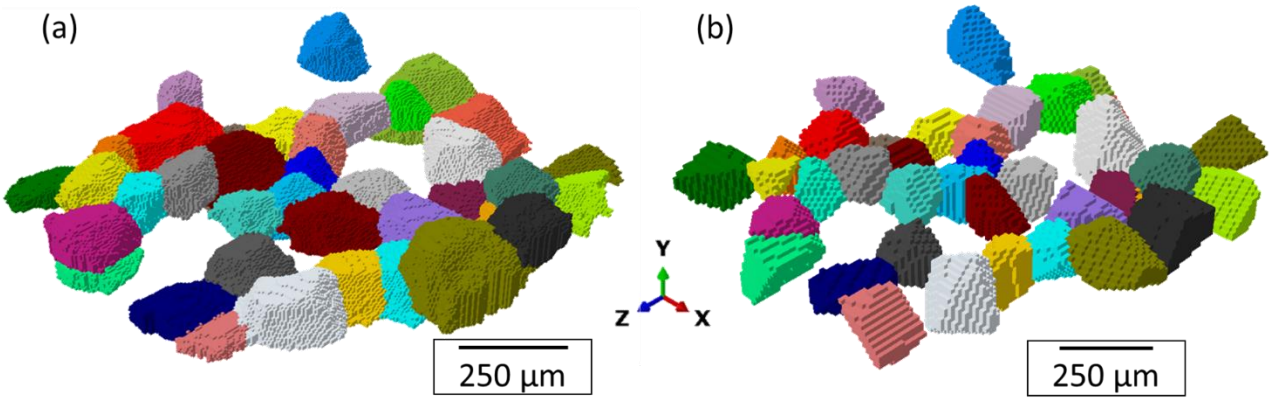

Figure 3.10. Comparison of grain morphologies: (a) FE mesh with exact grain morphology obtained from nf-data; (b) FE mesh with voronoi tessellated grains using ff-centroid data. Colors indicate grain IDs

To understand the effect of this difference in grain morphology on the final results relating to this study, the distribution of stresses in the two FE meshes is evaluated. Fig. 3.11 shows the grain averaged stresses in the loading direction for the two cases, which match well as the relative inter-granular stress distribution is similar in both the meshes, barring minor variations. The difference in the grain averaged stress in loading direction as well as hydrostatic stress for the two cases is quantitatively shown in Table 3.3, which confirms the visual observation that there is negligible difference in the grain averaged quantities between the two meshes. However, the main advantage of utilizing the exact physical grain morphology in this study is to have a better understanding of the distribution of the stresses. The grain morphology may play a role in localization of stresses, which might not be captured by the tessellated grains. Fig. 3.12 shows the stress in the loading direction, which has not been grain averaged. Though the mesh with the tessellated grains shows relatively higher stresses at the grain boundaries than the mesh with the exact grain morphology, the regions of stress localization is identical in both the cases.

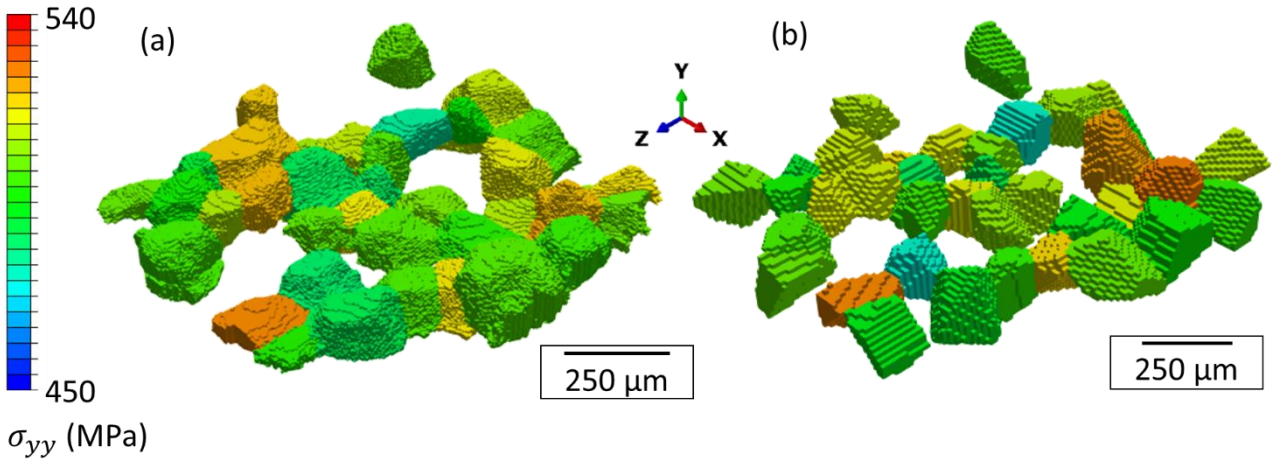

Figure 3.11. : Grain averaged stress, σ_{yy} in loading direction (at Load 3): (a) FE mesh with exact grain morphology obtained from nf-data; (b) FE mesh with voronoi tessellated grains using ff-centroid data

Table 3.3. Values of the summed difference between the nf+ff grain mesh and ff grain mesh, scaled to the number of grains

Summed difference	
Stress in loading direction (σ_{yy})	28.2 MPa
Hydrostatic stress (σ_{Hyd})	40.0 MPa

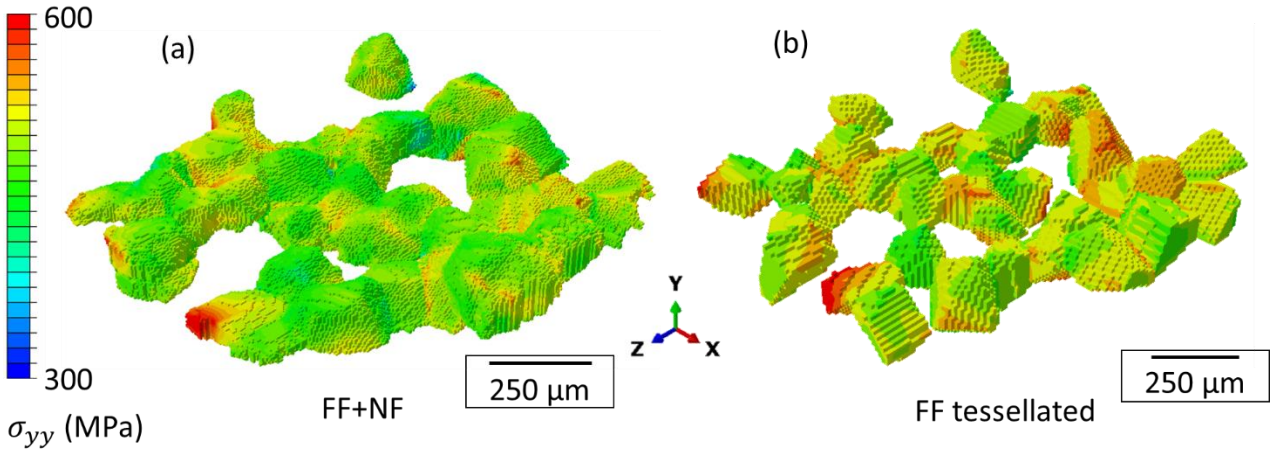

Figure 3.12. Stress in loading direction (at Load 3): (a) FE mesh with exact grain morphology obtained from nf-data; (b) FE mesh with voronoi tessellated grains using ff-centroid data

From these FE simulation results, it is observed that having exact grain morphologies does not substantially change the grain averaged stress states during simulation when compared to

tessellated grains. Moreover, the regions of stress localization are also captured reasonably well by the mesh with the tessellated grains when compared with the physically realistic grain morphology. One possible limitation to the grain morphology study discussed here is that it involves loading the simulation volume just until the yield point of the material. This may result in the location of stress localizations to change if the material is subject to higher amount of plasticity, bringing about noticeable differences in the two meshes. At the same time it must be noted that due to the varying grain orientations within the sample, a number of grains do actually plasticize, so these conclusions should be valid for different loading conditions, involving higher plasticity.

3.8 Additional data: Further validating the methodology to incorporate residual stresses

In addition to comparing the results of the CPFE simulations with initialized residual stresses to experimental data from HEDM experiments (as discussed in Section 3.6 and 3.7), another method to validate the procedure to incorporate residual stresses is by initializing a known value of a stress field as a residual stress and seeing the distribution of the stress after letting it equilibrate. Out of a number of possible stress fields, a well-known stress field is the one associated with an edge dislocation. This validation process involves initializing the stresses in the finite element mesh corresponding to the stress associated with an edge dislocation in each finite element and letting the stresses equilibrate. The results of this simulation, i.e. stresses, after they equilibrate are shown in Fig. 3.13.

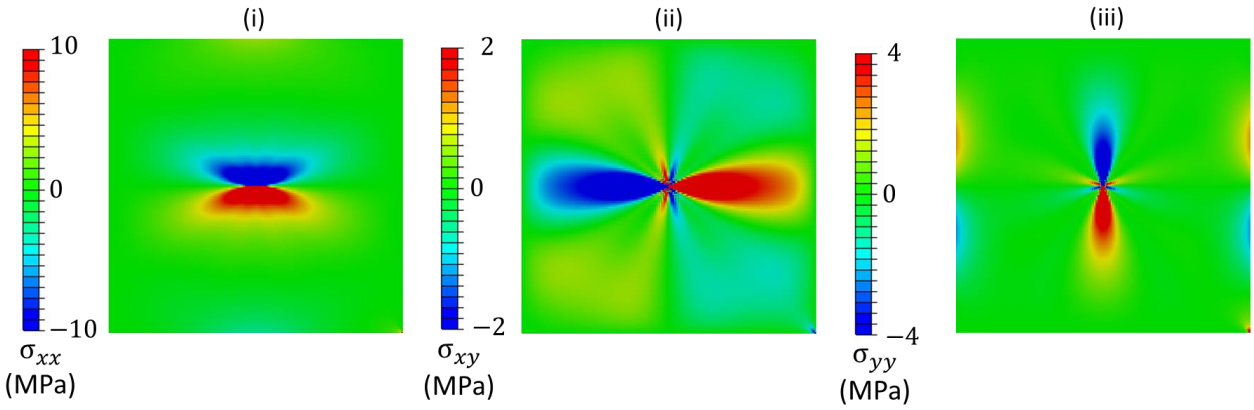

Figure 3.13. Stress distribution after equilibration for an initialized residual stress for an edge dislocation: (i) σ_{xy}, (ii) σ_{xy}, and (ii) σ_{yy}.

It can be seen that the stress distribution from the Fig. 3.13 follows the distribution that is expected in the case of edge dislocations, and hence these simulation serves as a good check for the model.

CHAPTER 4. INCORPORATING GRAIN-LEVEL RESIDUAL STRESSES AND VALIDATING A CRYSTAL PLASTICITY MODEL OF A TWO-PHASE TI-6AL-4V ALLOY PRODUCED VIA ADDITIVE MANUFACTURING

In this chapter, an experimentally validated CPFE model is developed for Ti-6Al-4V manufactured via selectively laser melting (SLM) which explicitly accounts for both the phases of the material. A realistic FE mesh of the dual phase alloy is generated based on a combination of EBSD and BSE characterization (carried out by Dr. Todd Book), which provides information necessary to segregate and represent the two phases. In addition, TEM analysis (carried out by Jeremy Yoo and Dr. Josh Kacher at Georgia Tech) is utilized to investigate the distribution of dislocation densities in the alloy, which in turn is used to further inform the model. The experimental validation is carried out by comparing the strain distribution obtained from the simulations with HR-DIC experiments. Finally, the strain distribution is used to investigate regions of high strain localization, which may correspond to possible sites for damage initiation.

4.1 Material and characterization

4.1.1 Material

The material in consideration is Ti-6Al-4V, a widely used dual phase titanium alloy, produced via SLM. The samples used for the current work were manufactured at Penn State University's Center for Innovative Materials Processing (CIMP-3D) using an EOSINT M280 system. The manufacturing process involved building vertical blocks and then machining dog bone specimens via electron discharge machining (EDM). To reduce the amount of residual stress and potential part distortion present in the specimens, two treatments were applied. The first was a stress relief process in vacuum at 650˚ C for 3 hours prior to cutting the samples from the build plate. Afterwards the specimens were mill annealed in vacuum at 704˚C for 2 hours followed by cooling in Argon. At this time we would like to point out that the region of interest for HR-DIC (including EBSD and BSE) and CPFE simulations was approximately a square of 100 μm at the center of the dog bone specimen. This area contains fiducial markers using micro-indentation at the corners to track the region of interest throughout DIC imaging. The images shown in this paper

correspond to an area after removing the fiducial markers and hence are squares with sides of ~75 μm. Additional details about manufacturing the sample can be found in [87].

4.1.2 EBSD and BSE characterization

For brevity, EBSD and BSE techniques are discussed here in brief and more details about these two characterization techniques for this same material can be found in [87]. The received samples were first polished and cleaned for EBSD scanning, which was carried out using an FEI XL-40 scanning electron microscope (SEM) with an EDAX EBSD camera and associated data collection and analysis software. The parameters used to carry out EBSD consisted of a step size of 0.20 μm with a gain of 12.60, a black of 1.51 and the exposure time being 31.97 ms. This EBSD data was directly utilized for generating a realistic FE mesh and calculating the initial GND density, both of which are direct inputs into the CPFE model and will be discussed in detail in the following sections.

EBSD was followed by BSE imaging on the same region of interest within the specimen. The primary reason to conduct BSE imaging was to distinguish between the phases present in the materials: the α (HCP) and the β (BCC) phases, since the material in consideration is a dual phase alloy. This is important as we model the α and the β phases explicitly within the crystal plasticity framework. The BSE imaging was carried out on a FEI Quanta 3D scanning electron microscope at 10,000× magnification, accelerating voltage of 15 kV, spot size of 4.5 and a working distance of 5 mm.

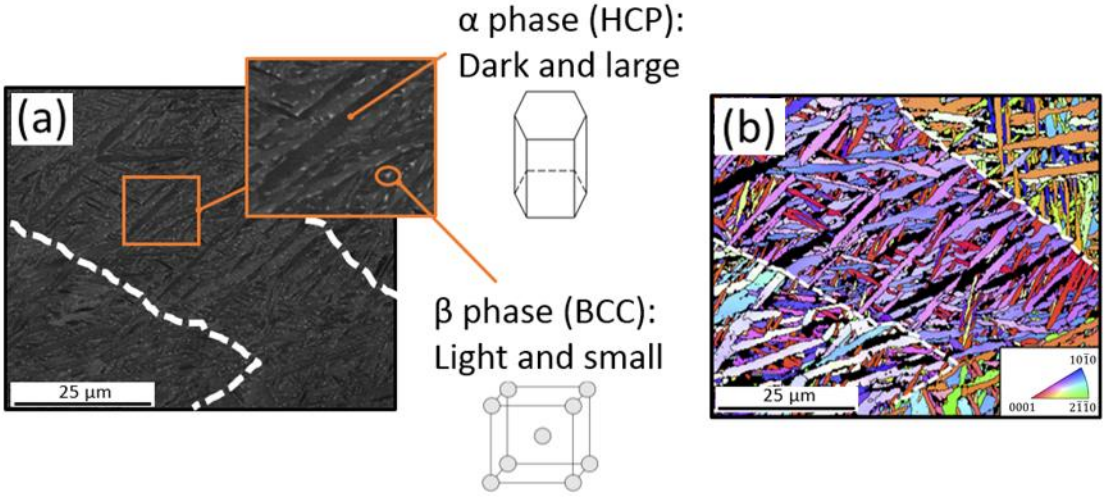

Figure 4.1. Experimental characterization: (a) Backscatter electron image (b) Inverse pole figure (for the α phase) for the region of interest in the sample

The BSE image and inverse pole figure (IPF) plot obtained from EBSD are shown in Fig. 4.1 (a) and (b), respectively. The BSE image is utilized to distinguish between the two phases present in the material: the dark regions correspond to the α (HCP) phase and the light white region is the β (BCC) phase. EBSD scans provide important crystallographic information like grain orientation, morphology and size which are utilized to generate a realistic microstructural FE mesh. The EBSD characterization was carried out only on the α (HCP) phase of the material, as the β (BCC) phase is extremely small in size and hence not feasible to be indexed using the available EBSD system, along with the α phase, in a reasonable amount of time using the current system. It is pointed out that it is feasible to explicitly characterize dual phase alloys with the appropriate translational stages and detectors [110]. Another important and interesting feature noticeable in this material is the presence of highly textured regions which are commonly referred to as prior β grains or macrozones. These regions can be visually observed as clusters of grains with similar orientations in the IPF plots shown in Fig. 4.1b and for clarity, have been indicated using superposed dashed white lines.

4.1.3 Transmission electron microscopy

To investigate the dislocation interactions and distributions in the microstructure as well as the local β-phase distribution, focused ion beam (FIB) lift-out procedure was used to prepare transmission electron microscopy (TEM) samples. FIB machining was performed with a FEI Nova Nanolab 200 FIB/SEM to prepare the TEM samples, which extended approximately 10 μm away from the surface. Two FIB lift-out samples were prepared: one from the grip section of the dog bone sample and one from a region of high strain localization (based on the HR-DIC results). The grip section was chosen as a damage-free region to study the native microstructure of the material. Annular dark field (ADF) scanning transmission electron microcopy (STEM) images were acquired using a FEI Tecnai F30 at 300 kV acceleration voltage at various camera lengths. Like the BSE images, the STEM image (Fig. 4.2) is also able to distinguish between the α and the β phases based on the gray scale values, reinforcing the effectiveness of using gray scale values to separate the two phases.

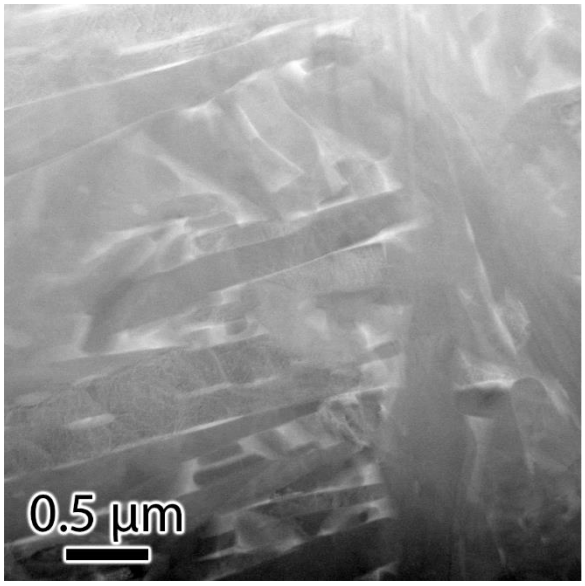

Figure 4.2. ADF STEM image differentiating the α-phase (dark) from the β-phase (light) with lift-out from the grip section.

4.1.4 Fatigue experiments and High Resolution Digital Image Correlation

The dog bone specimens were subject to cyclic loading followed by HR-DIC to obtain a strain distribution in the region of interest after loading. The specimens were first loaded to a strain of 1% and then cycled using stress control at the maximum stress achieved at 1% displacement with an R ratio of 0.05 at 1 Hz for 1000 cycles. SEM imaging was carried out on the region of interest before and after loading the specimen, in order to perform HR-DIC. This was preceded by sample preparation which involved speckling the sample using Au nano-particles, as described in [111,112]. The samples were soaked in Au nano-particle solution for 5 to 10 days to develop a dense pattern that was suitable to carry out HR- DIC. The imaging was carried out using a FEI Quanta 3D SEM at a magnification of 8000x with an aperture size of 30 µm, an accelerating voltage of 5 kV, spot size of 5 with a 10 mm working distance. The step size for strain correlation was 0.037 µm with a subset of 1.1749 µm. The detailed experimental procedure can be found in [87]. Since imaging with SEM involves electromagnetic fields and the time taken to image the specimen might be significant, distortion correction was accounted for based on the method described in [113].

4.2 Crystal Plasticity simulations

One of the main goals of this work is to develop a reliable and experimentally validated CPFE model capable of providing information about strain (and hence stress) distribution within the region of interest (i.e. region being simulated). The entire process involves establishing a crystal plasticity model and a microstructural finite element mesh, both of which need to be physically realistic and representative of the material in consideration. The main advantage of the CPFE model developed in this work is that both the α and β phases of the alloy are modeled explicitly and the simulations are carried out on a FE mesh created directly from a EBSD and BSE characterization and hence represents the actual material. The CPFE model and the procedure of generating the FE mesh are discussed in detail below.

4.2.1 Crystal Plasticity model

The CPFE model presented here is a phenomenological rate dependent model similar to the ones developed by [6,20,27,104,105] that has been modified to incorporate GNDs making it physically relevant. This is implemented in a user material subroutine (UMAT) within a commercial finite element code, Abaqus. Since both the α and phases are explicitly accounted for, two separate sets of slip systems and CPFE parameters are needed for the two phases.

The kinematics of the deformation are captured by the standard multiplicative decomposition of the deformation gradient as follows.

$$\mathbf{F} = \mathbf{F^e}.\mathbf{F^p} \tag{4.1}$$

With $\mathbf{F}$ being the total deformation gradient and $\mathbf{F^e}$ and $\mathbf{F^p}$ being its elastic and plastic parts, respectively. The plastic velocity gradient in the intermediate configuration is given by the following equation:

$$\mathbf{L^P} = \dot{\mathbf{F}}^{\mathbf{p}}.(\mathbf{F^p})^{-1} = \sum_{\mathbf{i=1}}^{\mathbf{N_{sys}}} \dot{\boldsymbol{\gamma}}^{\mathbf{i}}(\mathbf{s_0^i} \otimes \mathbf{n_0^i}) \tag{4.2}$$

With s_0^i, n_0^i and $\dot{\gamma}^i$ being the slip plane direction, slip plane normal and the shearing rate for the i^{th} slip system, respectively. The flow rule, relating the shearing rate on a slip system to the resolved shear stress is represented using a power law [20] as follows:

For the α phase:

$$\dot{\boldsymbol{\gamma}}^{\mathbf{i}} = \dot{\boldsymbol{\gamma}}_{\mathbf{0}} \left\langle \frac{|\boldsymbol{\tau}^{\mathbf{i}} - \boldsymbol{\chi}^{\mathbf{i}}| - \mathbf{K}^{\mathbf{i}}}{\mathbf{D}^{\mathbf{i}}} \right\rangle^{\mathbf{m}} \mathbf{sgn}\left(\boldsymbol{\tau}^{\mathbf{i}} - \boldsymbol{\chi}^{\mathbf{i}}\right) \tag{4.3}$$

For the β phase:

$$\dot{\boldsymbol{\gamma}}^{\mathbf{i}} = \dot{\boldsymbol{\gamma}}_{\mathbf{0}} \left\langle \frac{|\boldsymbol{\tau}^{\mathbf{i}}| - \mathbf{K}^{\mathbf{i}}}{\mathbf{D}^{\mathbf{i}}} \right\rangle^{\mathbf{m}} \mathbf{sgn}\left(\boldsymbol{\tau}^{\mathbf{i}}\right) \tag{4.4}$$

In the above equations, $\langle\ \rangle$ denotes Macaulay brackets with τ^i, D^i, χ^i and K^i being the resolved shear stress, slip system resistance, backstress and the threshold stress for the i^{th} slip system, respectively. $\dot{\gamma}_0$ and m are the reference shearing rate and strain rate sensitivity, respectively, kept constant for all the slip systems. Recent literature suggests that the prismatic and basal strain rate sensitivities for α-β Ti alloys may not be the same, as shown by (Zhang et al., 2016a; Zhang et al., 2016b; Chatterjee et al., 2017). However for this work, the strain rate sensitivities are taken to be the same for the various slip systems for the simplicity of fitting the crystal plasticity parameters coupled with the unavailability of the strain rate data for the exact alloy in consideration.

The threshold stress may be further broken down into an evolving and a non-evolving component as follows.

$$\mathbf{K}^{\mathbf{i}} = \frac{\mathbf{K}_{\mathbf{y}}^{\mathbf{i}}}{\sqrt{\mathbf{d}_{\mathbf{avg}}}} + \mathbf{K}_{\mathbf{s}}^{\mathbf{i}} \tag{4.5}$$

K_y^i is a non-evolving constant, and d_{avg} is the average grain diameter. This type of equation takes the form of the Hall-Petch relation [114,115] that accounts for hardening due to grain size effects making the CPFE model grain size dependent. K_s^i evolves according to the following equation.

$$\dot{\mathbf{K}}_{\mathbf{s}}^{\boldsymbol{\iota}} = -\boldsymbol{\lambda}\mathbf{K}_{\mathbf{s}}^{\mathbf{i}}\left|\dot{\boldsymbol{\gamma}}^{\boldsymbol{i}}\right| \tag{4.6}$$

The slip system resistance is a non-evolving constant as hardening is accounted for by the threshold stress and backstress.

$$\dot{\mathbf{D}}^{\mathbf{i}} = \mathbf{0} \tag{4.7}$$

The backstress for the α phase is calculated using the following equation, and is kept constant for a given time step.

$$\boldsymbol{\chi^{i} = A * \mu * b^{i} \sqrt{\rho^{i}_{GND}}} \tag{4.8}$$

Where b^{i} and ρ^{i}_{GND} are the Burgers vector and the GND density for the i^{th} slip system. A is a scalar constant and μ is the isotropic shear modulus of the material. The method to calculate the GND density is explained in detail in Section 4.2.2. Due to its small volume fraction, the backstress term in the β phase is considered negligible.

Even though the basal and prismatic slip systems are the dominant ones for the α phase at room temperature, to incorporate all the possible deformation modes, a total of 24 slip systems: 3 $(0001)\langle 11\bar{2}0\rangle$ basal, 3 $\{10\bar{1}0\}\langle 11\bar{2}0\rangle$ prismatic, 6 $\{10\bar{1}1\}\langle 11\bar{2}0\rangle$ 1st order pyramidal and 12 $\{10\bar{1}1\}\langle 11\bar{2}3\rangle$ 2nd order pyramidal systems have been incorporated within the model. For the β phase, in addition to the 12 $\{110\}\langle 111\rangle$ slip systems that are active at room temperature, 12 $\{112\}\langle 111\rangle$ slip systems are incorporated in order to provide more degrees of freedom to the β phase. It should be noted that the CRSS and other CPFE parameters are kept constant for all the 24 BCC slip systems but varied for each family of the HCP phase. The elastic constants and the values for drag stress and threshold stress for the α phase are based on the values used in [46]. The elastic constants for the β phase are taken from [116]. The values of the CPFE parameters and the elastic constants for both the phases are given in Table 4.1.

Table 4.1. Crystal plasticity parameters utilized in the simulations

Parameter	***Value***		
	α (HCP)		**β (BCC)**
$\dot{\gamma}_0$	0.01		0.01
m	15		15
CRSS (MPa)	Basal	420	370
	Prism	370	
	Pyramidal-1	490	
	Pyramidal-2	590	
D (MPa)	Basal	148	98
	Prism	98	
	Pyramidal-1	218	
	Pyramidal-2	318	
d_{avg} (μm)	2.15		0.17
K_y ($MPa*\sqrt{\mu m}$)	178.89		50.30
K_s (MPa)	150		150
λ	15		15
A	0.4		--
μ (MPa)	46000		--
C_{11} (MPa)	162400		135000
C_{12} (MPa)	92000		113000
C_{44} (MPa)	49700		54900
C_{13} (MPa)	69000		--
C_{33} (MPa)	180700		--

4.2.2 Incorporating residual stresses via GNDs

As discussed earlier, the presence of residual stresses at the grain-scale may be linked to higher GND density in a given region. For this reason, GND densities have been incorporated into the current model as a means to account for the effects of residual stress. The process of incorporating the GND density in the model is as follows. After each time step of the CPFE simulation, the Nye tensor is equated to the open Burgers circuit [117] using the equation below:

$$\sum_{\mathbf{i=1}}^{\mathbf{N}} \boldsymbol{\rho}_{\mathbf{GND}}^{\mathbf{i}} \mathbf{b}^{\mathbf{i}} \otimes \mathbf{t}^{\mathbf{i}} = \mathbf{Curl}\left(\mathbf{F}^{\mathbf{P}}\right) \tag{4.9}$$

Where ρ_{GND}^{i}, b^{i} and t^{i} are the GND density, Burgers vector and the tangent vector for the i^{th} GND type with $\mathrm{N} = 33$ GND densities: 24 edge + 9 screw for the HCP phase. The equation is solved by using a least squares minimization method [118], which results in a solution that geometrically corresponds to the least dislocation line lengths [117]. Though it may be argued that using an energy minimization method instead of a least squares approach would be more physically relevant to solve the above equation, it must be noted that the least squares minimization scheme is easy to implement and is suitable for our purposes. Since in the current model, the primary effect of the GND density results in the hardening of the slip systems via the backstress term (which includes a scaling constant) and does not affect the model in any other way, getting exact values of GND densities is not a primary concern.

One of the primary difficulties for this modeling approach is to incorporate GND densities into CPFE models implemented in Abaqus, because calculating the curl (determined from spatial derivatives) requires knowledge of the deformation gradient of neighboring integration points at any given time. However, if the model is implemented within a UMAT, which is the most popular and convenient method to incorporate material models within Abaqus, there is no way to know neighbor information for a given material point. One method is to use a user element subroutine as in [58] but implementing material models is much easier utilizing a UMAT. In the current work, a simple feasible workaround is presented which involves storing neighbor information in files which is updated after every time step. Though time involved in writing files may increase the simulation time, it is not substantial and writing files is a simple and robust way to implement GND densities into CPFE models.

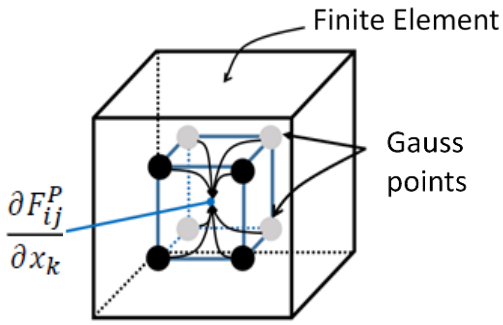

Figure 4.3. Calculating derivatives within a finite element at the element center using shape functions

Calculating the curl requires evaluating the spatial derivatives of the deformation gradient for points within the FE mesh. Derivatives are calculated as shown in the schematic in Fig. 4.3. Since the FE mesh utilizes hexahedron elements, each element has 8 integration or material points. An imaginary element can be constructed with these integration points and all the derivatives and the associated curl can be calculated at the center of this pseudo-element (and hence the actual finite element as both have the same center) using FE shape functions. This value of the curl and hence GND density is kept constant for a given finite element.

Since the material in consideration has initial residual stresses, it will have an initial GND density based on the relation between residual stress and GND density discussed earlier. This initial GND density can be evaluated from the EBSD orientation maps by relating the curl of the orientation field to Nye's dislocation tensor, details can be found in [119] [120]. The local GND density is then calculated by taking the norm of Nye's dislocation density tensor, with a weighting factor to account for the terms unavailable due to the two dimensional nature of EBSD scans. More details of this approach can be found in (Ruggles and Fullwood, 2013). As the scans were acquired using traditional EBSD rather than high angular resolution EBSD, the angular resolution was considered sufficient for total GND density calculations but not their resolution onto individual slip systems [121,122]. The total GND density calculated for the α (HCP) phase is shown in Fig. 4.4.

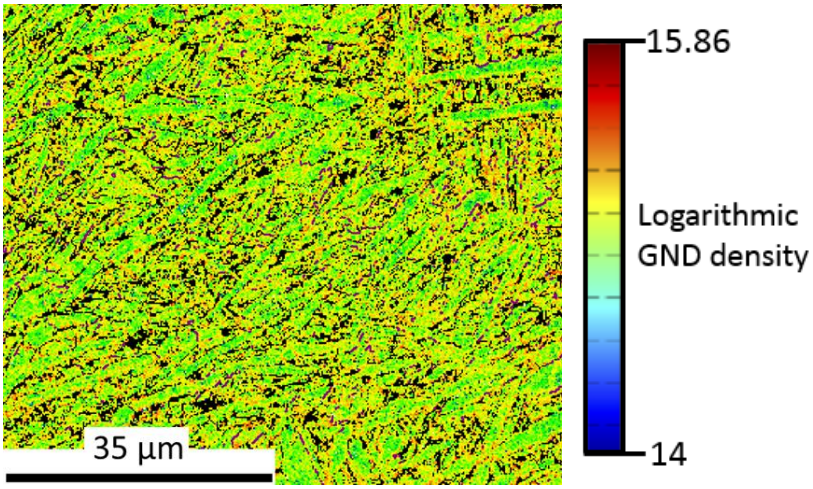

Figure 4.4. Distribution of total GND density in the region of interest within the sample

Only the total GND density at a given material point can be calculated using this approach and not the GND density on individual slip systems. To estimate the GND density on each slip system, some approximations are used. It has been observed that in Ti-6Al-4V, on an average, the GND density of the <a> type slip systems are around ~10 times higher than that of the <c+a> systems [76]. Based on this assumption, the total initial GND densities may be divided into densities on individual slip systems which are then used to initialize the CPFE model. This assumption will later be reevaluated by investigating the dislocation density content on <a> and <c+a> dislocations using TEM studies, albeit TEM is not ideal for extracting statistical level information.

In addition to initializing GND densities, another method to incorporate residual stresses that involves the triple decomposition of the total deformation gradient [88] may be utilized as follows. At the beginning of the CPFE simulation, since only residual stresses exists in the material, with the material not having undergone any deformation, the value of the total deformation gradient at the start of the simulation will be the identity tensor, I.

$$\mathbf{F} = \mathbf{I} \tag{4.10}$$

But since initial residual stresses are non-zero, the elastic part of deformation gradient ($\mathbf{F^e}$), which contributes to the stress field will be non-identity at the beginning of the initial time step.

$$\mathbf{F^e} \neq \mathbf{I} \tag{4.11}$$

The only way to ensure that $\mathbf{F}$ is equal to the identity tensor along with $\mathbf{F}^{e}$ having a non-identity value using the standard elastic-plastic decomposition of the deformation gradient is by ensuring $\mathbf{F}^{\mathbf{P}}$ is not equal to the identity tensor. Physically, this will translate into the fact that the residual deformation is accounted for by the plastic part of the deformation gradient. However it may be argued that the residual stress is an elastic response to prior irreversible deformation and hence $\mathbf{F}^{\mathbf{P}}$ should also be set as the identity tensor (no plastic deformation). To ensure this, a triple decomposition of the deformation gradient is proposed as follows.

$$\mathbf{F} = \mathbf{F}^{\mathbf{e}}\mathbf{F}^{\mathbf{R}}\mathbf{F}^{\mathbf{P}} \tag{4.12}$$

This decomposition resembles the elastic-plastic decomposition but differs since $\mathbf{F}^{\mathbf{R}}$ is introduced to ensure that both $\mathbf{F}$ as well as $\mathbf{F}^{\mathbf{P}}$ have the value of the identity tenor at the beginning of the simulation. A point to note is that the residual stress is generated only due to $\mathbf{F}^{\mathbf{e}}$ and $\mathbf{F}^{\mathbf{R}}$ in no way contributes to the stresses in the material and works as a pseudo Eigen deformation gradient to keep $\mathbf{F}$ and $\mathbf{F}^{\mathbf{P}}$ as identity at the start of the simulation.

4.2.3 Crystal plasticity finite element mesh generation and simulations

As an input to the CPFE model, there is a need to develop a physically realistic mesh that is representative of the material in consideration. Since both the α and the β phases are modeled explicitly, it is important to separate these two phases in the FE mesh. As observed, the two phases can be easily distinguished spatially using the BSE imaging and hence can be separated by thresholding the image as seen in Fig. 4.5. The thresholding process converts the image into binary bins with the black regions being the β phase and the white regions being the α phase. This spatial information about the α and β phases is directly utilized to generate the FE mesh, which is discussed as follows.

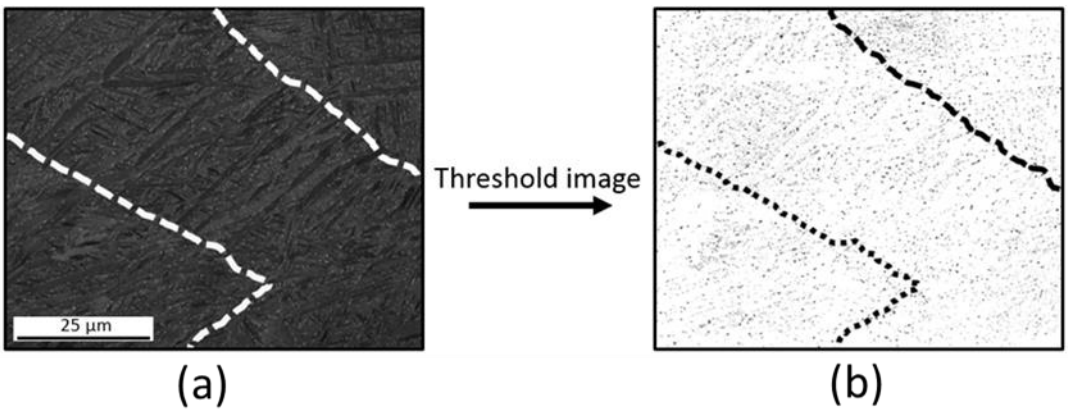

Figure 4.5. Thresholding the BSE image to obtain spatial distribution of the α (light) and the β (dark) phase: (a) before applying the threshold and (b) after applying the threshold. Dotted lines indicate the location of prior β boundaries.

The methodology of developing a FE mesh from EBSD and BSE characterization is shown in Fig. 4.6. The EBSD file is imported into DREAM.3D, an open source data analysis tool, specifically geared towards 3D materials [123]. Using the available α-phase EBSD data, DREAM.3D is utilized to generate a single phase (α) FE mesh composed of hexahedron elements. The generated mesh is then superposed with the binary BSE image which is used to identify whether a given element belongs to the α or the β phase utilizing scripts develop in Matlab followed by assigning the crystallographic orientation to the β phase using the BOR [124]. This process results in a FE mesh with hexahedron elements for both the α and β phases and the properties of the two being assigned in the UMAT.

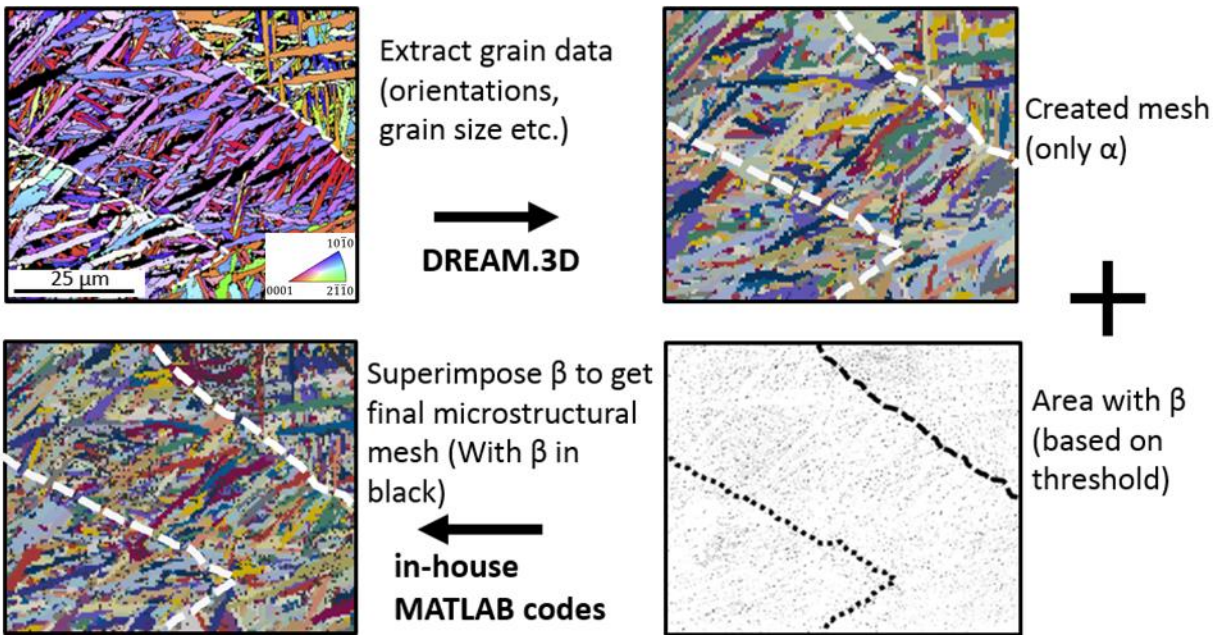

Figure 4.6. Procedure utilized to create FE mesh from material characterization data

As pointed out earlier, EBSD characterization was carried out only for the α phase and hence no information about the crystallographic orientation for the β phase is available. To run the CPFE model, the crystallographic orientation of both phases is required. To resolve the issue of the missing orientation of the β phase, its orientation is deduced based on the well-known BOR [124] that exists between the α and the β phases of Ti alloys. The visual representation of the BOR existing between the two phases is shown below in Fig. 4.7.

Burgers orientation relationship:

$$(0001)_\alpha // \{101\}_\beta$$

$$\langle 11\bar{2}0\rangle_\alpha // \langle 111\rangle_\beta$$

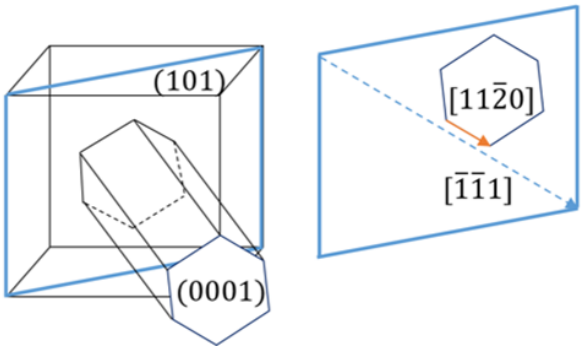

Figure 4.7. Burgers orientation relationship (figure recreated from [96])

The final mesh consists of 288,800 hexahedron elements with an element size of 0.5 µm * 0.5 µm * 1 µm and has a depth of 8 µm in the z-direction (resulting in 8 elements in the thickness). With such a fine mesh, there are more than sufficient elements in each α grain to capture strain localization, with the number of elements in the α grains ranging from a few hundred to a few thousands. The boundary conditions (BCs) applied to the simulation volume correspond to the case of loading the specimen uniaxially in the x-direction, as described by [125]. The region of interest in this work, a square with dimension ~75 µm is a small part of a larger dog bone specimen with a gauge section of 17.5 mm by 3.5 mm. With the material in consideration being a polycrystalline alloy consisting of grains with varying orientations, it may be argued that the simulation volume may be subjected to different BCs as compared to the macroscopic loading due to the neighbor orientation effects. However this effect is minimized as the actual simulation volume is a square of sides ~95 µm, which is bigger than the region of interest with uniaxial BCs being applied to the boundary grains (and not directly on the grains in the region of interest).

Most of the literature with regard to CPFE modeling that involves cyclic loading limit their simulations to a few cycles due to computational limitations which prevents simulating a large number of cycles as is the case with [18,46,126]. This is coupled with the fact that for a number of relevant engineering alloys, the cyclic stress-strain curve stabilizes after a few cycles as in the case of [127,128] and hence it is acceptable in literature to run simulations only until saturation of the macroscopic stress-strain curve is reached. In the current work, it is observed that the experimental stress-strain curve stabilizes fairly quickly, after a few cycles and hence it is sufficient to run simulations for only a few cycles. However, in order for the simulations results to be as close to experiments, the simulations are run for 100 cycles, well beyond the point of saturation of the stress-strain curve.

4.3 Results

The comparison between CPFE and HR-DIC is done using strain maps for the strain in the loading direction as shown in Fig. 4.8 and analyzed in Fig. 4.9. In addition to evaluating the strain maps, the Schmid factors for the basal and prismatic slip systems (slip systems with low CRSS values) for the α phase, calculated based on experimental strains are also plotted. Since the material in consideration is a polycrystalline alloy, it is expected that the local stress state of the grains will

deviate significantly from the global stress state (uniaxial tension in this case) due to grain-neighbor interactions. Therefore to better understand the effect of crystal orientations, local Schmid factors [129] are introduced which are calculated in a similar manner as the nominal Schmid factors, except, instead of using the global experimental uniaxial stress tensor for all the grains, the local averaged stress tensors of individual grains, obtained from CPFE simulation are utilized.

$$\text{CPFE local Schmid factor} = \frac{\sigma : \mathrm{M}}{\sigma_{\text{von Mises}}} \tag{4.13}$$

Where, σ is the averaged stress tensor for a given grain, M is the Schmid tensor, given by $\mathrm{M} = \mathbf{s_0^i} \otimes \mathbf{n_0^i}$ with s_0^i and n_0^i being the slip plane direction and the slip plane normal respectively. The Schmid tensor is used to resolve the stress tensor on to the slip systems to obtain the resolved shear stress $\sigma_{\text{von Mises}}$ is the averaged von Mises stress for a given grain. The basal and prismatic Schmid factors (both local and nominal) are calculated and then plotted (only for the α phase) as shown in Fig. 4.10.

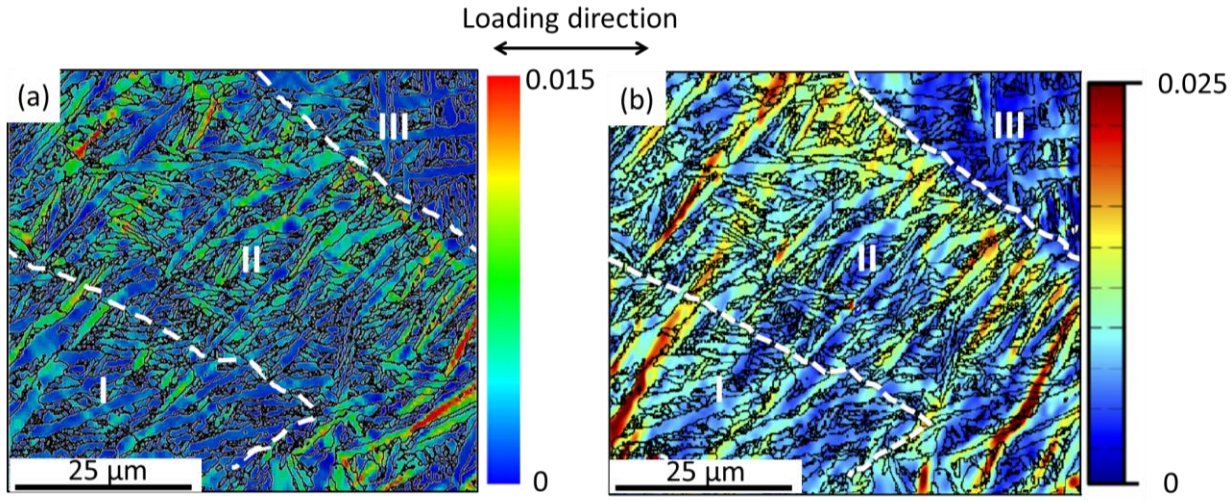

Figure 4.8. Visual comparison between strain maps obtained from (a) CPFE simulations and (b) DIC experiments with overlay of grain boundary map obtained from EBSD

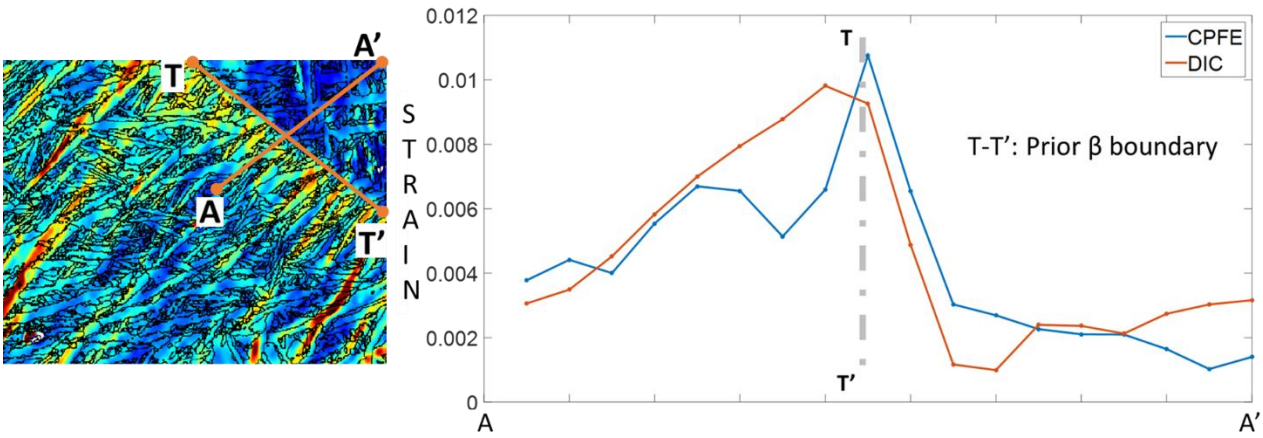

Figure 4.9. Quantitative axial strain (along the loading direction) comparison along a path (Path A-A' shown on the left) across the prior β boundary (T-T') indicating strain localization at the boundary, with the CPFE strains scaled 1.6 times (same as the scale bar in Fig. 4..8) to account for the CPFE simulation being subject to fewer loading cycles compared to the DIC experiments

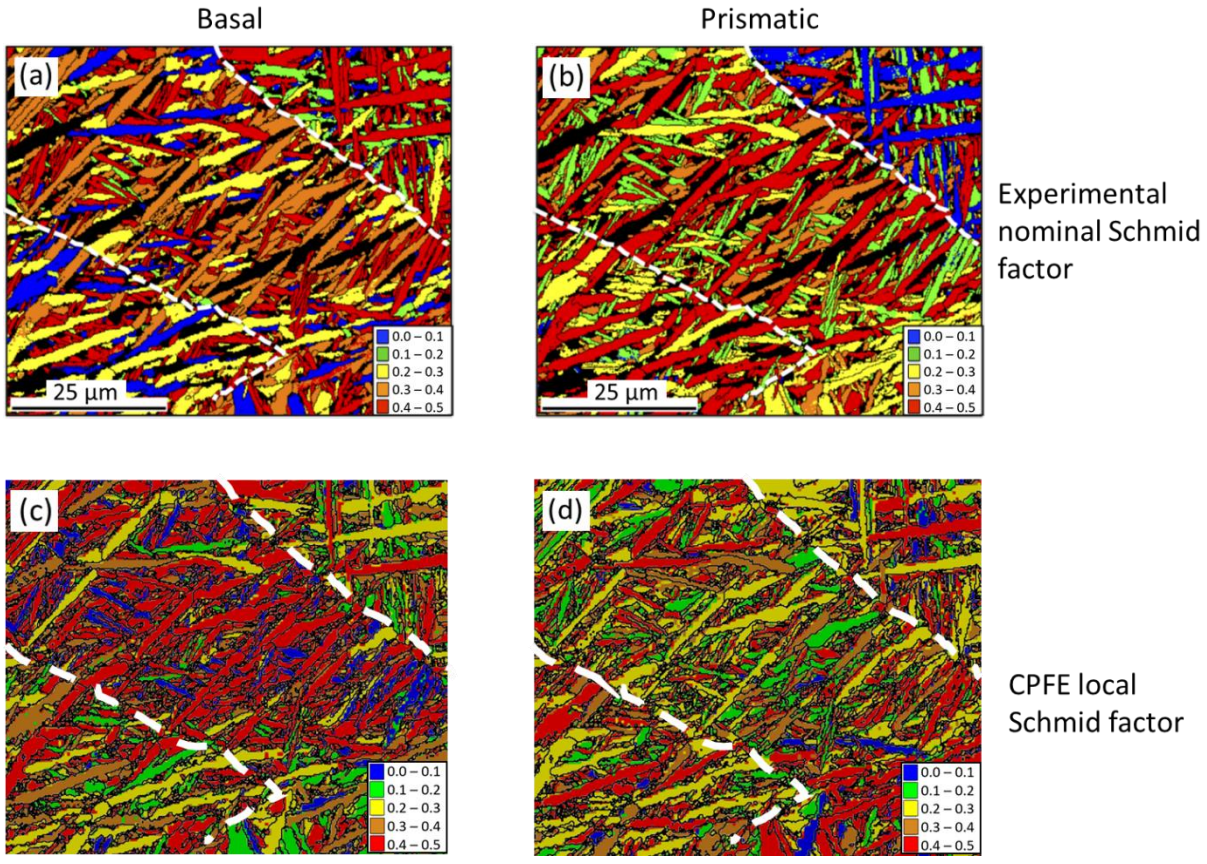

Figure 4.10. Nominal and local Schmid factors compare well with each other as well as the strain in the loading direction shown in Fig. 4.8: (a) nominal basal Schmid factor, (b) nominal prismatic Schmid factors, (c) local basal Schmid factor, and (d) local prismatic Schmid factors, (c) local basal Schmid factor, and (d) local prismatic Schmid factor

Since the effect of residual stresses is incorporated into the simulation via GND densities, which in turn are utilized to calculate the backstress, the evolution of backstress with the number of cycles is investigated. It is observed that the general trend of evolution remains similar across all the slip systems, hence to get an understanding of the evolution behavior, the absolute values of the backstresses on just one slip system ($(1\ \bar{1}\ 0\ 0)\ [1\ 1\ \bar{2}\ 0]$ in this case) are plotted for the first, 20th and the 100th cycle shown in Fig. 4.11.

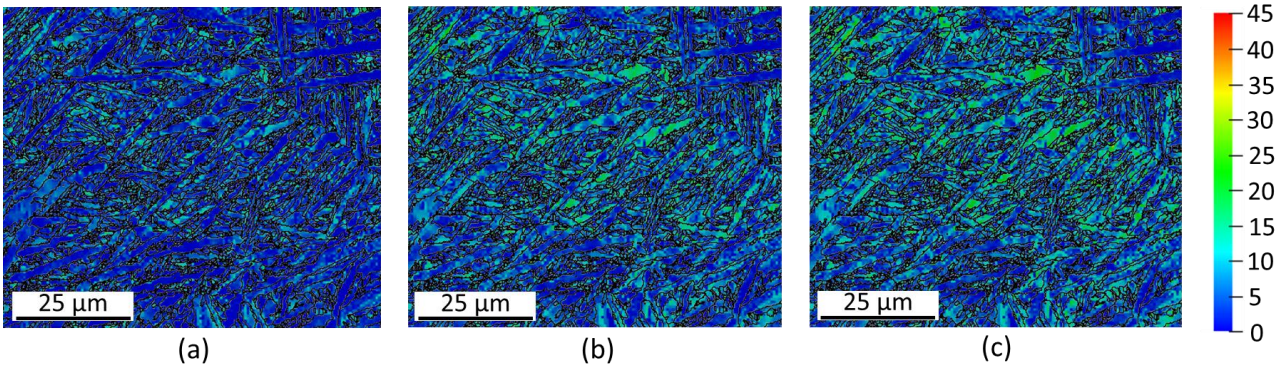

Figure 4.11. Evolution of backstress at the end of (a) cycle-1, (b) cycle-20, and (c) cycle-100 for the $(1\ \bar{1}\ 0\ 0)\ [1\ 1\ \bar{2}\ 0]$ slip system, superposed with grain boundary map obtained from EBSD

In order to identify the dislocation arrangements in the residual stress condition, i.e. prior to loading, and after cyclic loading, TEM analysis is conducted. Fig. 4.12 shows TEM images acquired using a **g** = 0002 two beam bright field condition from the undeformed grip section (Fig. 4.12a) and a high strain region (Fig. 4.12b) machined from the sample after deformation. In this diffraction condition, all <a>-type dislocations are invisible and only <c+a>-type dislocations are present in the image. Interestingly, a large content of <c+a>-type dislocations, higher than what is expected from previous studies on deformed Ti-6Al-4V (Britton et al., 2010), [77], [97] can be seen. These dislocations appear to originate from the α-β interfaces though, as all images were acquired *post mortem*, this cannot be confirmed.

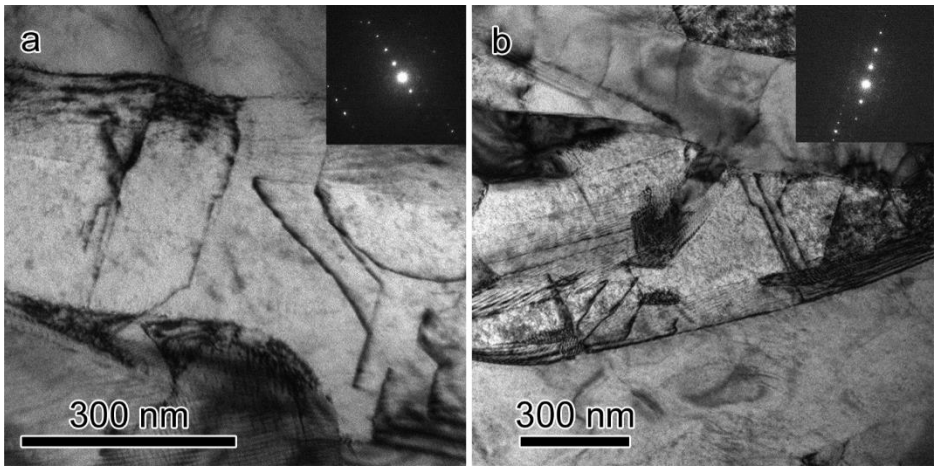

Figure 4.12. Two beam bright field TEM images of <c+a> dislocations from the (a) grip section and (b) high strain region. Insets show diffraction patterns associated with the images.

4.4 Discussion

As can be seen in Fig. 4.8 and Fig. 4.9, there is similar strain patterning between the results obtained from the CPFE simulations and HR-DIC experiments for the strain in the loading direction, specifically the strain accumulation at the prior β boundaries II and III (as can be seen visually and quantitatively in Fig. 4.9). These results are obtained using CPFE parameters that are determined from literature and not fit to the local strain values. If we focus on the model, we see that it is able to capture the physics of the material at the mesoscale due the fact that the α and β phases are modeled explicitly and initial GND densities are introduced in order to account for the effects of the residual stress present in the material. Now coming to the material in consideration, it is well known that α (HCP) crystals are highly anisotropic in their slip behavior with the basal and prismatic slip dominating the slip activity and pyramidal slip systems rarely being activated at room temperatures and low strain values [1], as is the case with this simulation. This highly anisotropic nature of slip in these crystals makes it more likely to agree with the stress obtained from the nominal Schmid factor values [87] and hence more likely for the CPFE model to give better results. Since within the CPFE model, plastic flow takes place when the resolved shear stress on a particular slip system exceeds its CRSS, which translates into the Schmid law. Further evidence of this can be seen in the comparison between regions of high experimental nominal basal/prism Schmid factors and high strain localization along with decent correlation between experimental nominal and CPFEM local Schmid factors, especially for the basal slip systems.

Which is interesting because individual grains within a polycrystal have a heterogeneous stress state due to the neighbor effects and hence in most cases, the stress distribution does not match the experimental nominal Schmid factors. This behavior of the α grains is believed to be partially attributed the surrounding β grains, which are relatively soft and ensure compatibility, but this is the study of ongoing investigation. The evolution of backstress plotted in Fig. 4.11 shows a substantial increase in the value as you move from cycle 1 to cycle 20. However there is very little evolution from cycle 20 to 100 which suggests that the value of backstress saturates. To pin point the cycle number after which the change in backstress is not noticeable, the change in the backstress values, from one cycle to the next is calculated and once there is very little variation between the two, it is assumed the backstress value has saturated. It is observed that the saturation of backstress occurs at around cycle 33. At this point, it will be interesting to compare these results with experimental work related to the evolution of GND densities with cyclic loading. [130] measured the evolution of GND densities in conventional Ti-6Al-4V with number of cycles after 1000 cycles, so a comparison cannot be made with the current study. [131] investigated the evolution of the GND densities in Copper with the number of cycles and observed an increase followed by a decrease after 2 cycles, which is again followed by a slight increase. This result is slightly different from the one observed in this study, however it must be pointed out that the current study focuses on a different material system.

The current CPFE model makes an assumption with regards to the distribution of the total GND densities on different slip systems as discussed in Section 4.2.2. However TEM results, discussed in Section 4.3, show larger quantities of <c+a> dislocations as compared to <a> type dislocations, contrary to what has been observed in literature. [132] point out two ways by which <c+a> dislocations may be generated and those can be near surfaces and interfaces such as grain boundaries or heterogeneous sites in the grain interior. Based on which, we may attribute these GND density trends that deviate from literature to the presence of a higher amount of non-equilibrium dislocation structures in this additively manufactured material due to inherent rapid solidification as compared to conventional manufacturing. It may also be attributed to the presence of micro-pores [79] created during the manufacturing process.

The assumption made to split the total GND densities on to different slip systems was that the quantity of <a> type dislocations are approximately 10 times the <c+a> dislocations. However, since this is not what is observed in the TEM results, the simulations were re-initiated with a

different distribution of GND densities on the available slip systems. The simulations were rerun using the following distribution: <c+a> GND densities being $1/10^{th}$ of <a> type GND densities (original simulation), <c+a> GND densities being $1/5^{th}$ (20 %) of the total GND densities and <c+a> GNDs being 1/2 (50 %) of the total GND densities. The effect of varying the initial GND density on the macroscopic response as well as microscopic state variables like backstress is investigated. It is important to recollect that in addition to the anisotropy in the distribution of GND densities, there is inherent anisotropy that exists among the different slip systems due to the different CRSS values, as seen in Table 4.1. The results indicate that there is negligible change in the macroscopic stress response by changing the distribution of the initial GND density as can be seen in Table 4.2.

Table 4.2. Variation in macroscopic stress

Initial GND density distribution	**Macroscopic stress @ 1% strain**
<c+a> GNDs = 1/10 of <a> (9.1 % of total GND is <c+a>)	1084.84 MPa
20 % of total GND is <c+a>	1084.83 MPa
50 % of total GND is <c+a>	1084.80 MPa

Since the initial GND density directly affects the backstress term in the flow rule, the local crystallographic variable that is investigated is the backstress on the individual slip systems. The average point by point variation of the backstress one of the prismatic slip systems: $(1\ \bar{1}\ 0\ 0)\ [1\ 1\ \bar{2}\ 0]$, between 2 different initial GND density terms is investigated and is shown in Table 4.3.

Table 4.3. Effect on backstress by varying the initial GND density

	Deviation between 9.1 % and 50 % of total GND distributed on <c+a>	**Deviation between 9.1 % and 20 % of total GND distributed on <c+a> (MPa)**
Average deviation	0.23 (MPa)	0.07 (MPa)
Max deviation	9.4 (MPa)	7.7 (MPa)

It is observed that the change in the initial GND density affects the value of the backstress and as expected a higher GND density results in higher backstress. Though there is a reasonable change in the backstress value due to the presence of initial GNDs, it is not significant enough to cause changes to the macroscopic response and local strain distribution. Tables 4.2 and 4.3 represent the average variation in the GND density distribution when doing a point by point comparison of the quantities on the surface of the simulation volume for different simulations. In addition to this average backstress variation, the difference in localized backstress values is investigated for the 1st and 100th cycle (well beyond the macroscopic stress-strain curve saturation). There is no difference in the trends for the 1st and 100th cycle, hence only the 1st cycle is shown. The initial GND density on all the slip systems is varied in these simulations and hence we investigate the effects on both the prismatic and pyramidal slip systems. Since there is no variation observed in the trends in evolution of backstress for the three prismatic slip systems, we plot the evolution of backstress on just one of the prismatic slip systems: $(1\ \bar{1}\ 0\ 0)\ [1\ 1\ \bar{2}\ 0]$ in Fig. 4.13. Now coming to the pyramidal slip systems, since we are interested in <c+a> dislocations, which correspond to the 2nd order pyramidal slip system, one of the 2nd order pyramidal slip system, the $(0\ \bar{1}\ 1\ 1)\ [1\ 1\ \bar{2}\ 3]$ system is displayed in Fig. 4.13.

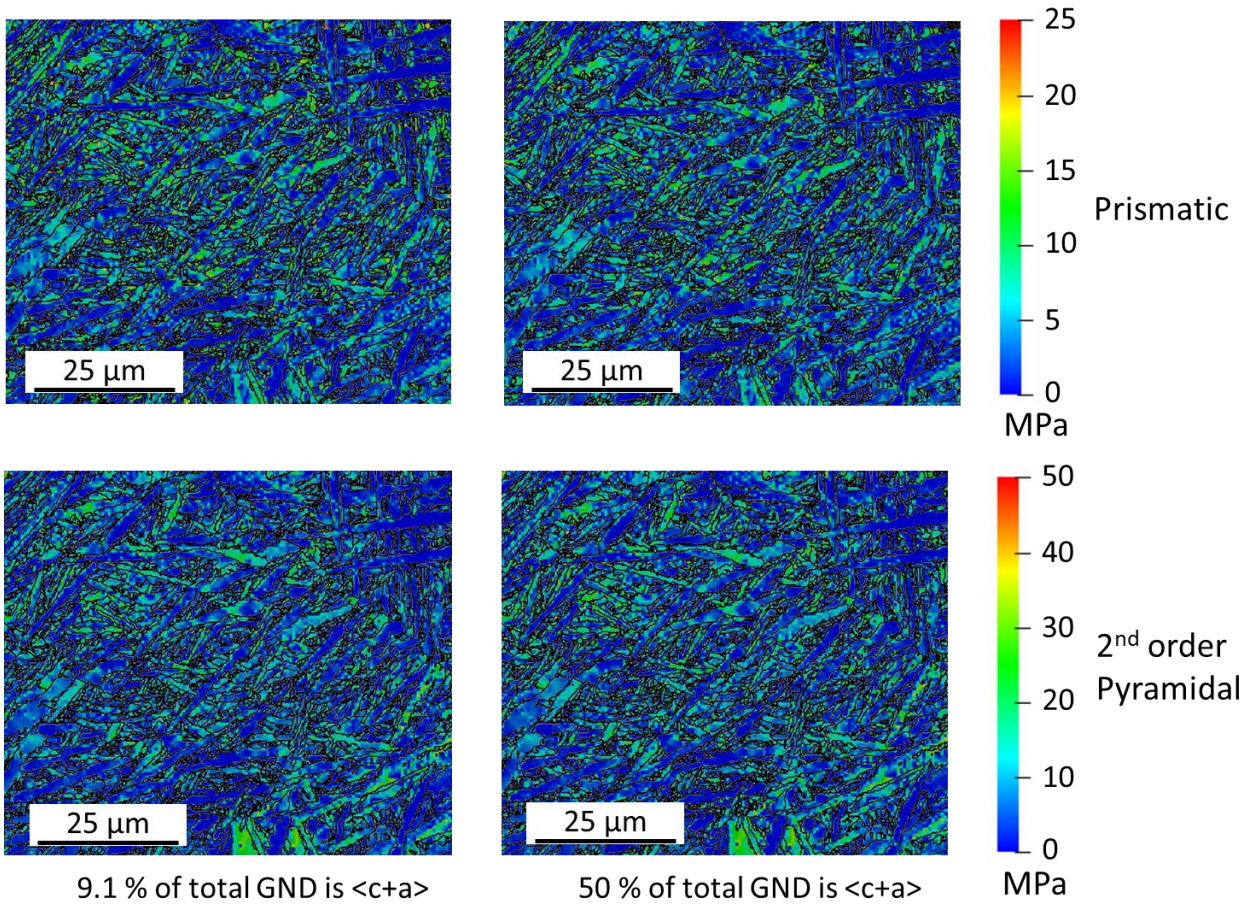

Figure 4.13. Effect of varying the initial GND density on the evolution of backstress after the first cycle

Looking at the backstress distribution after the first cycle in Fig. 4.13, we observe that there is an increase/decrease in the backstress value by increasing/decreasing the GND density on that specific slip system, however the change is negligible. This suggests that the total GND density plays a significant role and the distribution of the density on the slip systems does not greatly influence the backstress value. Similar trends are observed for the 100th cycle and hence not plotted.

It has been widely reported that strain localization is a precursor to fatigue crack initiation [133,134] and hence the regions of strain localization are investigated in the strain map shown in Fig. 4.8. High amounts of strain localization is observed at prior β boundary-II and III and similar kind of strain localization is not observed across prior β boundary-I and II. This is important and suggests that prior β boundaries play a significant role in strain localization in this material. To understand this further, we analyze the average orientation of the prior β grains: The prior β I, II

and III have average Euler angles of [148.6, 59.2, 173.5], [155.3, 56.2, 179.8] and [135.3, 58.6, 217.0], respectively, with the misorientations between prior β I and II being 11.8^{o} and that between prior β II and III being 31.3^{o}. One possible explanation for the high strain localization across prior β II and III may be attributed to the relatively large misorientation between the two as compared to across prior β I and II. This strain localization across the prior β II and III and not across prior β I and II is a very substantial result as it is possible to control the prior β boundaries with the processing parameters of the manufacturing process itself, and therefore redistribute strain localization thereby affecting the fatigue behavior of these materials.

CHAPTER 5. MODELING TI-6AL-4V USING A CRYSTAL PLASTICITY MODEL CALIBRATED WITH MULTI-SCALE EXPERIMENTS TO UNDERSTAND THE EFFECT OF THE ORIENTATION AND MORPHOLOGY OF THE ALPHA AND BETA PHASES ON TIME DEPENDENT CYCLIC LOADING

This work aims to develop a fully calibrated and versatile CPFE model that can be used to gain a comprehensive understanding of deformation behavior of complex heterogeneous Titanium alloys based on the crystal plasticity perspective, with microstructure features as an input. In this work, a three-dimensional crystal plasticity model for a dual phase Titanium alloy, Ti-6Al-4V, explicitly accounting for both the phases (α and β) of the material is developed and implemented in a finite element framework. A systematic method using experimental data in the form of stress-strain curves from specimen level tension tests (provided by Pratt & Whitney) coupled with lattice strains on different crystallographic planes for the individual α and β phases, obtained from High Energy X-ray diffraction experiments (in collaboration with Priya Ravi) is used to calibrate the CPFE parameters of the model. Finally, the fully calibrated CPFE model is used to gain a comprehensive understanding of the effect of the microstructure following the BOR or deviating from it on dwell and high cycle fatigue.

5.1 Crystal Plasticity Model and realistic Finite Element mesh creation

The crystal plasticity model presented in this work is the extension of the phenomenological, rate dependent model used by [46,47,89] and is implemented in a commercially available finite element software, Abaqus via the user material (UMAT) subroutine. The details of the model are as follows.

The kinematics of the deformation are captured by the standard multiplicative decomposition of the deformation gradient.

$$\mathbf{F} = \mathbf{F^e F^p} \tag{5.1}$$

Where $\mathbf{F}$ is the total deformation gradient and $\mathbf{F^e}$ and $\mathbf{F^p}$ are its elastic and plastic parts, respectively. The plastic velocity gradient in the intermediate configuration is given by the following equation:

$$\mathbf{L^P} = \dot{\mathbf{F}}^{\mathbf{p}}(\mathbf{F}^{\mathbf{p}})^{-\mathbf{1}} = \sum_{\mathbf{i=1}}^{\mathbf{N_{sys}}} \dot{\boldsymbol{\gamma}}^{\mathbf{i}}(\mathbf{s_0^i} \otimes \mathbf{n_0^i}) \tag{5.2}$$

With s_0^i, n_0^i and $\dot{\gamma}^i$ being the slip plane normal, slip plane direction and the shearing rate for the i^{th} slip system, respectively. The flow rule, relating the shearing rate on a slip system to the resolved shear stress is represented using a power law [20] as follows:

$$\dot{\boldsymbol{\gamma}}^{\mathbf{i}} = \dot{\boldsymbol{\gamma}}_{\mathbf{0}} \left\langle \frac{|\boldsymbol{\tau}^{\mathbf{i}} - \boldsymbol{\chi}^{\mathbf{i}}| - \mathbf{K}^{\mathbf{i}}}{\mathbf{D}^{\mathbf{i}}} \right\rangle^{\mathbf{m}} \mathbf{sgn}\left(\boldsymbol{\tau}^{\mathbf{i}} - \boldsymbol{\chi}^{\mathbf{i}}\right) \tag{5.3}$$

In the above equations, $\langle\ \rangle$ denotes Macaulay brackets, defined by with $\langle x\rangle = x$ for $x \leq 0$ and $\langle x\rangle = 0$ for $x > 0$. τ^i, D^i, χ^i and K^i are the resolved shear stress, slip system resistance, backstress and the threshold stress for the i^{th} slip system, respectively. $\dot{\gamma}_0$ and m are the reference shearing rate and strain rate sensitivity, respectively, kept constant for all the slip systems.

The threshold stress may be further broken down into an evolving and a non-evolving component.

$$\mathbf{K}^{\boldsymbol{i}} = \frac{\mathbf{K_y^i}}{\sqrt{\mathbf{d_{avg}}}} + \mathbf{K_s^i} \tag{5.4}$$

K_y^i is a non-evolving constant, and d_{avg} is the average grain size. This type of equation takes the form of the Hall-Petch relation [114,115], that accounts for hardening due to grain size effects making the CPFE model grain size dependent. K_s^i evolves according to the following equation.

$$\dot{\mathbf{K}}_{\mathbf{s}}^{\boldsymbol{i}} = -\boldsymbol{\lambda}\mathbf{K_s^i}\left|\dot{\boldsymbol{\gamma}}^{\boldsymbol{i}}\right| \tag{5.5}$$

The slip system evolves according to the following equation.

$$\dot{\mathbf{D}}^{\mathbf{i}} = \mathbf{H}\sum_{\mathbf{j=1}}^{\mathbf{N}} \mathbf{q}^{\mathbf{ij}}\left|\dot{\boldsymbol{\gamma}}^{\mathbf{j}}\right| - \mathbf{H_D}\mathbf{D}^{\mathbf{i}}\sum_{\mathbf{j=1}}^{\mathbf{N}}\left|\dot{\boldsymbol{\gamma}}^{\boldsymbol{j}}\right| \tag{5.6}$$

The backstress evolves according to the following equation:

$$\dot{\boldsymbol{\chi}}^{\boldsymbol{\alpha}} = \mathbf{A}\dot{\boldsymbol{\gamma}}^{\boldsymbol{\alpha}} - \mathbf{A_D}\boldsymbol{\chi}^{\boldsymbol{\alpha}}|\dot{\boldsymbol{\gamma}}^{\boldsymbol{\alpha}}| \tag{5.7}$$

For the α (HCP) phase, 24 slip systems: 3 $(0001)\langle 11\bar{2}0\rangle$ basal, 3 $\{10\bar{1}0\}\langle 11\bar{2}0\rangle$ prismatic, 6 $\{10\bar{1}1\}\langle 11\bar{2}0\rangle$ 1st order pyramidal and 12 $\{10\bar{1}1\}\langle 11\bar{2}3\rangle$ 2nd order pyramidal have been incorporated. And for the β (BCC) phase, the 12 $\{110\}\langle 111\rangle$ and the 12 $\{112\}\langle 111\rangle$ slip systems are incorporated.

The methodology to create a realistic finite element mesh, representative of the actual material in consideration and including both the α and β phases of the material follows the procedure described by Kapoor et al. [89]. For the benefit of the reader, the process is discussed

here in brief and in detail in the additional data section (Section 5.7). The process starts with material characterization involving carrying out EBSD and BSE imaging on the same region of interest, on the surface of the sample. Carrying out BSE in addition to EBSD aids is identifying the exact morphology and location of the β phase, which is essential as the α and β phases are modeled explicitly. Moreover, the entire grain morphology of the β phase cannot be obtained solely from EBSD, due to the sparse information of the β phase (due to its relatively low confidence index), necessitating the need for BSE imaging. Combining information from EBSD and BSE imaging, the spatial location and the crystallographic orientation of the α and β grains can be obtained. Due to the sparse data for the β phase from the available EBSD characterization, the orientation of a single β grain is obtained by averaging all the EBSD data points within that grain, which is also explained in additional data section (Section 5.7).

5.2 High Energy X-ray experiments to determine lattice strain

The HEXD experiment was conducted at the Advanced Photon source (APS) at the Argonne National Lab, beamline 1-ID-E. The general experimental setup used in this experiment is shown in Fig. 5.1. High energy monochromatic X-rays at 71.676 keV ($\lambda = 0.017298$ nm) were deemed suitable for this material to conduct the required High energy X-Ray Diffraction. The detector used was a single amorphous silicon flat panel GE detector with 2048 x 2048 pixels and a 200 μm pixel pitch. Tensile specimens were loaded under uniaxial tension in the load frame, and were held to prescribed strain values under displacement control in order to take a HEXD scan. A 500 μm tall region in the middle of the gauge section was scanned in increments of 100 μm each, using a 100 μm tall box beam.

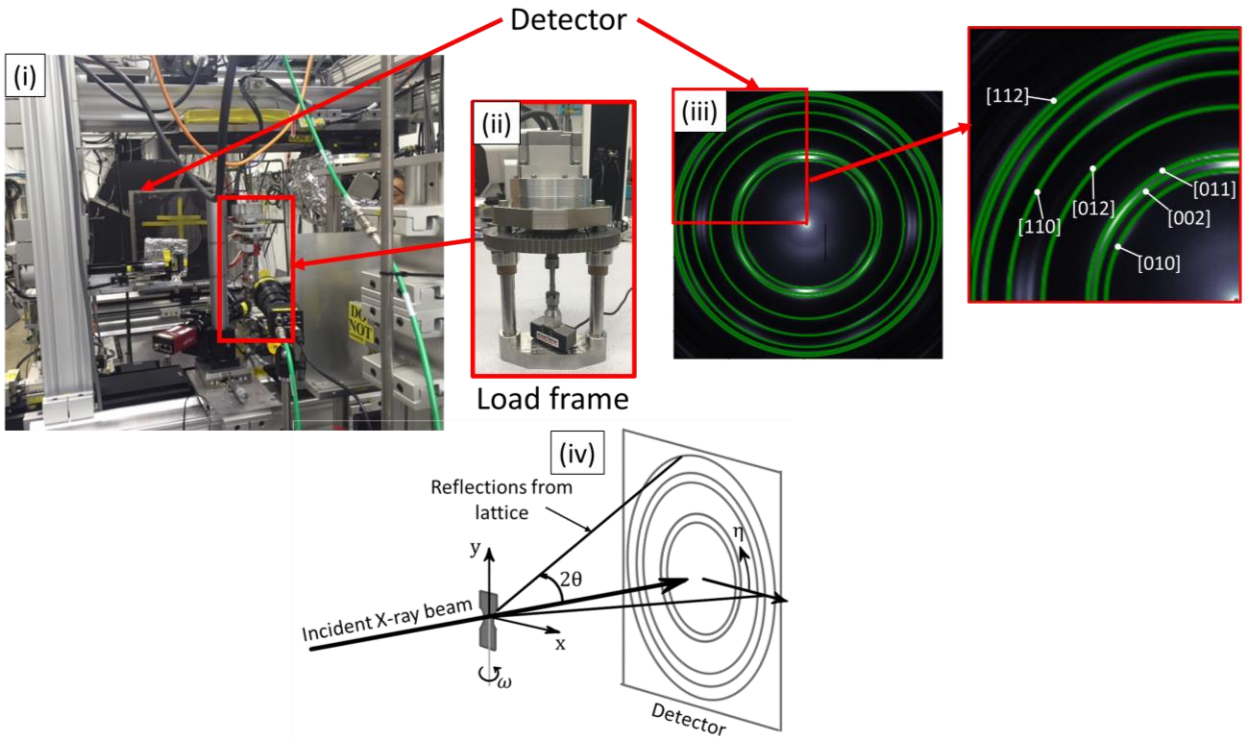

Figure 5.1. HEXD experiment: (i) Experimental setup at APS, showing the detector and the load frame; (ii) zoomed in view of the load frame; (iii) observed diffraction rings on the detector, with a zoomed view showing the (hkl) planes corresponding to the rings; (iv) schematic of the HEXD experiment, showing the geometry of the specimen and the associated nomenclature, with y being the loading axis, ω the rotation about the y axis, η the azimuthal angle, θ the Bragg angle, and correspondingly 2θ being the radial distance of the diffraction ring on the detector.

The experimental setup, including detector tilts, an accurate sample to detector distance, and the beam center was calibrated using reference Ceria (CeO_2) powder patterns with the help of the software fit2d. Ceria images were taken 180° apart from each other in ω, and the results were averaged out to rule out any vertical shifts of the loading axis. The diffraction patterns of the specimens comprised of complete Debye-Scherrer rings, which made them good candidates for wide-angle X-ray scattering (WAXS) or powder diffraction analysis. Scans were taken every 5° while the specimen was rotated about its loading axes (in ω) spanning an angular range of 130°. At a distance of roughly 1280 mm away from the detector, 11 α rings corresponding to the {010}, {002}, {011}, {012}, {110}, {013}, {020}, {112}, {021}, {004}, {022} planes, and 4 β rings corresponding to the {110}, {020}, {121}, {220} planes were successfully captured on the GE detector.

When a monochromatic X-ray beam is focused onto the region of interest in the sample, the crystals that satisfy Bragg's condition diffract the incident x-rays to form Debye-Scherrer rings that are captured on the area detector. The detector records the intensities of these rings at each frame (i.e. each recorded ω angle). An image summed over all ω angles was used in this experiment in order to eliminate any texture effects while performing the powder diffraction analysis. This was followed by performing an integration of the ring intensities over the azimuth η and plotting against the radial direction 2θ.

The position of these intensity peaks at radial distance 2θ along with the beam wavelength λ gives the inter-planar spacing of {hkl} family of crystallographic planes. This relationship is governed by Bragg's law.

$$\mathbf{2d_{hkl}\sin\theta_{hkl}=n\lambda} \tag{5.8}$$

Where d_{hkl} is the inter-planar spacing and θ_{hkl} is the Bragg angle of {hkl} planes in all the crystals illuminated by the beam.

Henceforth, any shifts in these peak positions from the initial or reference state gives an indication of an averaged value of elastic strain $\epsilon^{hkl}_{elastic}$ that can be measured for {hkl} family of planes using Eqn. 9.

$$\boldsymbol{\epsilon^{hkl}_{elastic}} = \frac{\mathbf{d^{hkl} - d^{hkl}_o}}{\mathbf{d^{hkl}_o}} \tag{5.9}$$

Where d^{hkl} is the inter-planar spacing at a particular load step, and d^{hkl}_o is the inter-planar spacing at the initial state for a given {hkl}. The data reduction was done using a MATLAB code (provided by Jonathan Almer) using the approach described in [55,135,136]. Upon loading the specimen under uniaxial tension in the loading direction (LD), the strains along LD and consequently the lattice strains along LD will increase, while the strains along the transverse direction (TD) and subsequently the lattice strains along TD will decrease. In the Debye-Scherrer rings, these values are obtained from azimuthal angles η=90° and 270° for the former, and 0° and 180° for the latter, respectively. At the initial state, when the specimen is unstrained, the diffraction rings form circles on the area detector. Since d^{hkl} and 2θ are inversely related, an increase in d^{hkl} implies a contraction along the corresponding 2θ position. Therefore, as the sample is strained

further, these circles become elliptical - contracting along the y-axis and expanding along the x-axis of the detector plane. The MATLAB routine takes intensity lineouts along 2θ at the desired azimuthal angle η=90° and 270° to obtain axial strains, and 0° and 180° to obtain transverse strains. These 1-dimensional line profiles give the variation of intensity with respect to increasing radial distance 2θ. Each of these peaks is individually fit using a pseudo-Voigt function in order to obtain the desired inter-planar spacing value d^{hkl}. Finally, the lattice strain $\epsilon^{hkl}_{elastic}$ is obtained using Eqn. 5.9.

5.3 Fitting the crystal plasticity parameters

In addition to having a well-developed, physically relevant CPFE model and a physically realistic microstructural mesh, representative of the material in consideration, to get reliable results from CPFE simulations, it is imperative that the parameters used in the CPFE model are determined correctly. The objective of this part of the research is to establish a set of CPFE parameters for the individual α and β phases of Ti-6Al-4V for the model presented in Section 5.1. The parameters used in the current model can be sub-divided primarily into three groups based on the methodology used to obtain their values: (i) parameters that can be determined based on the physical understanding of the material, and hence can be directly taken from available literature; (ii) parameters on which constraints can be applied based on the on physical understanding, available in literature; (iii) parameters for which reasonable bounds or constraints cannot be applied. The classification of each of the parameter used in the model are highlighted in Table 1, which contains a list of all the fit parameters.

The first step of the fitting routine involves fixing the CPFE parameters and their bounds, based on their physical understanding from literature. The elastic constants for the α phase are taken from the work of Bridier et al. [47], the ratio of strain rate sensitivities between the basal and prismatic slip systems is taken from Chatterjee et al. [2], the bounds for the elastic constants of the β phase are taken from Bernier et al. [116] and Ozturk et al. [61], and the bounds on the critical resolved shear stress values for the different slip systems are based on [45,60,83]. This is followed by breaking the fitting process into two parts. Firstly, the CPFE parameters are determined by fitting the simulated stress-strain curves to macroscopic stress-strain curves for three different pedigrees of Ti-6Al-4V, each with a different β volume fraction, using a multi-objective genetic

algorithm framework, discussed in detail in Section 5.1. This procedure ensures that the macroscopic response of the material is consistent with the experimentally observed response. However, it does not ensure that the individual parameters of the α and β phases are uniquely determined, hence these CPFE parameters, more importantly for the lower volume fraction β phase need to be further optimized. This is achieved by simulating a virtual x-ray diffraction experiment and comparing the simulated lattice strain obtained on different crystallographic planes for both the α and β phase with experimentally determined lattice strains from HEXD experiments discussed in Section 5.2. This optimization routine is discussed in detail in Section 5.3.2.

5.3.1 Fitting to macroscopic stress-strain curves

To determine the correct set of parameters for the CPFE model, it is essential that only one set of these parameters exist for a given material, i.e. they are unique. To ensure this, the parameters selected should be such that even if another simulation corresponding to a different microstructure and a different β volume fraction is run using the same parameters, the CPFE model should be capable of giving the desired stress-strain response without re-fitting or changing any of the parameters. This is achieved by posing this as a multi-objective optimization problem: optimizing the CPFE parameters to simultaneously fit three different pedigrees of Ti-6Al-4V, which vary in their β volume fraction. The individual objective function for this fitting routine is the root mean squared error between the simulated and experimental stress-strain curves for each of the pedigrees. The three microstructures used for this fitting procedure and the schematic of the objective function are shown in Fig. 5.2. This fitting routine is implemented using genetic algorithm based optimization, implemented in Matlab and linked with Abaqus to run on a high performance-computing platform, using Python, based on the work of Prithivirajan et al. [50] and Bandyopadhyay et al. [137].

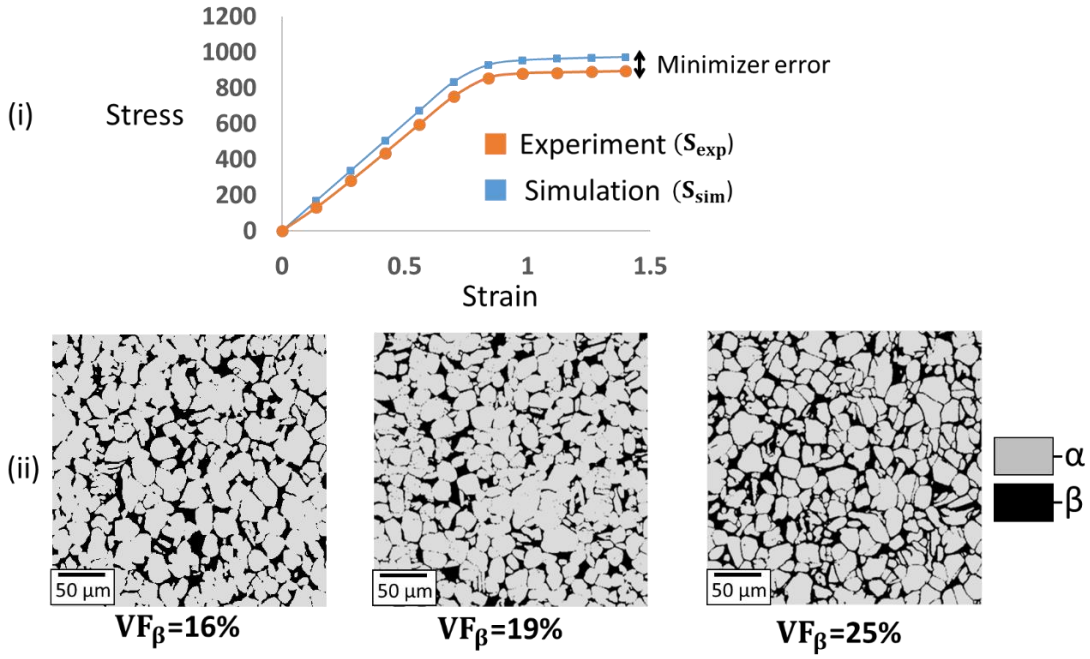

Figure 5.2. Fitting multiple material pedigrees, with varying β volume fractions using a multi-objective genetic algorithm: (i) visual representation of the objective function to minimize the error between simulated and experimental stress-strain curves. (ii) The three different material pedigrees used for fitting, along with their β volume fractions.

5.3.2 Fitting to lattice strain data

The β volume fraction of the material pedigrees used for fitting in Section 5.3.1 varies from 16% to 25%. With this relatively low volume fraction of the β phase, compared to the α phase, the macroscopic fit, discussed in Section 5.3.1, will have a tendency to be dominated by the α parameters. Additionally, the macroscopic fit does not ensure a unique local behavioral response of the material. To ensure that the parameters for the individual α and β phases are fit correctly, another method using lower scale experimental data, where the β phase data can be separated from that of the α phase is needed. This is achieved using data from the HEXD experiments discussed in Section 5.2.

The result of the HEXD experiments is lattice strain on certain families of crystallographic planes, mentioned in Section 5.2, for both the α and β phases of the material, for the different pedigrees (varying β volume fraction) of material that are tested. To use lattice strains on specific crystallographic planes as an objective function for optimizing the CPFE parameters, the same data needs to be extracted from the simulations. This is achieved by running a virtual experiment

using the developed CPFE model, based on the work of Dawson et al. [138]. The procedure involves identifying grains within the microstructure being simulated that will satisfy the diffraction condition for a given family of crystallographic planes, given a diffraction vector and then using these grains to compute the lattice strain for the given set of crystallographic planes. This procedure involves examining each grain in the microstructure to see if the scattering vector and the plane normal align within an angle of resolution, which is taken to be 5^{o}. This results in a set of grains for each plane normal being investigated. To compute the lattice strains the elastic strains parallel to the scattering vector are computed and averaged over the grains in the set for each plane normal. This optimization routine along with the schematic of the grains within the sample is shown graphically in Fig. 5.3.

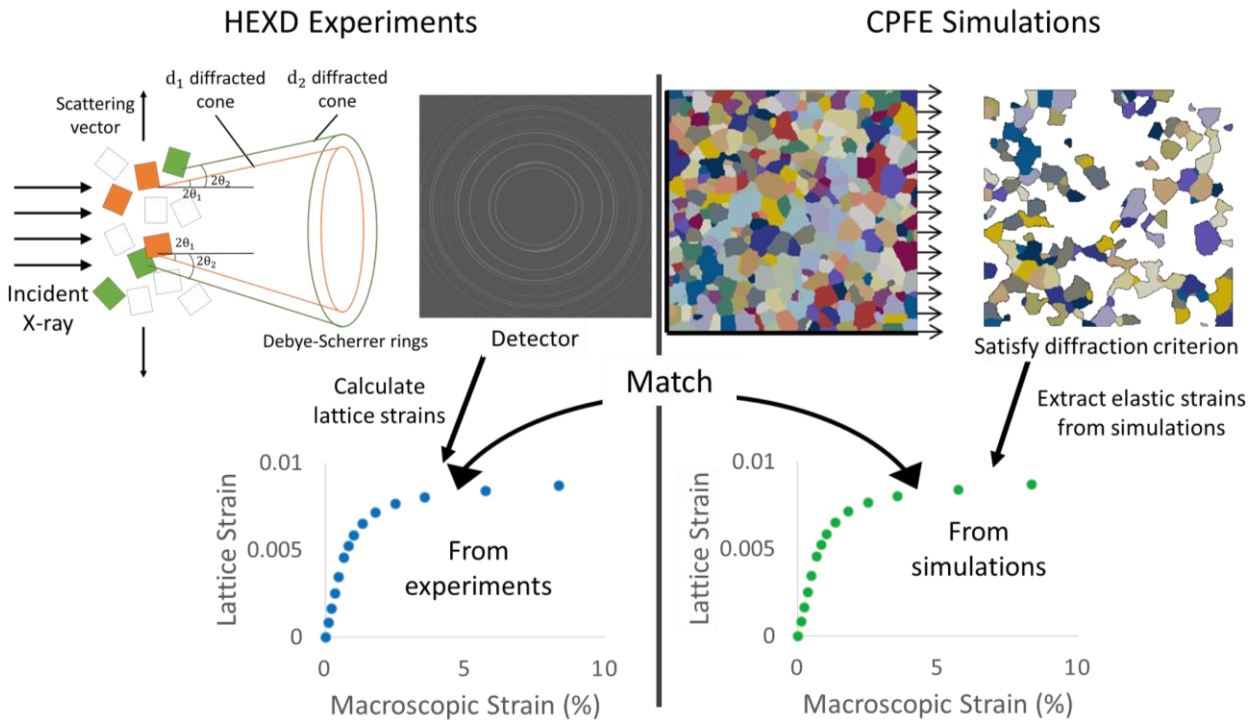

Figure 5.3. Fitting lattice strain data: Comparing HEXD experiments with CPFE simulations by setting up virtual diffraction with a schematic of the HEXD experiment shown on the left and the virtual diffraction shown on the right.

It must be noted that the HEXD experiments are carried out on relatively large sample (order of millimeters), compared to the simulation volume (order of microns). This results in the number of grains in the experiment being on the order of thousands, as opposed to hundreds in the simulation volume. To ensure that statistically, enough grains that satisfy the diffraction condition

are obtained from the simulation volume, a larger statistically equivalent microstructure is created from the statistics obtained from the characterized region, as shown in Fig. 5.4. This is done using DREAM.3D [123] by ensuring the grain size distribution, the volume fraction as well as the crystallographic orientation of both the phases of the statistically equivalent microstructure match the experimentally characterized material. The final calibrated CPFE parameters used for this study are shown in Table 5.1.

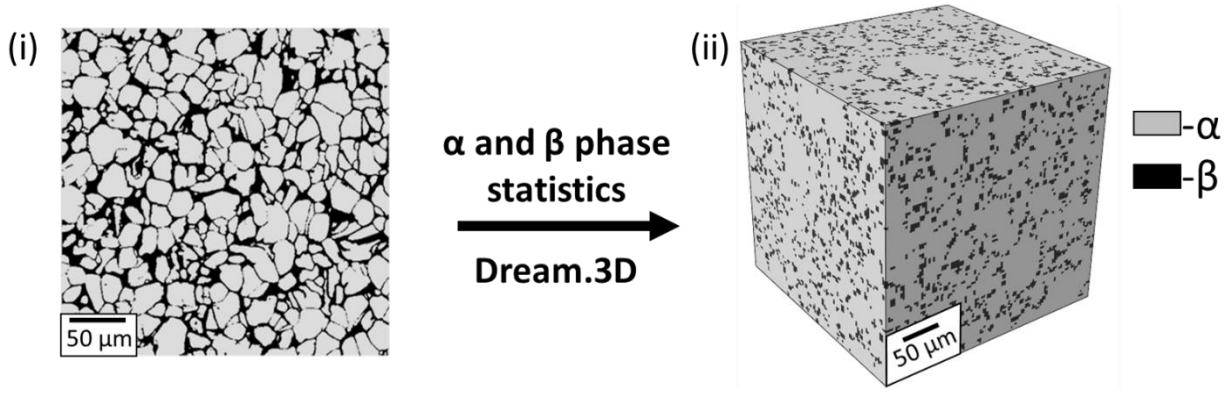

Figure 5.4. Generating synthetic microstructures to fit lattice strains to HEXD experiments, to ensure statistical enough number of grains are included: (i) Microstructure from characterization with ~300 grains, (ii) statistically equivalent virtual microstructure with ~5000 grains.

Table 5.1. Crystal plasticity parameters for the individual α and β phases along with classification on how the parameters are fit

Parameter	**Value**				
	α (HCP)			**β (BCC)**	
	Fitting procedure	**Value**		**Fitting procedure**	**Value**
$\dot{\gamma}_0$	Fit	0.01		Fit	0.01
m	Literature	**Basal**	50	Literature	15
		Prism	25		
		Pyramidal-1	15		
		Pyramidal-2	15		
CRSS (MPa)	Fit with bounds from literature	**Basal**	400.09	Fit with bounds from literature	370.6
		Prism	352.46		
		Pyramidal-1	466.78		
		Pyramidal-2	562.04		
D **(MPa)**	Fit	**Basal**	141.36	Fit	98.2
		Prism	92.15		
		Pyramidal-1	256.40		
		Pyramidal-2	308.70		
d_{avg} **(μm)**	Characterization	13.50		Characterization	1.22
K_y **(MPa*$\sqrt{\mu m}$)**	Fit	**Basal**	97.13	Fit	122.4
		Prism	102.00		
		Pyramidal-1	79.22		
		Pyramidal-2	89.78		
K_s **(MPa)**	Fit	**Basal**	97.13	Fit	150.0
		Prism	130.0		
		Pyramidal-1	156.14		
		Pyramidal-2	111.80		
λ	Fit	15		Fit	15
C_{11} **(MPa)**	Literature	169000		Fit with bounds from literature	128250
C_{12} **(MPa)**		89000			113000
C_{44} **(MPa)**		43000			60390
C_{13} **(MPa)**		62000			--
C_{33} **(MPa)**		196000			--

5.4 Investigating the role of the orientation relationship between the α and β phases on time dependent cyclic loading: an application of the developed model

The fully calibrated model presented in the previous sections is used to gain a better understanding of the changes in the deformation behavior with the variation in the orientation of the α and β phases. To understand the possible differences in the material response, stemming from the orientation relationships existing between the α and β phases, two microstructures are investigated: an equiaxed microstructure that does not follow the BOR (similar to the one used for fitting in Section 5.3) and a bimodal microstructure that follows the BOR. Since characterization data for the bi-modal microstructure is not available, to compare the two microstructures, a bi-modal microstructure is created by synthetically inserting lamellar β in the α EBSD obtained for the equiaxed microstructure. This ensures that the β volume fraction and the crystallographic orientations of the alpha phase are consistent in the two microstructures. The synthetic microstructure creation involves inserting β laths with random geometric orientations that have their crystallographic orientation such that they align with the α phase, following one of the variants of the BOR. This is done by modifying the FE mesh of the microstructure using in-house Matlab scripts.

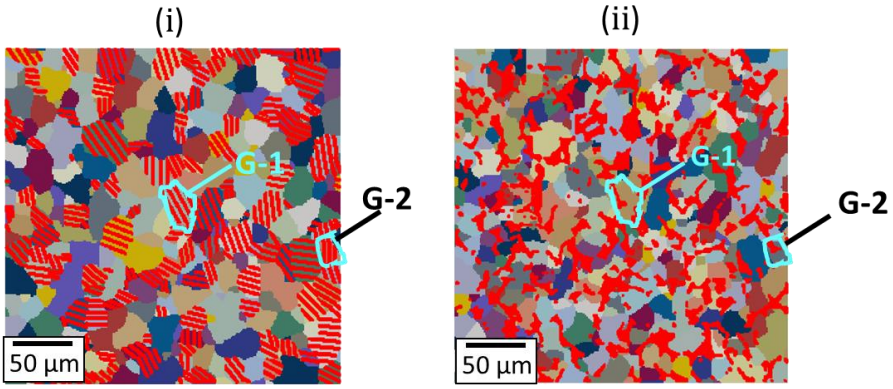

Figure 5.5. Microstructures used to study time dependent and cyclic deformation in a (i) bi-modal microstructure that follows BOR, (ii) equiaxed microstructure that does not follow BOR. The α phase is colored according to grain ID and the β phase is shown in red to highlight the difference in the distribution of the β phase between the 2 microstructures. Two grains, G-1 and G-2 are highlighted and their intra-granular deformation behavior will be discussed in the upcoming sections.

After creating the bi-modal microstructure, the two microstructures need to be compared based on a specified loading condition. They are subject to two different loading conditions, shown

in Fig. 5.6, comprising of cyclic loading, with hold times i.e. dwell loading, as well as cyclic loading without hold times. The results discussed in the next section correspond to an applied load of 800 MPa. Simulations were carried out at lower stresses (550 MPa) as well, however, due to similar conclusions being drawn from them, they are presented in the additional data section (Section 5.7). Additionally, to see the benefits, if any, that the explicitly modeled α and β phases have over simulations that neglect the β phase, the results of the two microstructures are compared with a fully α microstructure. Finally, the effect of varying the β volume fraction in the equiaxed microstructures is studied on time dependent cyclic loading. For the purposes of the upcoming sections, the bi-modal microstructures that follow the BOR and the equiaxed microstructure that does not follow the BOR will be referred to as BOR and non-BOR microstructures, respectively.

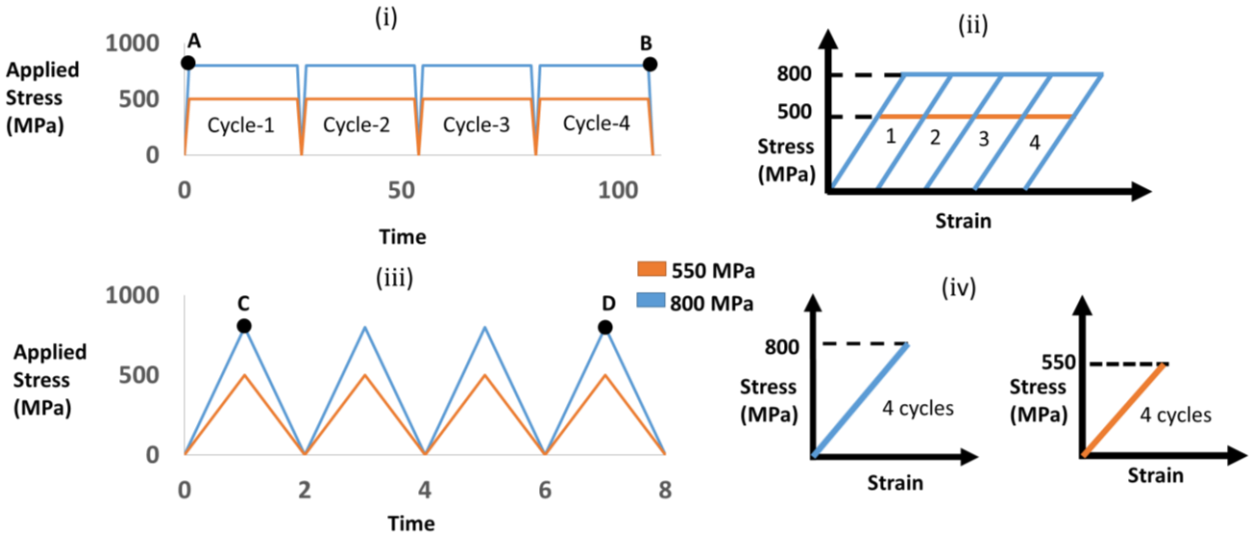

Figure 5.6. Applied load to the simulation volume with stress-time plot for (i) cyclic loading with time hold (i.e. dwell) and (iii) cyclic loading with no time holds. Stress-strain plot for (ii) cyclic loading with time hold (i.e. dwell) and (iv) cyclic loading with no time holds. Both loading conditions are shown for two applied loads (550 and 800 MPa)

5.5 Results

Since the purpose of these simulations is to understand the variation in the deformation within the microstructure, quantities to highlight the local distribution of stresses as well as plasticity within the microstructure are needed. The quantity used to observe the variation in stresses within the microstructure is the stress in the loading direction (σ_{xx}), as it is the dominant stress value due to the microstructures being loaded uniaxially along the x-axis. The quantifiable

metric to measure the amount of accumulated plasticity is taken to be the total plastic strain accumulation (PSA), defined in Eq. 10 and 11. The stress in the loading direction and the PSA are depicted over the entire microstructure as well as their distributions are studied in individual grains highlighted in Fig. 5.6.

$$\dot{p} = \sqrt{\frac{2}{3} L_P : L_P} \tag{5.10}$$

$$p = \int \dot{p}\, dt \tag{5.11}$$

Where, L_P is the plastic velocity gradient, defined in Section 5.1. After subjecting the different microstructures to the loading specified in Fig. 5.6, firstly the differences in modeling the α and β phases explicitly versus completely neglecting the β phase are studied. These are done by plotting σ_{xx} and PSA within a grain (G-2), close to the boundary of the microstructure to minimize any neighboring effects that might alter the stress distributions while comparing the three cases. The plots for variation in the quantities, along a tie line, drawn along the loading direction are shown in Fig. 5.7. For both the figures, the variation of these quantities with time are also plot.

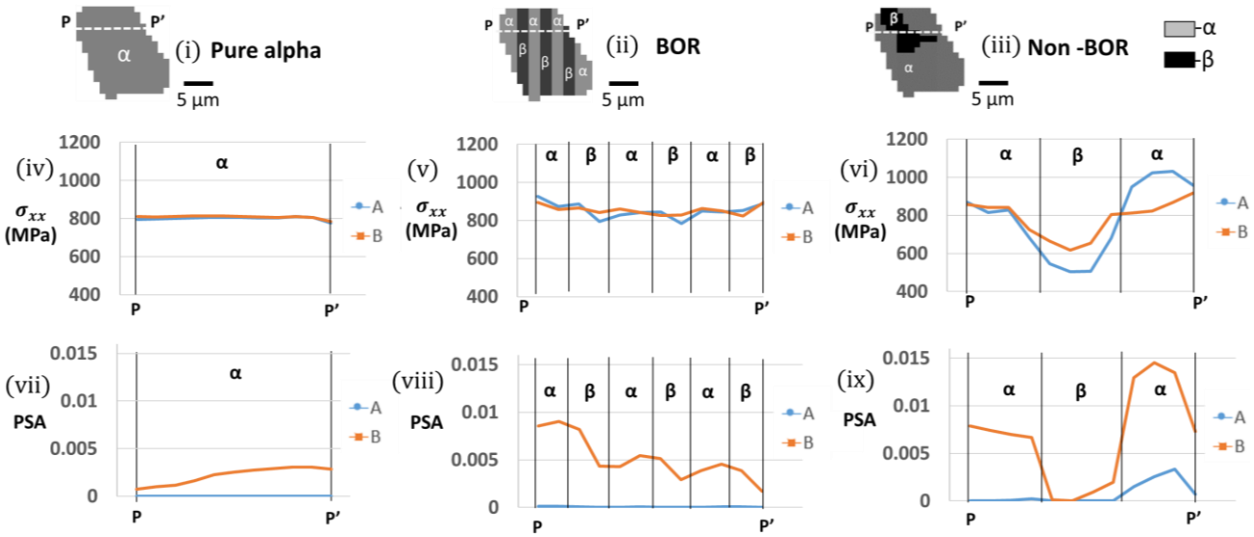

Figure 5.7. Differences in the simulations with and without incorporating the β phase at the grain scale for a grain (G-2) using a tie line P-P' to see the distribution within the grain for a: (i) fully α microstructure; (ii) BOR microstructure; (iii) non-BOR microstructure. Distribution of σ_{xx} at time A and B, for the three cases: (iv) fully α microstructure; (v) BOR microstructure; (vi) non-BOR microstructure. Distribution of PSA at time A and B, for the three cases: (vii) fully α microstructure; (viii) BOR microstructure; (ix) non-BOR microstructure.

Next, the effect of applying cyclic loading with time holds, i.e. dwell loading, corresponding to the load shown in Fig. 5.6 (i) is analyzed by plotting the distribution of σ_{xx} and PSA on the entire microstructure and is shown in Fig. 5.8. This is followed by selecting a grain within the microstructure (G-1), to get information about the distribution of these two quantities within a single grain in the bulk of the microstructure. The variation in these quantities, within a single grain, along a tie line, are shown in Fig. 5.9. For all the plots, the variation of the plot quantities with time is also shown (quantities are plot at time A and B).

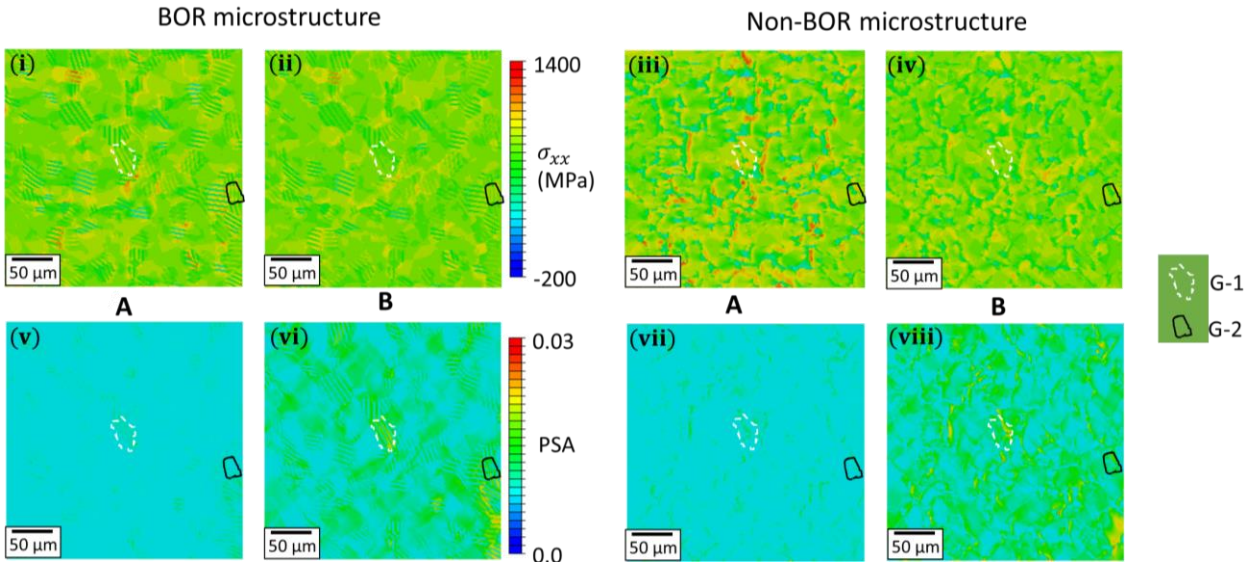

Figure 5.8. For applied dwell loading (800 MPa applied stress), shown in Fig. 5.6(i), σ_{xx} in the BOR microstructure at (i) time A. and (ii) time B; σ_{xx} in non-BOR microstructures at (iii) time A. and (iv) time B; PSA in BOR microstructure at (v) time A. and (vi) time B; PSA in non-BOR microstructure at (vii) time A. and (viii) time B

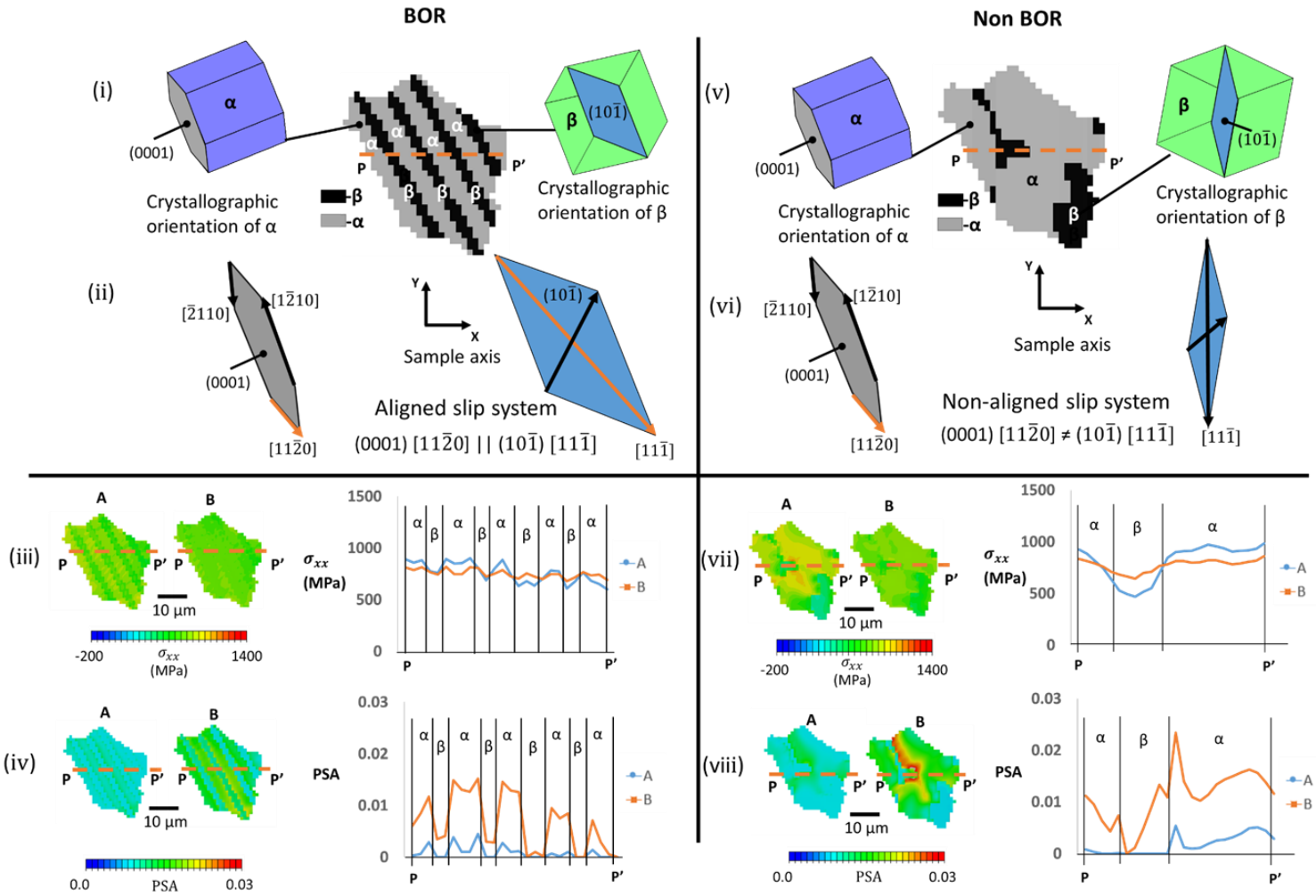

Figure 5.9. Visualization of the crystallographic orientation of the α and β phases and the alignment of the slip systems between the two phases for grain G-1 for the BOR microstructure: (i) and (ii) and non-BOR microstructure: (v) and (vi), respectively. σ_{xx} and PSA distribution in grain G-1 across a tie-line, P-P' in the grain for the BOR microstructure: (iii) and (iv) and non-BOR microstructure: (vii) & (viii), respectively.

Next, σ_{xx} and PSA are depicted for the microstructures subject to cyclic loading (with an applied stress of 800 MPa), without any hold times (corresponding to applied loading shown in Fig. 5.6 (iii)), and are shown in Fig. 5.10. Since there is no time dependent variation in the plot quantities (observation from Fig. 5.10), the variation of the localized quantities within an individual grain is not plot, as it would correspond to the same distribution as in Fig. 5.9 at initial time A.

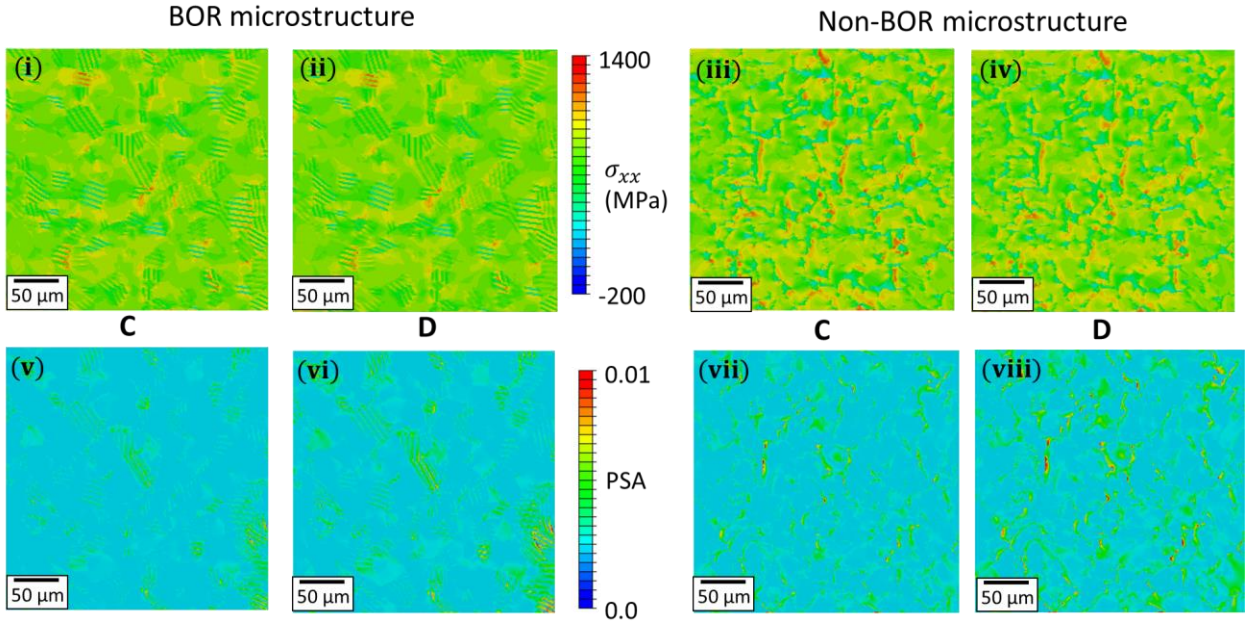

Figure 5.10. For cyclic loading with applied stress of 800 MPa, with no hold times shown in Fig. 5.6(ii), σ_{xx} in the BOR microstructure at (i) time C. and (ii) time D; σ_{xx} in non-BOR microstructure at (iii) time C, and (iv) time D; PSA in the BOR microstructure at (v) time C, and (vi) time D; PSA in the non-BOR at (vii) time C. and (viii) time D.

Finally, to study the effect of the β volume fraction on dwell loading, σ_{xx} and PSA and their variation within the microstructure with time is shown in Fig. 5.11. Additionally, the two equiaxed-microstructures used in this study with varying β volume fraction and their simulated macroscopic stress-strain are shown in Fig. 5.11.

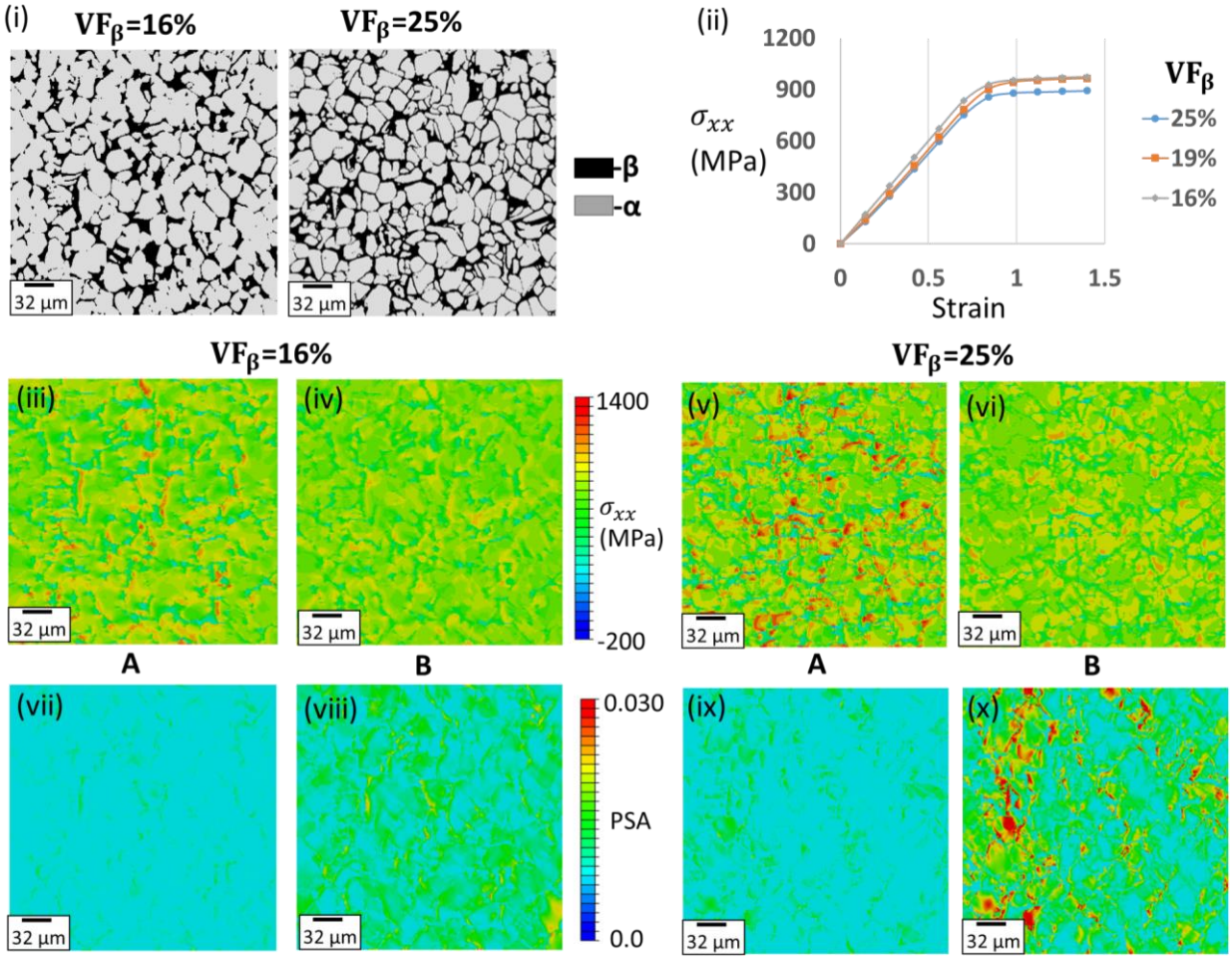

Figure 5.11. (i) Microstructures for studying the effect of β volume fraction; (ii) Stress-strain curves for Ti-6Al-4V with varying β volume fraction; σ_{xx} in microstructure with low β volume fraction at (iii) time A, and (iv) at time B; σ_{xx} in microstructure with high β volume fraction at (v) time A, and (vi) at time B; PSA in microstructure with low β volume fraction at (iii) time A, and (iv) at time B; PSA in microstructure with high β volume fraction at (v) time A, and (vi) at time B

5.6 Discussions

In the fitting framework presented in Section 5.3, macroscopic stress-strain curves coupled with information for the individual lattice strains of the two phases, obtained from HEXD experiments, for different material pedigrees are used to obtain the CPFE parameters for the material. These parameters are valid for microstructures with varying β volume fractions and give the desired material response at the macroscopic as well as the crystallographic (lattice strain) level. These parameters cannot be obtained by fitting only to experiments at one length-scale or using a

single microstructure for fitting. This is because fitting a large number of parameters to a single macroscopic stress-strain curve results in multiple (non-unique) solutions, coupled with the fact that due to the low volume fraction of the β, the macroscopic fit will have a tendency to be dominated by the α parameters. The parameters obtained in this study are valid for α-β Ti-6Al-4V with varying β volume fractions, which cannot be said for the parameters in other CPFE models discussed in Chapter 2. However, it should be noted that the current CPFE formulation has the reference stress dependent on the average grain size, which is obtained from the microstructure characterization. Though the current CPFE parameters will be valid for materials with similar grain size, if a material with a different grain size needs to be simulated, the parameters may need some adjustments.

Traditionally, many CPFE models for dual phase Titanium alloys neglect the β phase due to its relatively low volume fraction, to reduce the complexity of the model and save on computational time. With researchers starting to model the α and β phases explicitly, as discussed in Chapter 1, it is important to understand the benefit of the explicit modeling of the two phases. Figure 5.7 compares the deformation of a single grain, close to the boundary of the simulation volume (to neglect any neighbor effects of grains) in a microstructure that neglects the β phase (fully α) with the BOR and non-BOR microstructures. From the distribution of σ_{xx} and PSA, within the grain, it is seen that the α-β microstructures (BOR and non-BOR microstructures) have higher heterogeneity within a single grain, compared to the fully α simulations, as seen from the local variations across the α-β interface. Thus, neglecting the β phase in the simulations results in under-predicting the localized heterogeneity in deformation, which is exacerbated in the non-BOR microstructure. These observations suggest the growing need to model α and β phases of the alloy explicitly, in order to capture the localized heterogeneities in deformation. This becomes even more important when the CPFE models are used within life prediction frameworks.

From the distribution of σ_{xx} and PSA in the microstructures, and within an individual grain (Fig. 5.9) and their variation with time, it is seen that the non-BOR microstructure shows higher anisotropy in σ_{xx} and PSA, concentrated at the α-β interface for both dwell loading (Fig. 5.8) and cyclic loads with no hold time (Fig. 5.10). Additionally, for cyclic loading, involving hold times (dwell), there is significant redistribution of stresses in the non-BOR microstructure, compared to the BOR microstructure, which is coupled with increased plasticity in the β phase. The mechanism for the redistribution of stresses in the microstructure where the α-β interfaces are misaligned can

be explained based on the stress distribution in the α and β phases and their equilibration with time. For the non-BOR microstructure, due to the mismatch in the crystallographic orientation of the α and β phases, the anisotropy in stresses will be high at the α-β interface, with the α phase having a higher stress than the β phase. However, with time, this stress will redistribute across both the phases, causing a more homogenized distribution of stress, stemming from an increase in the stress in the β phase and a decrease in the α phase. The increased stress in the β phase also explains the increased plasticity with time. This explanation is based on the results of a full field CPFE model, taking into account the stress equilibration with time. A similar conclusion on increased plasticity (in terms of dislocation motion) in the β phase, with time has been proposed by Suri et al. [97], however it is explained on the basis of dislocation mechanics, which are at a lower length-scale and confirmed by TEM imaging. This explanation of redistribution of stresses and it's corresponding explanation at the dislocation level, proposed by Suri et al. [97] is summarized using a schematic in Fig. 5.12. Since the study of Suri et al. [97] involved comparing the BOR microstructure with another microstructure that deviates by around 11^{o} from the BOR, the results of this study are checked for the case of 11^{o} misorientation, and a similar trend is observed. The results are shown in the additional data section (Section 5.7). In addition, to confirm the findings at a lower operating stress, the simulations were repeated for an applied stress of 550 MPa, resulting in similar findings, also reported in the additional data section (Section 5.7).

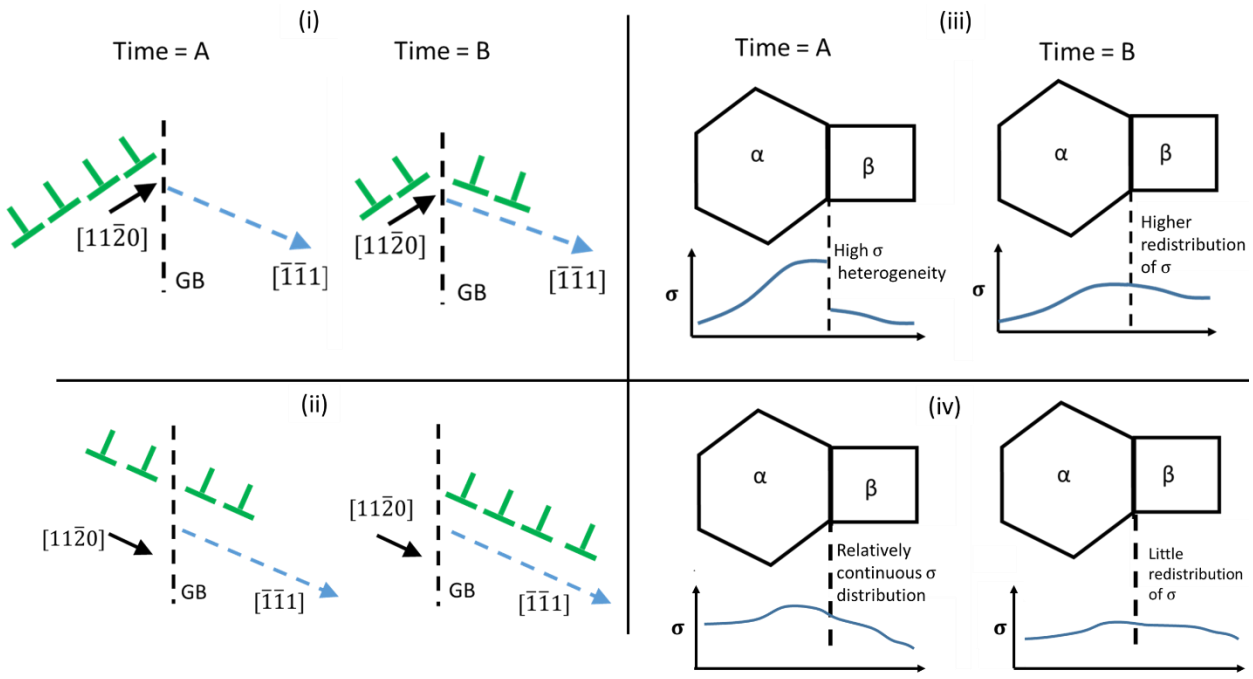

Figure 5.12. Observed stress relaxation explained on the basis of dislocation mechanisms at the sub-grain level for the α-β interface. (i) not following the BOR and (ii) following the BOR. The basis of stress relaxation is depicted from full field CPFE simulations and stress equilibration for the α-β interface (iii) not following the BOR and (iv) following the BOR.

Looking at the σ_{xx} and PSA distribution in the two microstructures subject to cyclic loading, with no time holds (Fig. 5.11), similar trends in the heterogeneity of the two quantities is observed. However, due to no time holds, the stress relaxation with cycles within the microstructure is not significant. The observation of localized high stresses that are not redistributed with cyclic loading suggests that these localized regions of high stresses can act as local strengthening mechanism. This coupled with the fact the slip transmission across the α-β phases is impeded due to the misalignment of the α and β phases in the case of non-BOR microstructure, it can be said that the non-BOR microstructures have the potential to be less susceptible to cyclic loading with no time holds. To confirm the findings at a lower operating stress, the simulations were repeated for an applied stress of 550 MPa, resulting in similar findings. The results are presented in the additional data section (Section 5.7).

Finally, comparing two non-BOR microstructures with varying β volume fractions, from Fig. 5.12, an enhanced tensile response is observed with a lower β volume fraction, which is attributed to the β phase being softer. Additionally, significantly higher heterogeneity in σ_{xx} and

PSA is observed with a higher β volume fraction. In addition to the heterogeneity, quantitatively a higher amount of PSA is observed in the case of the microstructure with a higher β volume fraction, which is attributed to a higher strain needed to reach the same stress in the case of the microstructure with a higher β content, due to its softer stress-strain response. Thus, a combination of higher stress heterogeneity as well as higher and heterogeneous plasticity with time, results in the microstructures with higher β volume fraction have the potential to perform worse during time dependent cyclic loading.

5.7 Additional data

5.7.1 Generating a realistic finite element mesh

Since both the α and the β phases are modeled explicitly in the crystal plasticity model presented in Section 5.1, it is important to clearly separate these two phases in the FE microstructural mesh. The two phases can be easily distinguished spatially using BSE imaging and hence can be separated by thresholding the image. It is observed that the Image Quality (IQ) maps of the α EBSD scans match the BSE images and thus can also be used instead of the BSE images. The thresholding process converts the image into binary bins with the black and white regions being the β and α phases respectively, as shown in Fig. 5.13. This spatial information about the α and β phases is directly utilized to generate the FE microstructural mesh, discussed as follows.

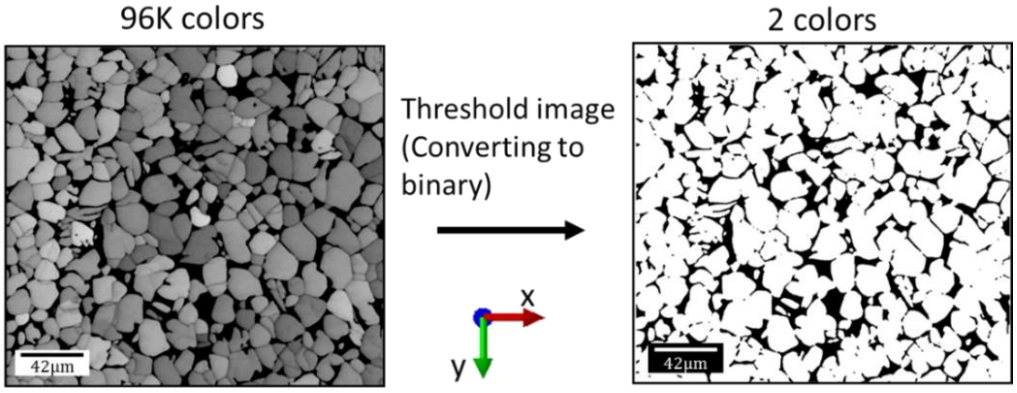

Figure 5.13. Thresholding the IQ image (similar to a BSE image) of Ti-6Al-4V to obtain spatial distribution of the α (light) and the β (dark) phase: (a) before applying the threshold (b) after applying the threshold

The methodology of developing a FE mesh from EBSD and BSE characterization is summarized in Fig. 5.14. The EBSD file is imported into DREAM.3D, an open source data analysis tool, specifically geared towards 3D materials [123]. Using the available α-phase EBSD data, DREAM.3D is utilized to generate a single phase (α) FE mesh composed of hexahedron (hex) elements. The generated mesh is then superimposed with the binary BSE image which is used to identify whether a given element belongs to the α or the β phase utilizing scripts develop in Matlab. After the spatial assignment of the finite elements to the two phases, the crystallographic orientation of the β phase is then assigned based on the β phase orientation data available from EBSD. Since there is some missing crystallographic and spatial information from the EBSD scan, the BSE image is used to determine the spatial location image of the β phase. The entire grain morphology of the β phase is difficult to obtain using EBSD. The process of obtaining the β orientation from sparse EBSD is shown in Fig. 5.15.

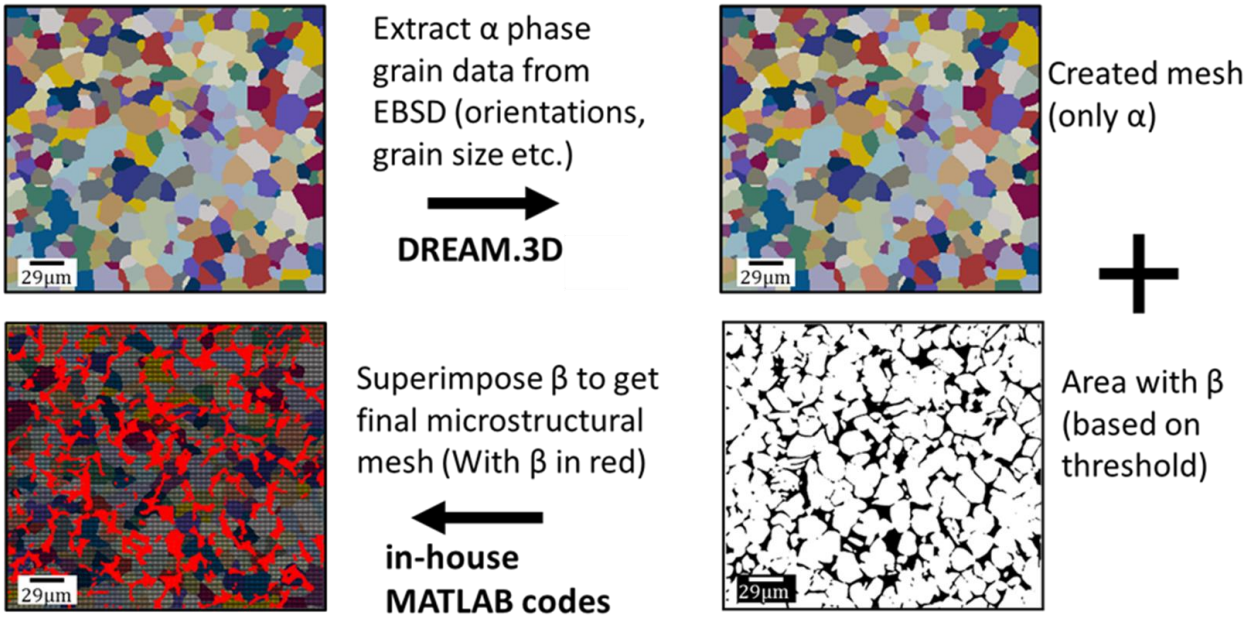

Figure 5.14. Procedure utilized to create FE mesh from material characterization data

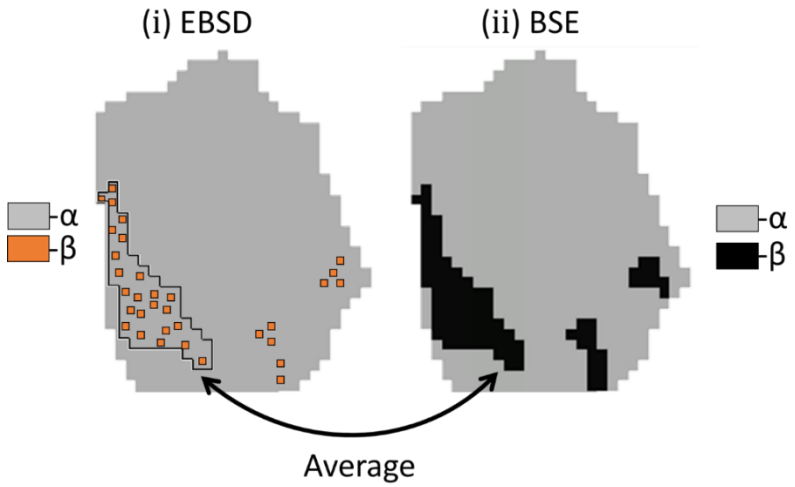

Figure 5.15. Obtaining crystallographic data from sparse β EBSD data by averaging over the entire β grain morphology: (i) α-β EBSD showing the sparse β phase data (ii) BSE imaging showing the morphology of the α and β phases

5.7.2 Simulation results at 550 MPa for dwell loading

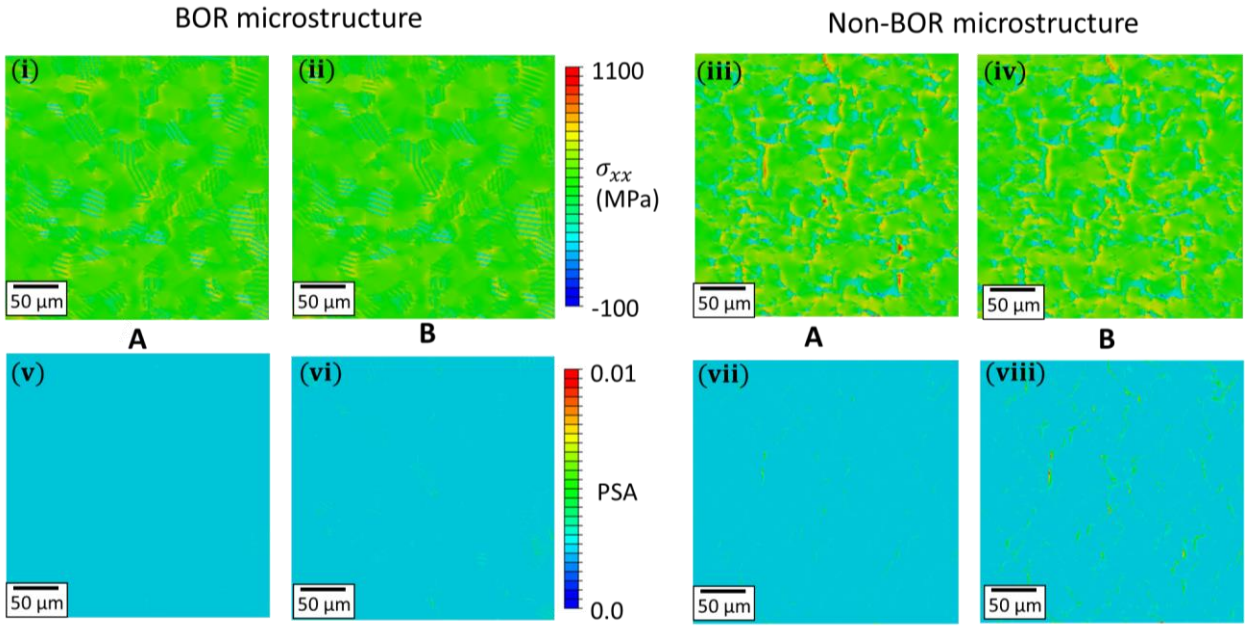

Figure 5.16. σ_{xx} in the BOR microstructure at (i) time A, and (ii) time B; σ_{xx} in non-BOR microstructure at (iii) time A. and (iv) at time B; PSA in BOR microstructure at (v) time A. and (vi) at time B; PSA in non-BOR microstructure at (vii) time A. and (viii) at time B, for samples subject to dwell loading, as shown in Fig. 5.6(i), with an applied stress of 550 MPa.

5.7.3 Simulation results at 550 MPa for cyclic loading with no hold times

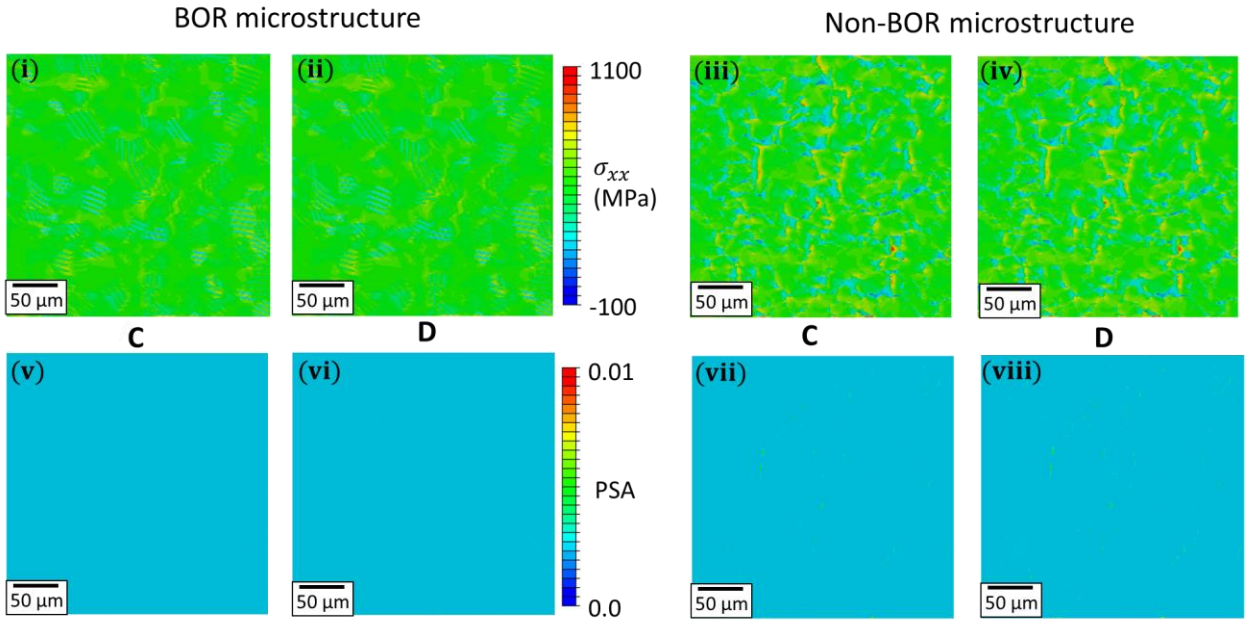

Figure 5.17. For cyclic loading with applied stress of 550 MPa, with no hold times shown in Fig. 5.6(ii), σ_{xx} in the BOR microstructure at (i) time C. and (ii) time D; σ_{xx} in non-BOR microstructure at (iii) time C, and (iv) time D; PSA in the BOR microstructure at (v) time C, and (vi) time D; PSA in the non-BOR at (vii) time C. and (viii) time D.

5.7.4 Results for a microstructure deviating in BOR by 11.5°

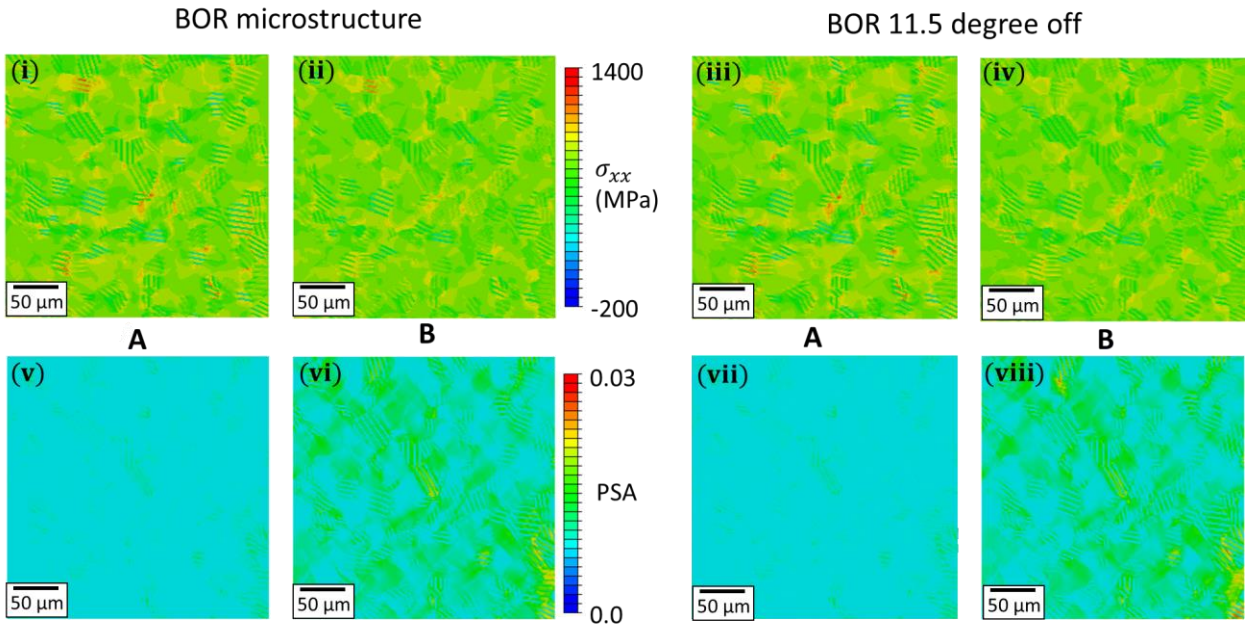

Figure 5.18. For applied dwell loading (800 MPa applied stress), shown in Fig. 5.6(i), σ_{xx} in the BOR microstructure at (i) time A. and (ii) time B; σ_{xx} in 11.5° off BOR microstructures at (iii) time A. and (iv) time B; PSA in BOR microstructure at (v) time A. and (vi) time B; PSA in 11.5° off BOR microstructure at (vii) time A. and (viii) time B.

CHAPTER 6. MODELING STRAIN LOCALIZATION IN MICROTEXTURED REGIONS IN A TITANIUM ALLOY: TI-6AL-4V

In this work, a CPFE based modeling approach is used to model microstructures containing macrozones in a Titanium alloy, Ti-6Al-4V. This is followed by developing a computationally efficient reduced order modeling strategy for these microstructures with macrozones. This is achieved by modeling the large macrozones using crystal plasticity and the remaining microstructure using anisotropic elasticity coupled with J2 plasticity. Further, a unique way to determine the plasticity parameters for the reduced order model, by relating texture to the plasticity parameters, is developed. The reduced order model is then used to understand the effect of the misorientation tolerance used for identification of the macrozones on the deformation characteristics of the microstructure, specifically plastic strain localization within the macrozones. Additionally the strain localization within the microstructure and its link to the orientations of the macrozones is also investigated.

6.1 Material and EBSD characterization

A number of experimental studies that deal with characterization of macrozones have been discussed in Chapter 2 [76,80,82–85], which go over the process of identifying macrozones using experimental data. In addition, Venkatesh et al. [139] present a detailed discussion to identify MTRs using a misorientation tolerance for the c-axis. With the primary focus of this paper being modeling macrozones, the experimental characterization is discussed in brief. The sample containing macrozones is characterized using EBSD (provided by Pratt & Whitney) to determine the grain sizes, grain morphologies, and crystallographic orientations. It should be noted that only the HCP (α) phase is characterized, due to the length scale in consideration, which prevents the characterization of the BCC (β) phase with a significantly smaller size compared to the α grains and being order of magnitudes smaller than the macrozones. Figure 6.1 shows the inverse pole figure (IPF) map obtained from the EBSD scan with an identified macrozone using a misorientation tolerance of 20^o . The orientations of the EBSD points within the 20^o misorientation tolerance are then averaged and assigned to the identified grain.

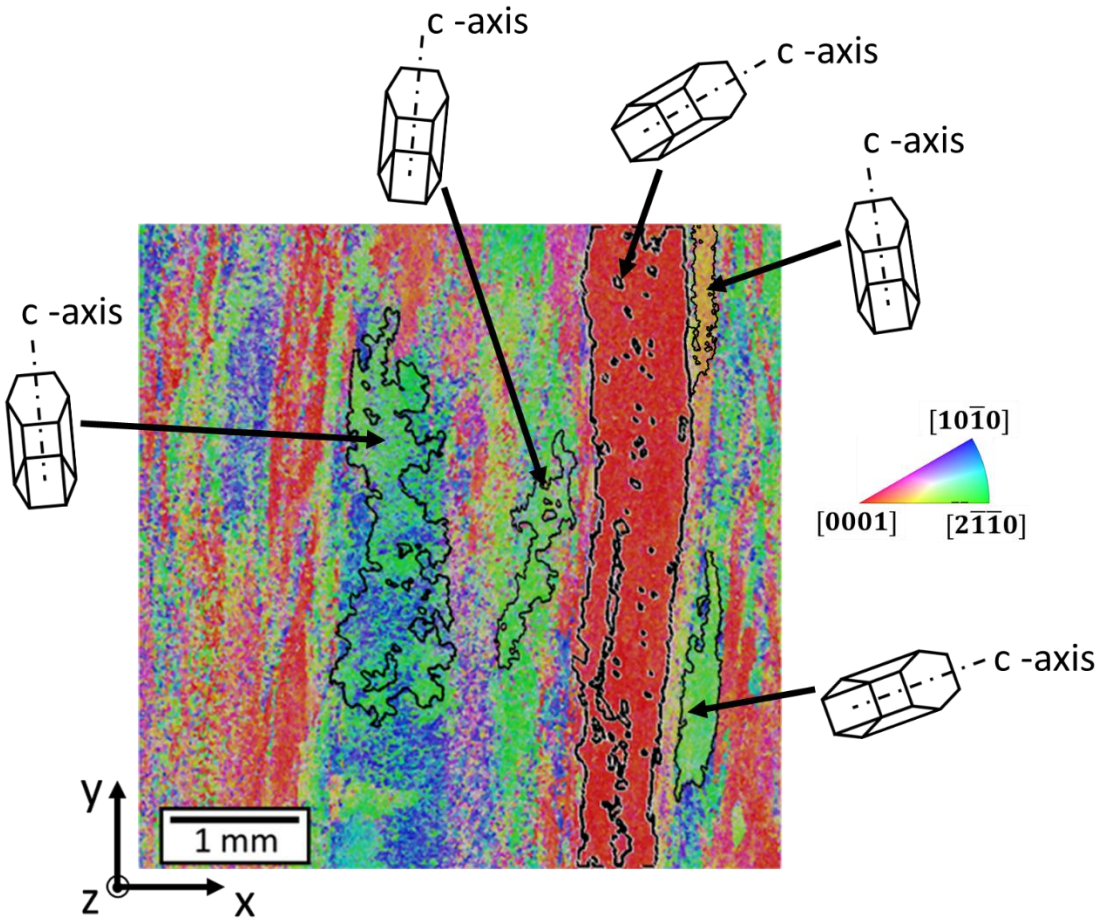

Figure 6.1. Inverse pole figure (IPF) from EBSD on the region probed with a few macrozones highlighted using a 20^{o} misorientation tolerance with the orientation of the c-axis displayed.

6.2 Crystal Plasticity model and FE mesh generation

The CPFE model used in this work is a phenomenological rate dependent model implemented in Abaqus via the user material subroutine. The kinematics are captured by the multiplicative decomposition of the deformation gradient as follows.

$$\mathbf{F} = \mathbf{F^e F^p} \tag{6.1}$$

Where $\mathbf{F}$ is the total deformation gradient and $\mathbf{F^e}$ and $\mathbf{F^p}$ are the elastic and plastic parts, respectively. The plastic velocity gradient in the intermediate configuration is determined using the following equation:

$$\mathbf{L^p} = \dot{\mathbf{F}}^{\mathbf{p}}(\mathbf{F^p})^{-1} = \sum_{\mathbf{i=1}}^{\mathbf{N_{sys}}} \dot{\boldsymbol{\gamma}}^{\mathbf{i}}(\mathbf{s_0^i} \otimes \mathbf{n_0^i}) \tag{6.2}$$

Where s_0^i, n_0^i, and $\dot{\gamma}^i$ are the slip plane direction, slip plane normal, and the shearing rate for the i^{th} slip system, respectively. The flow rule in this model is represented by a power law [20] as follows:

$$\dot{\boldsymbol{\gamma}}^{\mathbf{i}} = \dot{\boldsymbol{\gamma}}_{\mathbf{0}} \left\langle \frac{|\boldsymbol{\tau}^{\mathbf{i}} - \boldsymbol{\chi}^{\mathbf{i}}| - \mathbf{K}^{\mathbf{i}}}{\mathbf{D}^{\mathbf{i}}} \right\rangle^{\mathbf{m}} \mathbf{sgn}\left(\boldsymbol{\tau}^{\mathbf{i}} - \boldsymbol{\chi}^{\mathbf{i}}\right) \tag{6.3}$$

$\langle\ \rangle$ denotes Macaulay brackets with $\langle x \rangle = x$ for $x \leq 0$ and $\langle x \rangle = 0$ for $x > 0$. τ^i, D^i, χ^i, and K^i are the resolved shear stress, slip system resistance, backstress, and the threshold stress for the i^{th} slip system, respectively. $\dot{\gamma}_0$ and m are the reference shearing rate and strain rate sensitivity, respectively, kept constant for all the slip systems. The threshold stress is further broken down into an evolving and a non-evolving component.

$$\mathbf{K}^{\boldsymbol{i}} = \frac{\mathbf{K}_{\mathbf{y}}^{\boldsymbol{i}}}{\sqrt{\mathbf{d}_{\mathbf{avg}}}} + \mathbf{K}_{\mathbf{s}}^{\boldsymbol{i}} \tag{6.4}$$

K_y^i is a non-evolving constant, and d_{avg} is the average grain size, which is similar in formation to the Hall-Petch relation [114,115]. K_s^i evolves according to the following equation.

$$\dot{\mathbf{K}}_{\mathbf{s}}^{\boldsymbol{\iota}} = -\boldsymbol{\lambda}\mathbf{K}_{\mathbf{s}}^{\mathbf{i}}\left|\dot{\boldsymbol{\gamma}}^{\boldsymbol{i}}\right| \tag{6.5}$$

The slip system resistance evolves according to the following equation.

$$\dot{\mathbf{D}}^{\mathbf{i}} = \mathbf{H}\sum_{\mathbf{j=1}}^{\mathbf{N}} \mathbf{q}^{\mathbf{ij}}\left|\dot{\boldsymbol{\gamma}}^{\boldsymbol{j}}\right| - \mathbf{H}_{\mathbf{D}}\mathbf{D}^{\mathbf{i}}\sum_{\mathbf{j=1}}^{\mathbf{N}}\left|\dot{\boldsymbol{\gamma}}^{\boldsymbol{j}}\right| \tag{6.6}$$

The backstress evolves according to the following equation:

$$\dot{\boldsymbol{\chi}}^{\boldsymbol{\alpha}} = \mathbf{A}\dot{\boldsymbol{\gamma}}^{\boldsymbol{\alpha}} - \mathbf{A}_{\mathbf{D}}\boldsymbol{\chi}^{\boldsymbol{\alpha}}|\dot{\boldsymbol{\gamma}}^{\boldsymbol{\alpha}}| \tag{6.7}$$

24 slip systems: 3 $(0001)\langle 11\bar{2}0\rangle$ basal, 3 $\{10\bar{1}0\}\langle 11\bar{2}0\rangle$ prismatic, 6 $\{10\bar{1}1\}\langle 11\bar{2}0\rangle$ 1st order pyramidal, and 12 $\{10\bar{1}1\}\langle 11\bar{2}3\rangle$ 2nd order pyramidal have been included in this model. The elastic constants are based on the values used in [46]. All the CPFE parameters that cannot be obtained from literature with a good degree of certainty are fit to experimental stress-strain curves. The fitting procedure involves using a genetic algorithm to fit the CPFE constants used in Equations 6.1 to 6.7 with the objective function being minimizing the error between the experimental and simulated stress-strain curves. The initial values for the parameters are obtained from [46] and [47]. More details about the fitting routine can be found in [52] and the final fitted parameters are given in Table 6.1.

Table 6.1. Crystal plasticity parameters utilized in the simulations.

Parameter	***Value***	
$\dot{\gamma}_0$	0.001	
m	15	
CRSS (MPa)	Basal	420
	Prism	370
	Pyramidal-1	490
	Pyramidal-2	590
D (MPa)	Basal	148
	Prism	98
	Pyramidal-1	218
	Pyramidal-2	318
d_{avg} (μm)	19.8	
K_y ($MPa*\sqrt{\mu m}$)	Basal	522.62
	Prism	538.28
	Pyramidal-1	521.68
	Pyramidal-2	720.76
K_s (MPa)	Basal	147.06
	Prism	144.18
	Pyramidal-1	143.12
	Pyramidal-2	158.23
λ	50	
C_{11} (MPa)	162400	
C_{12} (MPa)	92000	
C_{44} (MPa)	49700	
C_{13} (MPa)	69000	
C_{33} (MPa)	180700	

This crystal plasticity model is used to run simulations for a subsection of the EBSD scan shown in Fig. 6.1. The EBSD scan in Fig. 6.1 is used as an input to DREAM.3D, an open source data analysis tool, specifically geared towards 3D materials [123] to create a finite element (FE) mesh with hexahedron elements. Details about generating the FE mesh using DREAM.3D can be found in [89]. This finite element mesh is then used as an input for the CPFE simulations as well as the reduced order model simulations presented in the following sections. The area of the EBSD map that is simulated along with the FE mesh created and the result of the simulation (strain in the loading direction) are shown in Fig. 6.2. The FE mesh consists of 1391112 hexahedron elements, with an element size of 1µm*1µm*1µm. The simulation takes 72 hours to run using 320 processors.

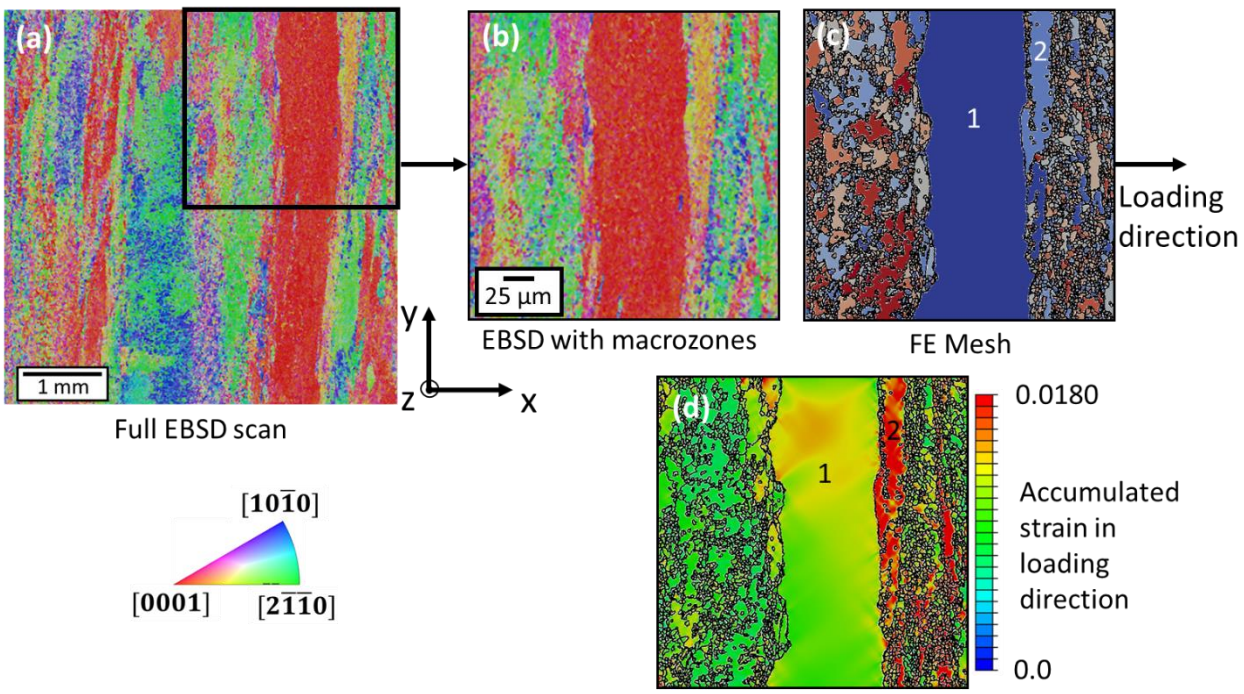

Figure 6.2. (a) Complete IPF map from the EBSD scan, (b) Region of the EBSD map used for the simulations, (c) FE mesh of the region of interest (each grain colored differently for easy identification), generated from the EBSD scan using DREAM.3D with the two largest macrozones highlighted (1 and 2). (d) Total strain in the loading direction corresponding to a macroscopic strain of 1.2%. Note: The FE mesh is not 2D and has a thickness of two elements in the z (in-plane) direction.

6.3 Reduced order model

Running the full scale CPFE simulations on the microstructures, like the one in Fig. 6.1, which are extremely large (on the order of millimeters) takes a long time (72 hours for the current microstructure). Though simulations play an important role in understanding deformation in microstructures with macrozones, these large simulation times diminish their advantage and hence reduces the application of modeling approaches specifically in the industrial sector. To reduce the computational expense, and at the same time to understand the deformation behavior in and around the macrozones, a reduced order model needs to be introduced. In order to capture the anisotropy that exists between grains due to their varying crystallographic orientations, it is essential that the elastic anisotropy is captured by rotating the elastic stiffness tensor according to the orientation of the grain with respect to the sample axis.

In the reduced order plasticity model proposed and used in this work, the simulations for microstructures containing macrozones are run using a combined J2-plasticity and CPFE model. This involves using a full scale CPFE formulation to model the large macrozones present (two in the current work) in the microstructure and using J2-plasticity with full anisotropic elasticity to model the remaining regions as shown in Fig. 6.3. It must be reiterated that the plasticity simulations are not elastically isotropic but do consider the crystallographic orientation of individual grains by rotating the anisotropic elastic constant tensor appropriately using Eq. 11, which can be seen in the variation of stress among different grains in Fig. 6.3.

The implementation of plasticity within Abaqus [140] is based on the elastic-plastic decomposition of the deformation gradient as in Eq. 1 but is simplified using a small strain assumption, which is valid for our simulations to give the additive strain rate decomposition.

$$\dot{\varepsilon} = \dot{\varepsilon}^{\mathbf{pl}} + \dot{\varepsilon}^{\mathbf{el}} \tag{6.8}$$

Which can be written in its integral form over a time increment as follows:

$$\Delta\varepsilon = \Delta\varepsilon^{\mathbf{pl}} + \Delta\varepsilon^{\mathbf{el}} \tag{6.9}$$

The elastic behavior is modeled using Hooke's law.

$$\boldsymbol{\sigma} = \mathbf{C}^{\mathbf{grain}} * \varepsilon^{\mathbf{el}} \tag{6.10}$$

With,

$$\mathbf{C}^{\mathbf{grain}} = \mathbf{D} * \mathbf{C} \tag{6.11}$$

Where $\mathbf{C}^{\mathbf{grain}}$ is the elastic constant tensor for the grain in consideration, $\mathbf{C}$ is the single crystal elastic constant tensor and $\mathbf{D}$ is the rotation matrix constructed using the Euler angles of the grain in consideration. The plasticity model used in this work is a simple elastic-plastic model with the stress beyond the yield strain approximated using a straight line (linear isotropic hardening), as shown in Fig. 6.4, with the yield function, $\boldsymbol{f}$, given by [141]:

$$\boldsymbol{f} = \left(\bar{\boldsymbol{\sigma}} - \boldsymbol{\sigma}_{\mathbf{Y}}\left(\bar{\boldsymbol{e}}^{\mathbf{pl}}\right)\right) = \mathbf{0} \tag{6.12}$$

Where $\bar{\boldsymbol{\sigma}}$ is the equivalent deviatoric stress, $\boldsymbol{\sigma}_{\mathbf{Y}}\left(\bar{\boldsymbol{e}}^{\mathbf{pl}}\right)$ is the yield stress, and $\bar{\boldsymbol{e}}^{\mathbf{pl}}$ is the plastic part of the equivalent deviatoric strain $\bar{\boldsymbol{e}}$ defined as follows.

$$\bar{\mathbf{e}} = \sqrt{\frac{2}{3}\mathbf{e}:\mathbf{e}} \tag{6.13}$$

Where,

$$\mathbf{e} = \mathcal{E} - \mathbf{I} * \frac{1}{3}\mathbf{trace}(\mathcal{E}) \tag{6.14}$$

Where $\mathcal{E}$ is the strain tensor and **I** is the identity tensor.

The equivalent deviatoric stress, $\bar{\boldsymbol{\sigma}}$ is defined as follows.

$$\bar{\boldsymbol{\sigma}} = \sqrt{\frac{3}{2}\boldsymbol{\sigma}_{\boldsymbol{D}}:\boldsymbol{\sigma}_{\boldsymbol{D}}} \tag{6.15}$$

With $\boldsymbol{\sigma}_{\boldsymbol{D}}$ being the deviatoric stress tensor.

$$\boldsymbol{\sigma}_{\boldsymbol{D}} = \boldsymbol{\sigma} - \mathbf{I} * \frac{1}{3}\mathbf{trace}(\boldsymbol{\sigma}) \tag{6.16}$$

Where $\boldsymbol{\sigma}$ and **I** are the stress and identity tensor respectively.

The yield stress, $\boldsymbol{\sigma}_{\boldsymbol{Y}}$ in the yield function given by Eq. 12 can be further broken down as follows [141].

$$\boldsymbol{\sigma}_{\boldsymbol{Y}} = \boldsymbol{\sigma}_{\boldsymbol{Y_0}} + \Omega(\bar{\mathbf{e}}^{\mathbf{pl}}) \tag{6.17}$$

With $\boldsymbol{\sigma}_{\boldsymbol{Y_0}}$ being the yield stress at zero plastic strain ($\bar{\mathbf{e}}^{\mathbf{pl}}$=0) and $\Omega(\bar{\mathbf{e}}^{\mathbf{pl}})$ being the linear isotropic hardening function which can be defined as:

$$\mathbf{d}\Omega(\bar{\mathbf{e}}^{\mathbf{pl}}) = \mathbf{h}\ \mathbf{d}\bar{\mathbf{e}}^{\mathbf{pl}} \tag{6.18}$$

Where **h** is a constant and can be determined based on the data points from the stress-strain curve shown in Fig. 6.4. Equations 6.8 through 6.18 correspond to a continuum plasticity model with linear-isotropic hardening. This model is available within the metal plasticity section of the Abaqus constitutive model database [140].

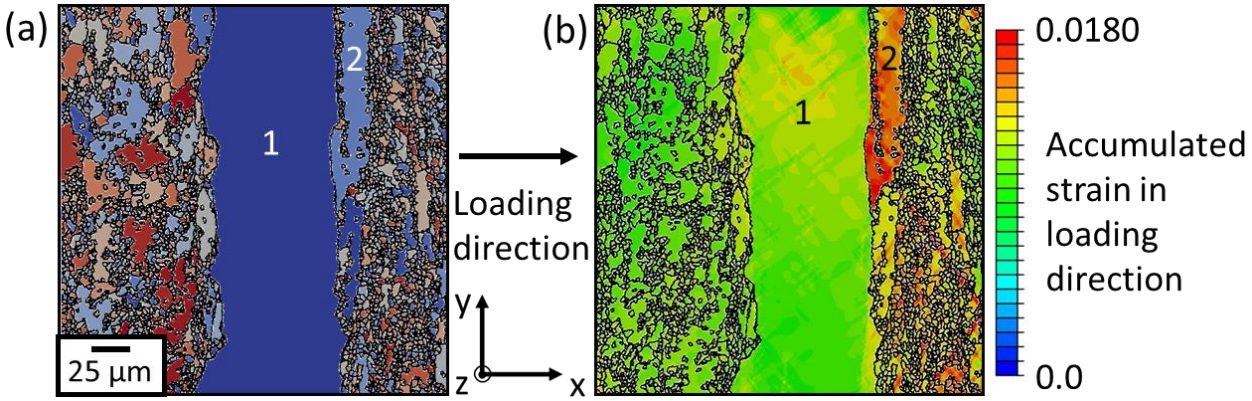

Figure 6.3. (a) FE mesh of the region of interest (each grain colored differently for easy identification). (b) CPFE-J2 plasticity simulations for microstructures with macrozones after 1.2% applied strain: Macrozones 1 and 2 modeled using crystal plasticity and the remaining regions with anisotropic elasticity coupled with J2 plasticity.

The CPFE framework used for the reduced order model is the same as presented in Section 6.2, including the model parameters (Table 6.1). For the anisotropic elasticity, the elastic constants are the same as that of the CPFE model, since the elastic description of the material remains the same (Table 6.1). The additional parameters that are needed to run the elastic-plastic simulations are the stress at yield (σ_Y) and stress corresponding to a strain beyond yield, taken to be at 1.4% in this work ($\sigma_{1.4\%}$). Figure 6.4 shows the approximation of the stress-strain curve used for the J2 plasticity simulations along with its parameters.

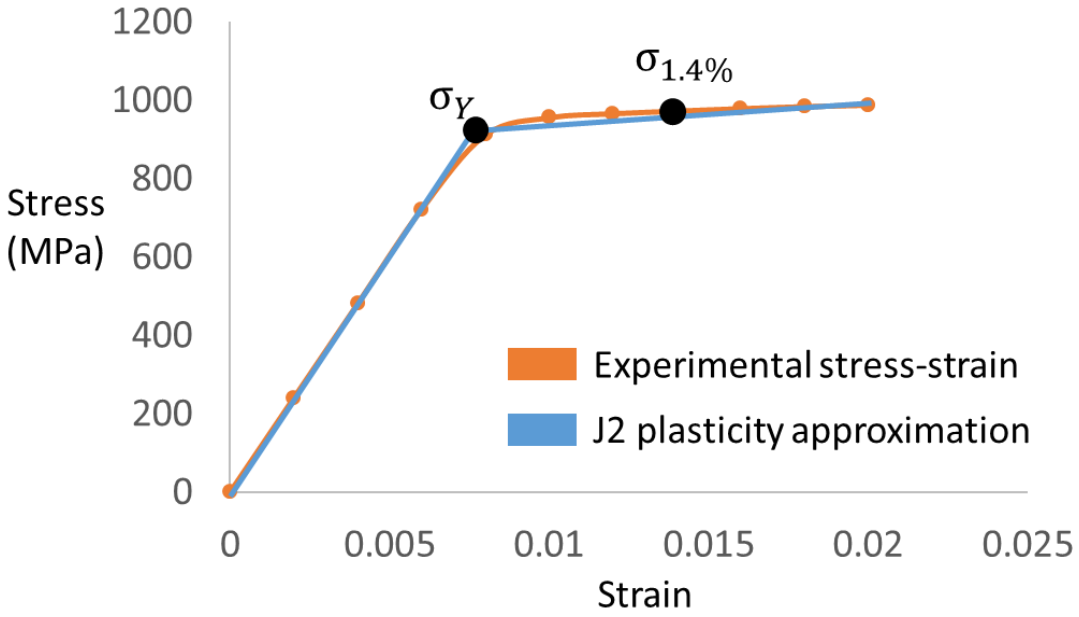

Figure 6.4. Approximation of the stress-strain curve used for determining J2-plasticity parameters with the two J2-plasticity parameters indicated in black.

The plasticity parameters needed for the simulations (σ_Y and $\sigma_{1.4\%}$) can be determined from the stress-strain curves. One method of determining the stress-strain curves (and hence the parameters) is by performing tensile experiments and EBSD characterization on the microtensile samples with varying textures. However, since carrying out experimental tests on all the microstructures is time consuming and may not always be feasible, a method to determine the plasticity parameters without using the experimental stress-strain curves is presented in the next section.

6.4 Determining J2 plasticity parameters

To reduce the overall experimentation (and hence the associated time), a simpler and more feasible approach is utilized to train the reduced order model, in which high fidelity full-scale CPFE modeling is leveraged to determine the parameters for the reduced order J2 plasticity parameters. This is achieved by linking the microstructure, specifically the texture of the material to the stress-strain curve and hence to the J2 plasticity parameters. One such scalar quantity capable of quantifying texture for HCP materials is the Kearns factors [142], which are defined as follows:

$$\mathbf{f_j} = \sum \mathbf{V_j}\,\mathbf{cos^2}(\boldsymbol{\alpha_j}) \tag{6.19}$$

Where the Kearns factor, f_j, is the effective fraction of grains aligned with their [0001] axis, i.e. their c-axis parallel to the reference direction. α_j is the angle between the [0001] direction and the reference direction, V_j is the volume fraction of grains with an angle between the [0001] direction and the reference direction being α_j. To completely define texture in terms of the Kearns factors, three reference directions (mutually perpendicular) are needed, which are taken to be the lab frame in this work. This results in three orientation factors obeying the following relationship: $f_1 + f_2 + f_3 = 1$. Due to this relation between the three Kearns factors, only two out of the three factors are sufficient to describe the texture of a given pedigree of the material.

With the Kearns factors serving as a scalar representation of the texture of the material, the second step involves creating a link between these scalar factors and the plasticity parameters. This is achieved by creating a database relating the Kearns factors to the plasticity parameters. To populate the database, a large number of microstructures with randomly assigned orientations are used to run full scale CPFE simulations. These microstructures are not complete 3D but are '2.5D' i.e. 2D with an extrusion for thickness of 4 elements and consist of 360 grains meshed using 250000 elements, which are sufficiently large to capture the required texture (but are not extremely large) and can be run in a matter of 4 to 5 hours. These microstructures with randomly assigned orientations cover a large number of possible orientations out of the total possible orientations. The stress-strain curves obtained from these simulations can then be used to determine the J2 plasticity parameters and populate the database.

Using this database, given the microstructure of the material, the Kearns factors can be determined and linked to the corresponding J2 plasticity parameters. The process of creating the Kearns database is visually summarized in Fig. 6.5 below.

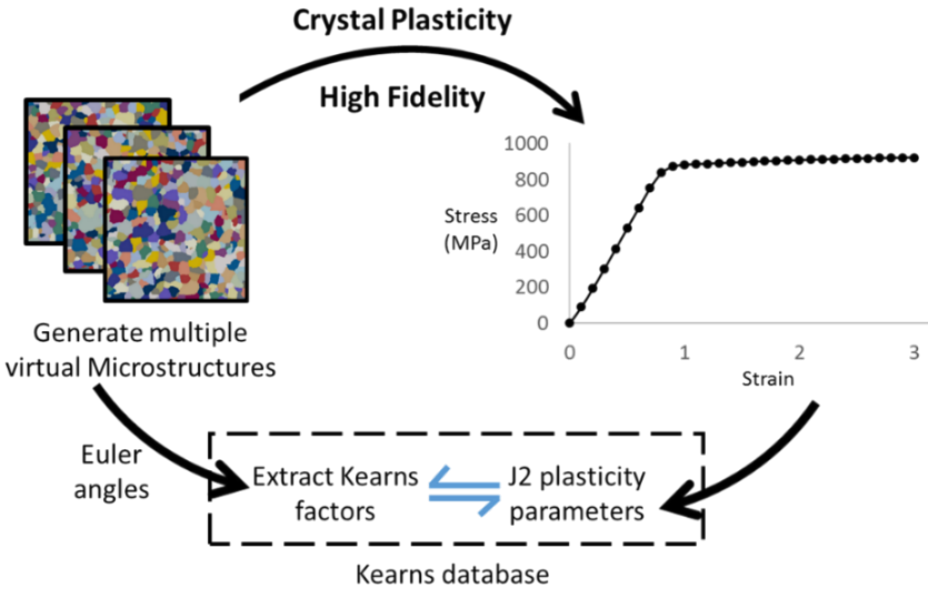

Figure 6.5. Procedure to create a Kearns factor database, which is used to determine the J2 plasticity parameters for a given microstructure.

Since the Kearns factors follow the relation $f_1 + f_2 + f_3 = 1$, based on the chosen axes that are mutually perpendicular to each other, the texture of a given microstructure can be represented as a point on a unit cell of a Cartesian coordinate system with f_1, f_2, and f_3 being the mutually orthogonal axes. If the entire possible orientation space is considered, it will result in a plane with the equation $f_1 + f_2 + f_3 = 1$. To create the current database, nearly 1500 simulations with microstructures having varying orientations are run. The orientations that are simulated to create the database in the current work are plotted in Fig. 6.6. It can be seen that a large portion of the orientation space is covered by the set of simulations conducted in this study. If a microstructure being simulated does not have its Kearns factors close to any of those plotted in Fig. 6.6, the J2-plasticity parameters are determined by interpolating between the available data points using the following equation

$$\textbf{J2 parmeter } (\mathbf{P}) = \frac{\mathbf{W_1P_1 + W_2P_2 + W_3P_3}}{\mathbf{W_1 + W_2 + W_3}} \tag{6.20}$$

Where, W_1, W_2, and W_3 are the distances of the three closest points in the database, with distances being measured using the Kearns factors as the coordinate axis and P_1, P_2, and P_3 representing one of the J2 plasticity parameters of the closest points in the database, respectively. Both the parameters, σ_Y and $\sigma_{1.4\%}$ are treated independently and can be obtained using Eq. 20.

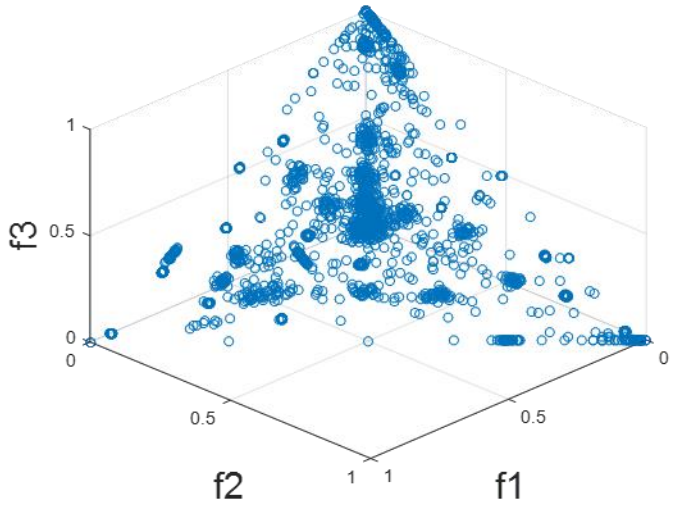

Figure 6.6. Orientations represented using the Kearns factors contained in the database plotted using the Kearns factors as the coordinate axes.

6.5 Validation

The reduced order model, presented in Section 6.3, as well as the procedure developed to determine the plasticity parameters using the Kearns database, presented in Section 6.4, needs to be validated, in order to build confidence with the results obtained from the reduced order model. A simple and reliable way to validate the precision of the reduced order model is to compare the results with those of the full CPFE model. This is done by carrying out two comparisons: One comparison is made at a macroscopic strain of 0.45%, where the microstructure is expected to be dominated by elastic strains to ensure the anisotropic elasticity captures the deformation below the yield point of the material. The other comparison is made at 1.2% macroscopic strain, where the strain distribution is going to be a combination of elastic and plastic strain to validate the complete model. The comparisons are shown in Fig. 6.7 below.

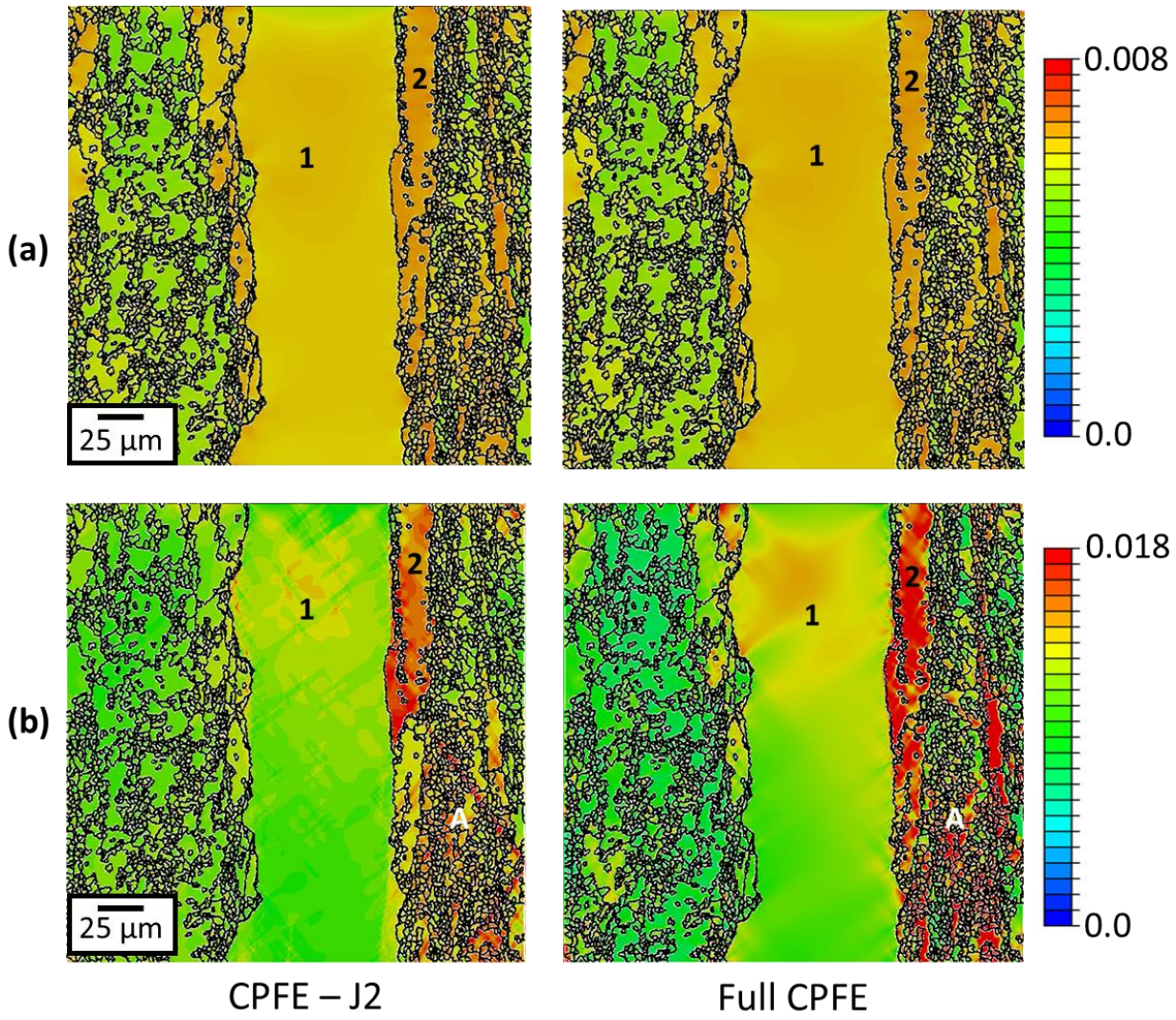

Figure 6.7. Total strain along the axial (loading) direction at (a) 0.45% strain (where the majority of strain is expected to be elastic) and (b) 1.2% (where the plastic strain is significant) with macrozones 1 and 2 identified.

From Fig. 6.7, it is seen that the strain distribution in the loading direction at a macroscopic strain of 0.45% is similar in both the full crystal plasticity and the reduced order model, indicating that the anisotropic elasticity and microplasticity are captured appropriately. At 1.2% macroscopic strain, the strain map comparison, between the reduced order (J2-CPFE) and full (CPFE) models, does not quantitatively relate to each other on a grain-by-grain basis, with the reduced order model slightly under predicting the maximum strain values in macrozones 1 and 2. However, there is a good qualitative match in the regions of high and low strains within the microstructure, as seen in and near macrozones 1 and 2. The ability to capture hot-spots in and around the macrozones are

deemed the most important aspect of these models, which are correctly captured using the reduced order model. In addition, the region of high strain in region labelled as 'A', away from the macrozone is captured in both the models. To further validate the model, the stress component in the loading direction is plotted in Fig. 6.8, and it is seen that the reduced order model slightly under predicts the average stress values, but the stress localization is captured similarly in both the models. This is significant as the reduced order model takes nearly $1/5^{th}$ the time to run on the same microstructural mesh. The reduction in time is important as running large CPFE models with appropriate size scales to capture the macrozones limits their widespread industrial use in damage modeling.

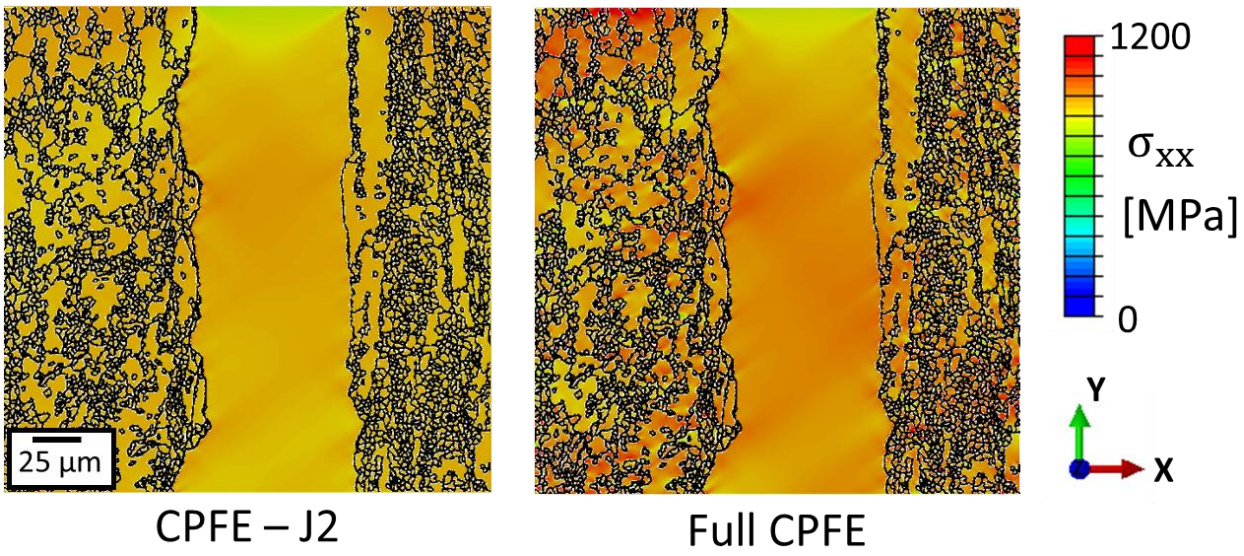

Figure 6.8. Stress distribution in the loading direction at 1.2% strain.

Next to validate the process of determining the J2 plasticity parameters from the Kearns database, the J2 plasticity parameters for a sample with a known experimental stress-strain curve are determined using the Kearns database discussed in Section 6.4. For the microstructure used to validate this process, the J2 plasticity parameters obtained from the experimental stress strain curve are: $\sigma_Y = 912$ MPa and $\sigma_{1.4\%} = 973$ MPa. From the Kearns database method, the parameters obtained are: $\sigma_Y = 906$ MPa and $\sigma_{1.4\%} = 1042$ MPa. The variation in values can be partially attributed to the stress-strain curves being obtained from macro-scale experiments and the simulations corresponding to a smaller volume of the sample.

6.6 Effect of misorientation threshold on the deformation in macrozones

For the simulation discussed in the above sections, the macrozone within the microstructure being simulated is treated as a single grain, which is identified using a 20° misorientation tolerance between grains. The role of the misorientation tolerance used to identify macrozones is investigated in this section. Specifically, the effect of segmenting the macrozone using an 20°, 18°, 15°, 12°, 10°, 8°, and 5° misorientation tolerance, i.e. to analyze the fidelity of the simulation by treating the macrozone as a single homogeneous grain. In each case, the misorientation tolerance within the macrozone is varied, while, the region outside the macrozone is not altered and is still modeled using J2 plasticity with the same microstructure as studied in Section 6.2. To understand the effect of using different misorientation tolerances on the deformation within the macrozone, the plastic strain accumulation within the macrozone is plotted in Fig. 6.9. The plastic strain accumulation, a measure of plastic strain at a given material point, is defined as follows:

$$\dot{p} = \sqrt{\frac{2}{3} L_P : L_P}\ ; p = \int \dot{p}\ dt \tag{6.21}$$

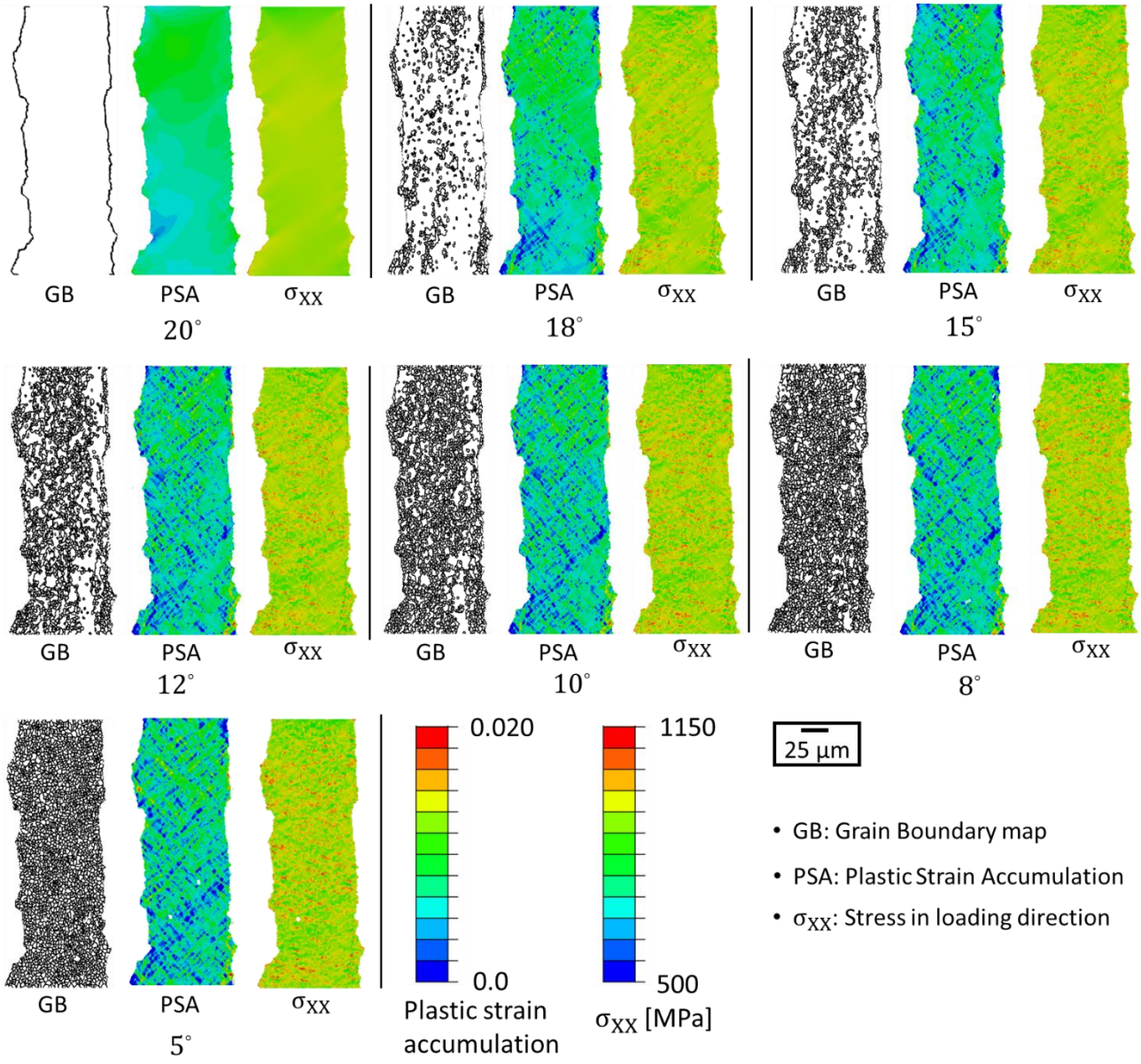

Figure 6.9. Variation in the plastic strain accumulation and the stress component in the loading direction within the largest macrozone with respect to the misorientation tolerance used to identify a macrozone.

From the plastic strain accumulation maps in Fig. 6.9, visually, a difference can be observed between modeling the macrozone as a single grain versus multiple grains; as with increased number of grains, a higher degree of strain heterogeneity is observed within the macrozone. To quantify the strain heterogeneity within the macrozone and how it varies with the misorientation tolerance, a quantifiable measure of strain heterogeneity, which measures the deviation of the strain within a grain from the average strain within the macrozone, is used.

$$\text{Hetrogeneity} = \sum_{k=1}^{N} \frac{(\varepsilon_k - \varepsilon_{mean})^2}{N} \tag{6.22}$$

Where N is the number of grains within the macrozone, and ε_k and ε_{mean} are the strain (in the loading direction) in the k^{th} grain and the averaged strain in the macrozone, respectively. The value of heterogeneity, as it varies with the misorientation tolerance, is shown in Table 6.2 below. In addition, other parameters like the maximum, minimum, and the mean of the plastic strain accumulation within the macrozone is also investigated.

Table 6.2. Measure of strain heterogeneity within the macrozone as a function of the misorientation tolerance.

Misorientation tolerance (no. of grains)	**20^o (1 grain)**	**18^o (812 grains)**	**15^o (1316 grains)**	**12^o (1788 grains)**	**10^o (2381 grains)**	**8^o (2432 grains)**	**5^o (2617 grains)**
Mean strain	0.012	0.012	0.012	0.012	0.012	0.012	0.012
Minimum value (grain averaged)	0.012	0.070	0.070	0.069	0.070	0.069	0.069
Maximum value (grain averaged)	0.012	0.020	0.020	0.019	0.019	0.019	0.019
Heterogeneity	0.0	0.29	0.40	0.47	0.57	0.57	0.59

By analyzing the effect of misorientation tolerance (and hence the number of grains) used to model a macrozone, from Table 6.2, it is seen that the heterogeneity increases with the decreasing misorientation tolerance (i.e. more grains), however the increase from 10° to 5° is not significant as compared from 20° to 10°. There is a marked difference between modeling the macrozone as a single grain, as opposed to dividing it into multiple grains. However, the effect is not pronounced below a threshold of 10°. This suggests that a 10° misorientation tolerance is sufficient to capture the strain heterogeneity within the macrozones. The conventional threshold tolerance used for grains for a CPFE simulation varies from 2 to 5°. Based on the results of this

study, using a threshold of 10° serves the purpose of capturing the strain heterogeneity and using this higher tolerance (as opposed to 2° or 5°) will reduce the simulation time due to the reduction in the number of grains. On the other hand, the conventional tolerance used during characterization to visually identify macrozones is 20°, as discussed in Chapter 2. Thus, using a threshold of 10° (as opposed to the conventional 20°) will result in a conservative estimate of the size of the macrozone and result in visually smaller macrozones. An engineering trade-off exists, between capturing the heterogeneity and gradients in the micromechanical fields within a macrozone, which necessitates a 10° misorientation threshold, and identifying the size of a macrozone associated with the characteristic length-scale of damage, in which a 20° misorientation threshold is more appropriate.

6.7 Investigating strain localization in the microstructure

Since strain localization is known to be a precursor to failure [133,134] and provides a good metric to predict damage, we investigate the strain distribution and localization within the microstructure. The strain distribution, along with the c-axis orientation of the two large macrozones is shown in Fig. 6.10. It can be seen that high strain localization occurs in macrozone 2, which is adjacent to the other large macrozone (macrozone 1). To understand this strain distribution, the orientation of these macrozones is investigated. Macrozone 2 is well aligned for basal and prismatic slip, with its c-axis being nearly perpendicular to the loading direction (referred to as a soft grain). Whereas, macrozone 1, having its c-axis relatively parallel to the loading direction (referred to as a hard grain), is not susceptible to basal and prismatic slip, which have a lower CRSS value compared to other slip systems [1]. This explains why strain localization is observed in macrozone 2 and not in macrozone 1.

In Chapter 2, the reviewed literature suggested that macrozones play a key role in strain localization and crack nucleation. One of the most recently studied crack nucleation mechanism in Ti-alloys relates to the hard-soft grain combination which is also the region of high strain localization in the current microstructure. Multiple studies [143–145] suggest that hard-soft grain combinations lead to strain accumulation in the soft grain coupled with high stress concentration in the hard grain. The stress concentration in the hard grain then results in facet crack nucleation and hence failure. These effects are even more pronounced in hard-soft macrozones than in hard-

soft grains as the entire macrozone (which is orders of magnitude bigger than the individual grains) experiences high stress compared to the adjacent soft macrozone, resulting in higher possibility of facet crack nucleation. The simulation results presented in this paper using both the full-scale CPFE and the reduced order model also result in high strain localization in the soft macrozone of the hard-soft macrozone combination. These results therefore suggest that the reduced order model presented in this work can be incorporated into damage prediction frameworks.

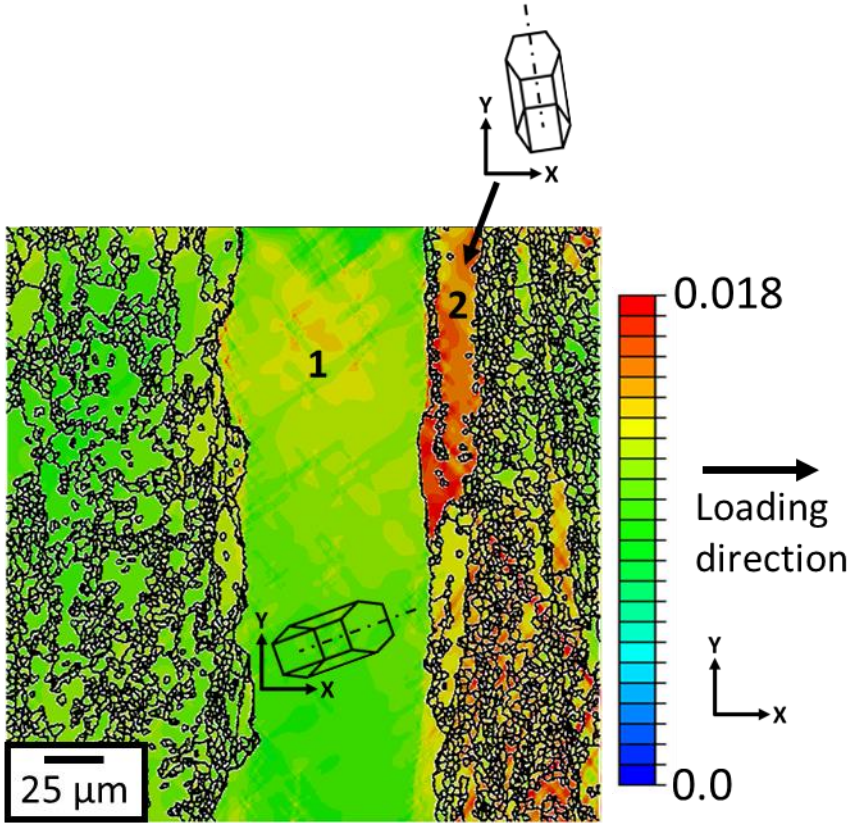

Figure 6.10. Strain distribution in the loading direction at 1.2% macroscopic strain (using the reduced order model).

CHAPTER 7. CONCLUSIONS AND FUTURE WORK

The conclusions of the research presented in this dissertation for each of the chapters is elucidated as follows.

7.1 Chapter 3: Incorporating type 2 residual stresses using HEDM data

In Chapter 3, a new framework is introduced to incorporate type-2 residual stresses in CPFE simulations using a robust approach, which may be extended to other CPFE simulations that utilize the multiplicative decomposition of the deformation gradient, provided the initial residual stresses are known in some form. A one to one comparison between experiments and simulations is made by comparing grain averaged quantities obtained from simulations with HEDM experiments. The results of the simulations with initialized residual stresses and physically realistic BCs show a marked improvement in the correlation with experiments, which serves as a validation for the proposed method. While many CPFE studies have examined the role of the constitutive equations of crystal plasticity (e.g. the flow rule and hardening laws) on predicting mechanical behavior, it is of equal importance to create a physically representative microstructure instantiation that adequately captures the residual stresses present on the crystal. Finally, the simulation results indicate that using the exact physical grain morphology may not offer much benefit over utilizing tessellated grains obtained from grain centroid data for the purposes of understanding grain averaged stress distributions within the simulation volume at the meso-scale. Albeit, capturing the grain morphology is necessary within the simulation to predict intragranular stress concentrations and strain localizations.

7.2 Chapter 4: Incorporating residual stresses via GND densities and validating the CPFE model

In Chapter 4, an experimentally validated CPFE model for additively manufactured Ti-6Al-4V produced via SLM, explicitly accounting for the two phases of the material was developed along with a physically realistic microstructural mesh, and its validation was based on the good

correlation between results from HR-DIC and CPFE simulations. The significant contributions of this chapter are summarized as follows.

- Utilizing grain orientation data from EBSD coupled with the BOR and information about the spatial distribution of the α and β phases in the region of interest using BSE imaging, a physically realistic FE microstructural mesh, representative of the actual material in consideration, is created. In addition, the CPFE formulation itself explicitly accounts for the two phases of the material and utilizes different crystal plasticity parameters for the two.
- Residual stresses are initialized by incorporating initial GND densities, calculated using spatial KAM measurements, obtained directly from experimental material characterization. This is unique compared to other studies since spatial information about GND densities over the region of interest is directly utilized in the model in the form of hardening on different slip systems via the evolution of the backstress. The total backstress is calculated based on the GND density values on slip systems which in turn are composed of the initial GND densities and their evolution during the deformation process. At the beginning of the simulation, due to the initial GND density, which varies for the different families of slip systems, there is variation in slip-system level backstress values among the different families (heterogeneity in the initial backstress values). Interestingly, the backstress evolution stabilizes at around 33 cycles. This stabilization of the backstress may be attributed to the GND densities remaining constant with no more GND densities being produced due to deformation after 33 cycles. Traditionally, the most common backstress model used in CPFE simulations is the Armstrong-Fredrick type, which involves evolution of the backstress based on a source and a sink term, with the evolution purely being driven by the ratio of this source and sink term. This phenomenological relationship often results in saturation of the backstress much earlier than required. The backstress model based on GND densities in this work is more physically realistic and is shown to saturate at a stage that is representative of the experimentally observed mechanical behavior of the material.
- TEM results indicate a higher amount of initial <c+a> dislocations compared to <a> type dislocations near the β grains, which is contrary to what is observed in the same material manufactured using traditional techniques, where <a> type dislocations

outnumber <c+a> dislocations. This is an interesting finding due to the fact that <c+a> dislocations, associated with pyramidal slip are hard to activate due to their high CRSS. This deviation of behavior from traditional materials may be attributed to the manufacturing process itself involving rapid solidification of the melt pool which may result in the formation of non-equilibrium dislocation structures and micro-pores and thus higher <c+a> dislocations. The distribution of initial dislocation density obtained from TEM results affects how the total initial GND density is distributed among the slip systems in the simulations, affecting the initial values of backstress and hence the initial hardening. But it does not seem to play a significant role in the evolution of backstress after its saturation.

- There are similarities in the strain maps and associated regions of strain localization across the prior β grains between the results of the CPFE simulations and HR-DIC. The comparison in this study is unique as it involves a significantly large number of grains (on the order of 1000s), unlike the majority of studies reported in literature. This similarity in strain patterning is attributed to the physically based model as it accounts for both the α and β phases and also accounts for the initial GND densities.
- Strain maps obtained both from simulations and experiments indicate that strain localization predominantly takes place at prior β grain boundaries, suggesting prior β boundaries are capable of blocking slip (since strain localization may be attributed to accumulation of dislocations at these prior β boundaries). This is a significant finding since the β phase is the primary equilibrium structure at elevated temperatures, which exist during the processing route. And thus by changing the process parameters, the β grains may be modified which in-turn would result in the modification of prior β boundaries and the heterogeneous strain distribution response of the material.

7.3 Chapter 5: CPFE model calibrated with multi-scale experiments to understand the effect of the orientation and morphology of the α and β phases on time dependent cyclic loading

In this work, a CPFE model for an industrially relevant dual phase (α-β) Titanium alloy, Ti-6Al-4V is developed, with explicitly modeled α and β phases. The model is calibrated to experiments at multiple length-scales using microstructures with varying β volume fractions. Finally, the model

is used to understand the deformation within Ti-6Al-4V, with varying local orientations and morphology of the α and β phases, focusing on cyclic and time dependent deformation. The significant contributions of this study can be summarized as follows.

- A detailed optimization routine using experimental data from specimen level stress-strain curves and lattice strains on different crystallographic planes for the individual α and β phases, for microstructures with varying β volume fraction is used to determine the CPFE parameters for the individual phases of the material. Using a rich experimental dataset with experiments at multiple length scales, the calibrated CPFE parameters that are valid for Ti-6Al-4V with varying β volume fractions. In addition, the use of actual physically realistic microstructures, obtained from material characterization for fitting the data and gaining an understanding of the material behavior ensures the conclusions drawn from the simulations results are valid for the actual material. However, it should be noted that the current CPFE formulation has a term dependent on the average grain size, which is obtained from the microstructure characterization. Though the current CPFE parameters will be valid for materials with similar grain size, if a material with a different grain size needs to be simulated, the parameters may need some adjustments.

- Using the calibrated CPFE model to compare the deformation behavior in the microstructure with varying orientation relationships between the α and β phases, it is seen that the non-BOR microstructure shows higher anisotropy in stresses and PSA, concentrated at the α-β interface during dwell loading. With time, this is accompanied by significant redistribution of stresses in the microstructure, coupled with increased plasticity in the β phase for the BOR microstructure, compared to the non-BOR microstructure. Based on these observations, the BOR microstructure has the possibility to be less susceptible to time dependent loading, due to lower redistribution of stresses with time.

- Misaligned slip systems (α and β phases not following the BOR) result in a higher stress relaxation with time, which is not significant in the aligned slip systems (α and β phases following the BOR). This observation is explained on the basis of stress equilibration with time, which stems from a high initial stress in the α phase and a lower stress in the β phase, followed by reduction in stress in the α phase and an increase in the β phase with time, which also results in an increased plasticity in the β phase with time. This explanation is

based on the results of a full field CPFE model, taking into account the stress equilibration with time and is similar to conclusions arrived at previously in literature at a lower length-scale, in terms of dislocations mechanics and TEM imaging.

- For simulations with the microstructure subject to cyclic loading with no time holds, higher stress anisotropy is observed the microstructure that does not follow the BOR (compared to the microstructure that does), which is not redistributed with cycles. The observed higher stress heterogeneity leads to the possibility of localized strengthening mechanisms in the non-BOR microstructure, attributed to the crystallographic misalignment of the α and β phases, thereby making non-BOR microstructure more suitable for cyclic loading not involving time holds.
- Simulations investigating the effect of β volume fraction on dwell loading show increasing β volume fraction to be associated with a higher anisotropy in stress and PSA, as well as a higher amount of plasticity (PSA), compared to the microstructure with a lower β volume fraction, for the same applied load. These observations lead to the conclusion that Ti-6Al-4V with higher β volume fraction has the possibility of having a higher susceptibility to dwell.

7.4 Chapter 6: Modeling strain localizations in microtextured regions

In Chapter 6, full scale CPFE modeling is leveraged to develop a reduced ordered model for macrozones in Ti-6Al-4V using a combination of J2-plasticity and CPFE modeling. To make the model versatile and usable for materials with varying textures, a unique way to determine the J2 plasticity parameters from texture information is developed, based on a set of Kearns factors. The results indicate that the reduced order model provides promising results for the strain distribution in the sample, specifically within the macrozone. The reduction in time using the reduced order model (from days to run a simulation to hours to run the same microstructural region) is substantial and hence paves the way for more widespread usage. Using this model, the choice of a misorientation tolerance used to identify a macrozone is investigated, and it is understood that modeling macrozone as a single grain does not capture the local strain heterogeneity, while using a misorientation tolerance of around 10° is sufficient to capture the local heterogeneity. Hard-soft

macrozone combinations, are well known to be potential sites for crack nucleation within these alloys. The results of these simulations also result in high strain localization in the soft macrozone of the hard-soft macrozone combination. This suggests that the simulation methodology, including the reduced order model, can be integrated within damage models for the prediction of failure of Titanium alloys.

7.5 Future work

Based on the research conducted and presented in this dissertation, the following is proposed to enhance the current work.

1. The incorporation of type-2 residual stresses using the triple decomposition of the deformation gradient in the CPFE model was validated with an experimental dataset that was loaded until the yield point of the material. An additional data set, with significant plasticity was available [146] and was attempted to be used to validate the model. However, due to sample being subject to bending loads superposed with tension, the true boundary conditions were difficult to obtain. With the growth in the HEDM experiments, the methodology to incorporate residual stresses can be further verified for datasets that are subject to loading with higher amounts of plasticity and whose boundary conditions can be easily obtained.
2. In the work incorporating residual stresses via GND's, the β phase was modeled using a small number of elements, which in many cases were less than 100 for a single β grain. Using a much finer mesh, coupled with more detailed meshing techniques, a finer mesh for the β phase, as well as the α-β boundary will help reduce any abnormal stress-gradients that may exist at the boundary. Additionally, in this work, hexahedron (hex) meshes have been used to mesh the simulation volumes. Meshing strategies using tetrahedral elements to obtain smoother meshes at the α-β phase boundaries can also be investigated (however, these are prone to volumetric locking). However, this would In also require a new method to determine the gradients within the individual finite elements to calculate the GND density, as the current method is only valid for hexahedron elements.

3. Due to the limitation of the UMAT in Abaqus to store neighbor elemental data, the current method to store neighbor information (which is used to calculate the gradients needed to evaluate the GND density in Chapter 3) is done by writing a file for each element in the mesh. This places a limit on the number of elements that can be used for the model, due to the limitation on the number of files that can be stored on the supercomputer. This limitation can be overcome by exploring other ways to store the neighbor data.
4. In Chapter 5, the variability in localized deformation in the α and β phases is studied using extruded 2D finite element meshes of the surface that is characterized using EBSD and BSE imaging. This study can be further enhanced by using 3D microstructures to model the α and β phases and see the effect on material properties within the bulk of the material, compared to the surface.
5. The reduced order model used to understand deformation in microstructures containing macrozones was validated with only one microstructure, containing a large hard macrozone. Using more microstructures with varying macrozone orientations will result in the model being fully validated for varying microstructures and orientations.
6. The methods of incorporating residual stresses presented in this work can be applied to understand fatigue scatter due to the presence of varying distribution of residual stress based on the manufacturing and processing route used to develop the alloy, specifically for additively manufactured materials. This will help understand relationship between the material processing, residual stresses and fatigue life.
7. Finally, combining all the modeling efforts of this work at the different length scales i.e. incorporating residual stresses, explicitly modeling α-β phases and modeling macrozones would result in a complete modeling tool to model Ti alloys at multiple length-scales, which then can be used within a life prediction frameworks.

REFERENCES

[1] G. Lütjering, J.C. Williams, Titanium, Springer Science & Business Media, 2007.

[2] K. Chatterjee, J.Y.P. Ko, J.T. Weiss, H.T. Philipp, J. Becker, P. Purohit, S.M. Gruner, A.J. Beaudoin, Study of residual stresses in Ti-7Al using theory and experiments, J. Mech. Phys. Solids. 109 (2017) 95–116. doi:10.1016/j.jmps.2017.08.008.

[3] Z. Zhang, T.S. Jun, T.B. Britton, F.P.E. Dunne, Intrinsic anisotropy of strain rate sensitivity in single crystal alpha titanium, Acta Mater. 118 (2016) 317–330. doi:10.1016/j.actamat.2016.07.044.

[4] Z. Zhang, T.-S. Jun, T.B. Britton, F.P.E. Dunne, Determination of Ti-6242 α and β slip properties using micro-pillar test and computational crystal plasticity, J. Mech. Phys. Solids. 95 (2016) 393–410. doi:10.1016/j.jmps.2016.06.007.

[5] A.J. Beaudoin, K.K. Mathur, P.R. Dawson, G.C. Johnson, Three-dimensional deformation process simulation with explicit use of polycrystal plasticity models, Int. J. Plast. 9 (1993) 833–860. doi:10.1016/0749-6419(93)90054-T.

[6] S.R. Kalidindi, C.A. Bronkhorst, L. Anand, Crystallographic texture evolution in bulk deformation processing of FCC metals, J. Mech. Phys. Solids. 40 (1992) 537–569. doi:10.1016/0022-5096(92)80003-9.

[7] F. Roters, P. Eisenlohr, L. Hantcherli, D.D. Tjahjanto, T.R. Bieler, D. Raabe, Overview of constitutive laws, kinematics, homogenization and multiscale methods in crystal plasticity finite-element modeling: Theory, experiments, applications, Acta Mater. 58 (2010) 1152–1211. doi:10.1016/j.actamat.2009.10.058.

[8] A.J.B. Jr, H. Mecking, U.F. Kocks, Development of localized orientation gradients in fcc polycrystals, Philos. Mag. A. 73 (1996) 1503–1517. doi:10.1080/01418619608242998.

[9] D.P. Mika, P.R. Dawson, Polycrystal plasticity modeling of intracrystalline boundary textures, Acta Mater. 47 (1999) 1355–1369. doi:10.1016/S1359-6454(98)00386-3.

[10] S. Balasubramanian, L. Anand, Plasticity of initially textured hexagonal polycrystals at high homologous temperatures: application to titanium, Acta Mater. 50 (2002) 133–148. doi:10.1016/S1359-6454(01)00326-3.

[11] A.J. Beaudoin, P.R. Dawson, K.K. Mathur, U.F. Kocks, D.A. Korzekwa, Application of polycrystal plasticity to sheet forming, Comput. Methods Appl. Mech. Eng. 117 (1994) 49–70. doi:10.1016/0045-7825(94)90076-0.

[12] D. Raabe, D. Ma, F. Roters, Effects of initial orientation, sample geometry and friction on anisotropy and crystallographic orientation changes in single crystal microcompression deformation: A crystal plasticity finite element study, Acta Mater. 55 (2007) 4567–4583. doi:10.1016/j.actamat.2007.04.023.

[13] X. You, T. Connolley, P.E. McHugh, H. Cuddy, C. Motz, A combined experimental and computational study of deformation in grains of biomedical grade 316LVM stainless steel, Acta Mater. 54 (2006) 4825–4840. doi:10.1016/j.actamat.2006.06.021.

[14] T. Hama, H. Takuda, Crystal-plasticity finite-element analysis of inelastic behavior during unloading in a magnesium alloy sheet, Int. J. Plast. 27 (2011) 1072–1092. doi:10.1016/j.ijplas.2010.11.004.

[15] B. Klusemann, B. Svendsen, H. Vehoff, Investigation of the deformation behavior of Fe–3%Si sheet metal with large grains via crystal plasticity and finite-element modeling, Comput. Mater. Sci. 52 (2012) 25–32. doi:10.1016/j.commatsci.2011.03.042.

[16] Y.S. Choi, M.A. Groeber, P.A. Shade, T.J. Turner, J.C. Schuren, D.M. Dimiduk, M.D. Uchic, A.D. Rollett, Crystal Plasticity Finite Element Method Simulations for a Polycrystalline Ni Micro-Specimen Deformed in Tension, Metall. Mater. Trans. A. 45 (2014) 6352–6359. doi:10.1007/s11661-014-2556-y.

[17] T. Zhang, J. Jiang, B. Britton, B. Shollock, F. Dunne, Crack nucleation using combined crystal plasticity modelling, high-resolution digital image correlation and high-resolution electron backscatter diffraction in a superalloy containing non-metallic inclusions under fatigue, Proc. R. Soc. A. 472 (2016) 20150792. doi:10.1098/rspa.2015.0792.

[18] S.R. Yeratapally, M.G. Glavicic, M. Hardy, M.D. Sangid, Microstructure based fatigue life prediction framework for polycrystalline nickel-base superalloys with emphasis on the role played by twin boundaries in crack initiation, Acta Mater. 107 (2016) 152–167. doi:10.1016/j.actamat.2016.01.038.

[19] D. Ozturk, A.L. Pilchak, S. Ghosh, Experimentally validated dwell and cyclic fatigue crack nucleation model for α–titanium alloys, Scr. Mater. 127 (2017) 15–18. doi:10.1016/j.scriptamat.2016.08.031.

[20] J.R. Mayeur, D.L. McDowell, R.W. Neu, Crystal plasticity simulations of fretting of Ti-6Al-4V in partial slip regime considering effects of texture, Comput. Mater. Sci. 41 (2008) 356–365. doi:10.1016/j.commatsci.2007.04.020.

[21] T.R. Bieler, P. Eisenlohr, F. Roters, D. Kumar, D.E. Mason, M.A. Crimp, D. Raabe, The role of heterogeneous deformation on damage nucleation at grain boundaries in single phase metals, Int. J. Plast. 25 (2009) 1655–1683. doi:10.1016/j.ijplas.2008.09.002.

[22] M.E. Gurtin, A gradient theory of single-crystal viscoplasticity that accounts for geometrically necessary dislocations, J. Mech. Phys. Solids. 50 (2002) 5–32. doi:10.1016/S0022-5096(01)00104-1.

[23] A. Arsenlis, D. M. Parks, R. Becker, V. V. Bulatov, On the evolution of crystallographic dislocation density in non-homogeneously deforming crystals, J. Mech. Phys. Solids. 52 (2004) 1213–1246. doi:10.1016/j.jmps.2003.12.007.

[24] A. Ma, F. Roters, D. Raabe, A dislocation density based constitutive model for crystal plasticity FEM including geometrically necessary dislocations, Acta Mater. 54 (2006) 2169–2179. doi:10.1016/j.actamat.2006.01.005.

[25] A. Ma, F. Roters, D. Raabe, On the consideration of interactions between dislocations and grain boundaries in crystal plasticity finite element modeling – Theory, experiments, and simulations, Acta Mater. 54 (2006) 2181–2194. doi:10.1016/j.actamat.2006.01.004.

[26] D. Deka, D.S. Joseph, S. Ghosh, M.J. Mills, Crystal plasticity modeling of deformation and creep in polycrystalline Ti-6242, Metall. Mater. Trans. A. 37 (2006) 1371–1388. doi:10.1007/s11661-006-0082-2.

[27] V. Hasija, S. Ghosh, M.J. Mills, D.S. Joseph, Deformation and creep modeling in polycrystalline Ti–6Al alloys, Acta Mater. 51 (2003) 4533–4549. doi:10.1016/S1359-6454(03)00289-1.

[28] M. Shenoy, Y. Tjiptowidjojo, D. McDowell, Microstructure-sensitive modeling of polycrystalline IN 100, Int. J. Plast. 24 (2008) 1694–1730. doi:10.1016/j.ijplas.2008.01.001.

[29] A. Chakraborty, P. Eisenlohr, Evaluation of an inverse methodology for estimating constitutive parameters in face-centered cubic materials from single crystal indentations, Eur. J. Mech. - A/Solids. (n.d.). doi:10.1016/j.euromechsol.2017.06.012.

[30] S. Mandal, B. T. Gockel, A.D. Rollett, Application of canonical correlation analysis to a sensitivity study of constitutive model parameter fitting, Mater. Des. 132 (2017) 30–43. doi:10.1016/j.matdes.2017.06.050.

[31] M. Diehl, M. Groeber, C. Haase, D.A. Molodov, F. Roters, D. Raabe, Identifying Structure–Property Relationships Through DREAM.3D Representative Volume Elements and DAMASK Crystal Plasticity Simulations: An Integrated Computational Materials Engineering Approach, JOM. 69 (2017) 848–855. doi:10.1007/s11837-017-2303-0.

[32] S. Ghosh, Y. Bhandari, M. Groeber, CAD-based reconstruction of 3D polycrystalline alloy microstructures from FIB generated serial sections, CAD Comput. Aided Des. 40 (2008) 293–310. doi:10.1016/j.cad.2007.11.003.

[33] C. Zhang, H. Li, P. Eisenlohr, W. Liu, C.J. Boehlert, M.A. Crimp, T.R. Bieler, Effect of realistic 3D microstructure in crystal plasticity finite element analysis of polycrystalline Ti-5Al-2.5Sn, Int. J. Plast. 69 (2015) 21–35. doi:10.1016/j.ijplas.2015.01.003.

[34] T.J. Turner, P.A. Shade, J. V. Bernier, S.F. Li, J.C. Schuren, P. Kenesei, R.M. Suter, J. Almer, Crystal Plasticity Model Validation Using Combined High-Energy Diffraction Microscopy Data for a Ti-7Al Specimen, Metall. Mater. Trans. A. 48 (2017) 627–647. doi:10.1007/s11661-016-3868-x.

[35] M.P. Echlin, A. Mottura, C.J. Torbet, T.M. Pollock, A new TriBeam system for three-dimensional multimodal materials analysis, Rev. Sci. Instrum. 83 (2012). doi:10.1063/1.3680111.

[36] T.J. Turner, P.A. Shade, J.C. Schuren, M.A. Groeber, The influence of microstructure on surface strain distributions in a nickel micro-tension specimen, Model. Simul. Mater. Sci. Eng. 21 (2013) 15002. doi:10.1088/0965-0393/21/1/015002.

[37] H. Lim, J.D. Carroll, C.C. Battaile, T.E. Buchheit, B.L. Boyce, C.R. Weinberger, Grain-scale experimental validation of crystal plasticity finite element simulations of tantalum oligocrystals, Int. J. Plast. 60 (2014) 1–18. doi:10.1016/j.ijplas.2014.05.004.

[38] C.C. Tasan, J.P.M. Hoefnagels, M. Diehl, D. Yan, F. Roters, D. Raabe, Strain localization and damage in dual phase steels investigated by coupled in-situ deformation experiments and crystal plasticity simulations, Int. J. Plast. 63 (2014) 198–210. doi:10.1016/j.ijplas.2014.06.004.

[39] A.W. Mello, A. Nicolas, R.A. Lebensohn, M.D. Sangid, Effect of microstructure on strain localization in a 7050 aluminum alloy: Comparison of experiments and modeling for various textures, Mater. Sci. Eng. A. 661 (2016) 187–197. doi:10.1016/j.msea.2016.03.012.

[40] L. Margulies, T. Lorentzen, H.F. Poulsen, T. Leffers, Strain tensor development in a single grain in the bulk of a polycrystal under loading, Acta Mater. 50 (2002) 1771–1779. doi:10.1016/S1359-6454(02)00028-9.

[41] J. Oddershede, Sø. Schmidt, H.F. Poulsen, H.O. Srensen, J. Wright, W. Reimers, Determining grain resolved stresses in polycrystalline materials using three-dimensional X-ray diffraction, J. Appl. Crystallogr. 43 (2010) 539–549. doi:10.1107/S0021889810012963.

[42] J. V. Bernier, N.R. Barton, U. Lienert, M.P. Miller, Far-field high-energy diffraction microscopy: A tool for intergranular orientation and strain analysis, J. Strain Anal. Eng. Des. 46 (2011) 527–547. doi:10.1177/0309324711405761.

[43] J.C. Schuren, P.A. Shade, J. V. Bernier, S.F. Li, B. Blank, J. Lind, P. Kenesei, U. Lienert, R.M. Suter, T.J. Turner, D.M. Dimiduk, J. Almer, New opportunities for quantitative tracking of polycrystal responses in three dimensions, Curr. Opin. Solid State Mater. Sci. 19 (2015) 235–244. doi:10.1016/j.cossms.2014.11.003.

[44] R. Pokharel, J. Lind, A.K. Kanjarla, R.A. Lebensohn, S.F. Li, P. Kenesei, R.M. Suter, A.D. Rollett, Polycrystal Plasticity: Comparison Between Grain - Scale Observations of Deformation and Simulations, Annu. Rev. Condens. Matter Phys. 5 (2014) 317–346. doi:10.1146/annurev-conmatphys-031113-133846.

[45] J.R. Mayeur, D.L. McDowell, A three-dimensional crystal plasticity model for duplex Ti–6Al–4V, Int. J. Plast. 23 (2007) 1457–1485. doi:10.1016/j.ijplas.2006.11.006.

[46] M. Zhang, J. Zhang, D.L. McDowell, Microstructure-based crystal plasticity modeling of cyclic deformation of Ti–6Al–4V, Int. J. Plast. 23 (2007) 1328–1348. doi:10.1016/j.ijplas.2006.11.009.

[47] F. Bridier, D.L. McDowell, P. Villechaise, J. Mendez, Crystal plasticity modeling of slip activity in Ti–6Al–4V under high cycle fatigue loading, Int. J. Plast. 25 (2009) 1066–1082. doi:10.1016/j.ijplas.2008.08.004.

[48] G. Proust, C.N. Tomé, A. Jain, S.R. Agnew, Modeling the effect of twinning and detwinning during strain-path changes of magnesium alloy AZ31, Int. J. Plast. 25 (2009) 861–880. doi:https://doi.org/10.1016/j.ijplas.2008.05.005.

[49] A.L. Oppedal, H. El Kadiri, C.N. Tomé, S.C. Vogel, M.F. Horstemeyer, Anisotropy in hexagonal close-packed structures: improvements to crystal plasticity approaches applied to magnesium alloy, Philos. Mag. 93 (2013) 4311–4330. doi:10.1080/14786435.2013.827802.

[50] V. Prithivirajan, Sangid, The role of defects and critical pore size analysis in the fatigue response of additively manufactured IN718 via crystal plasticity PV, Mater. Des. 150 (2018) 139–153. https://doi.org/10.1016/j.matdes.2018.04.022.

[51] Z. Zheng, D.S. Balint, F.P.E. Dunne, Dwell fatigue in two Ti alloys: An integrated crystal plasticity and discrete dislocation study, J. Mech. Phys. Solids. 96 (2016) 411–427. doi:https://doi.org/10.1016/j.jmps.2016.08.008.

[52] R. Bandyopadhyay, V. Prithivirajan, M.D. Sangid, Uncertainty Quantification in the Mechanical Response of Crystal Plasticity Simulations, JOM. (2019). doi:10.1007/s11837-019-03551-3.

[53] P. Darbandi, T.R. Bieler, F. Pourboghrat, T. Lee, Crystal Plasticity Finite-Element Analysis of Deformation Behavior in Multiple-Grained Lead-Free Solder Joints, J. Electron. Mater. 42 (2013) 201–214. doi:10.1007/s11664-012-2339-4.

[54] M.P. Miller, J. V Bernier, J.-S. Park, A. Kazimirov, Experimental measurement of lattice strain pole figures using synchrotron x rays, Rev. Sci. Instrum. 76 (2005) 113903. doi:10.1063/1.2130668.

[55] J. Almer, U. Lienert, R.L. Peng, C. Schlauer, M. Odén, Strain and texture analysis of coatings using high-energy x-rays, J. Appl. Phys. 94 (2003) 697–702. doi:10.1063/1.1582351.

[56] A. Buljac, M. Shakoor, J. Neggers, M. Bernacki, P.-O. Bouchard, L. Helfen, T.F. Morgeneyer, F. Hild, Numerical validation framework for micromechanical simulations based on synchrotron 3D imaging, Comput. Mech. 59 (2017) 419–441. doi:10.1007/s00466-016-1357-0.

[57] C.-H. Goh, R.W. Neu, D.L. McDowell, Crystallographic plasticity in fretting of Ti–6AL–4V, Int. J. Plast. 19 (2003) 1627–1650. doi:10.1016/S0749-6419(02)00039-6.

[58] F.P.E. Dunne, D. Rugg, A. Walker, Lengthscale-dependent, elastically anisotropic, physically-based hcp crystal plasticity: Application to cold-dwell fatigue in Ti alloys, Int. J. Plast. 23 (2007) 1061–1083. doi:10.1016/j.ijplas.2006.10.013.

[59] M. Kasemer, R. Quey, P. Dawson, The influence of mechanical constraints introduced by β annealed microstructures on the yield strength and ductility of Ti-6Al-4V, J. Mech. Phys. Solids. 103 (2017) 179–198. doi:10.1016/j.jmps.2017.03.013.

[60] Z. Zhang, F.P.E. Dunne, Microstructural heterogeneity in rate-dependent plasticity of multiphase titanium alloys, J. Mech. Phys. Solids. 103 (2017) 199–220. doi:10.1016/j.jmps.2017.03.012.

[61] T. Ozturk, A.D. Rollett, Effect of microstructure on the elasto-viscoplastic deformation of dual phase titanium structures, Comput. Mech. (2017) 1–16. doi:10.1007/s00466-017-1467-3.

[62] J.A. Moore, N.R. Barton, J. Florando, R. Mulay, M. Kumar, Crystal plasticity modeling of β phase deformation in Ti-6Al-4V, Model. Simul. Mater. Sci. Eng. 25 (2017) 75007. doi:10.1088/1361-651X/aa841c.

[63] L. Thijs, F. Verhaeghe, T. Craeghs, J. Van Humbeeck, J.-P. Kruth, A study of the microstructural evolution during selective laser melting of Ti–6Al–4V, Acta Mater. 58 (2010) 3303–3312. doi:10.1016/j.actamat.2010.02.004.

[64] H. Mughrabi, Dislocation wall and cell structures and long-range internal stresses in deformed metal crystals, Acta Metall. 31 (1983) 1367–1379. doi:10.1016/0001-6160(83)90007-X.

[65] S.R. Agnew, C.N. Tomé, D.W. Brown, T.M. Holden, S.C. Vogel, Study of slip mechanisms in a magnesium alloy by neutron diffraction and modeling, Scr. Mater. 48 (2003) 1003–1008. doi:10.1016/S1359-6462(02)00591-2.

[66] F. Soul, N. Hamdy, Numerical Simulation of Residual Stress and Strain Behavior After Temperature Modification, in: Weld. Process., 2012. doi:10.5772/47745.

[67] R.R. Pawar, V.T. Deshpande, The anisotropy of the thermal expansion of α-titanium, Acta Crystallogr. Sect. A. 24 (1968) 316–317. doi:10.1107/S0567739468000525.

[68] P.A. Turner, C.N. Tomé, A study of residual stresses in Zircaloy-2 with rod texture, Acta Metall. Mater. 42 (1994) 4143–4153. doi:10.1016/0956-7151(94)90191-0.

[69] W.D. Musinski, D.L. McDowell, On the eigenstrain application of shot-peened residual stresses within a crystal plasticity framework: Application to Ni-base superalloy specimens, Int. J. Mech. Sci. 100 (2015) 195–208. doi:10.1016/j.ijmecsci.2015.06.020.

[70] K.P. McNelis, P.R. Dawson, M.P. Miller, A two-scale methodology for determining the residual stresses in polycrystalline solids using high energy X-ray diffraction data, J. Mech. Phys. Solids. 61 (2013) 428–449. doi:10.1016/j.jmps.2012.09.015.

[71] R. Pokharel, R.A. Lebensohn, Instantiation of crystal plasticity simulations for micromechanical modelling with direct input from microstructural data collected at light sources, Scr. Mater. 132 (2017) 73–77. doi:10.1016/j.scriptamat.2017.01.025.

[72] M. Peach, J.S. Koehler, The Forces Exerted on Dislocations and the Stress Fields Produced by Them, Phys. Rev. 80 (1950) 436–439.

[73] M.E. Kassner, P. Geantil, L.E. Levine, Long range internal stresses in single-phase crystalline materials, Int. J. Plast. 45 (2013) 44–60. doi:10.1016/j.ijplas.2012.10.003.

[74] M.F. Ashby, The deformation of plastically non-homogeneous materials, Philos. Mag. A J. Theor. Exp. Appl. Phys. 21 (1970) 399–424. doi:10.1080/14786437008238426.

[75] K. Chatterjee, J.Y.P. Ko, J.T. Weiss, H.T. Philipp, J. Becker, P. Purohit, S.M. Gruner, A.J. Beaudoin, Study of residual stresses in Ti-7Al using theory and experiments, J. Mech. Phys. Solids. 109 (2017) 95–116. doi:10.1016/j.jmps.2017.08.008.

[76] T. Ben Britton, S. Birosca, M. Preuss, A.J. Wilkinson, Electron backscatter diffraction study of dislocation content of a macrozone in hot-rolled Ti–6Al–4V alloy, Scr. Mater. 62 (2010) 639–642. doi:10.1016/j.scriptamat.2010.01.010.

[77] S.L. Semiatin, T.R. Bieler, Effect of texture and slip mode on the anisotropy of plastic flow and flow softening during hot working of Ti-6Al-4V, Metall. Mater. Trans. A. 32 (2001) 1787–1799. doi:10.1007/s11661-001-0155-1.

[78] G. Welsch, W. Bunk, Deformation Modes of the Alpha-Phase of Ti–6AL–4V as a Function of Oxygen Concentration and Aging Temperature, Metall. Mater. Trans. A. 13 (1982) 889–899. doi:10.1007/BF02642403.

[79] G. Welsch, Y.-T. Lee, P.C. Eloff, D. Eylon, F.H. Froes, Deformation behavior of blended elemental ti-6ai-4v compacts, Metall. Trans. A. 14 (1983) 761–769. doi:10.1007/BF02643793.

[80] K. Le Biavant, S. Pommier, C. Prioul, Local texture and fatigue crack initiation in a Ti-6Al-4V titanium alloy, Fatigue Fract. Eng. Mater. Struct. 25 (2002) 527–545. doi:10.1046/j.1460-2695.2002.00480.x.

[81] M. Humbert, L. Germain, N. Gey, P. Bocher, M. Jahazi, Study of the variant selection in sharp textured regions of bimodal IMI 834 billet, Mater. Sci. Eng. A. 430 (2006) 157–164. doi:10.1016/j.msea.2006.05.047.

[82] E. Uta, N. Gey, P. Bocher, M. Humbert, J. Gilgert, Texture heterogeneities in αp/αstitanium forging analysed by EBSD-Relation to fatigue crack propagation, J. Microsc. 233 (2009) 451–459. doi:10.1111/j.1365-2818.2009.03141.x.

[83] F. Bridier, P. Villechaise, J. Mendez, Slip and fatigue crack formation processes in an ??/?? titanium alloy in relation to crystallographic texture on different scales, Acta Mater. 56 (2008) 3951–3962. doi:10.1016/j.actamat.2008.04.036.

[84] I. Bantounas, D. Dye, T.C. Lindley, The role of microtexture on the faceted fracture morphology in Ti–6Al–4V subjected to high-cycle fatigue, Acta Mater. 58 (2010) 3908–3918. doi:https://doi.org/10.1016/j.actamat.2010.03.036.

[85] M.P. Echlin, J.C. Stinville, V.M. Miller, W.C. Lenthe, T.M. Pollock, Incipient slip and long range plastic strain localization in microtextured Ti-6Al-4V titanium, Acta Mater. 114 (2016) 164–175. doi:https://doi.org/10.1016/j.actamat.2016.04.057.

[86] R. Bandyopadhyay, A.W. Mello, K. Kapoor, M.P. Reinhold, T.F. Broderick, M.D. Sangid, On the crack initiation and heterogeneous deformation of Ti-6Al-4V during high cycle fatigue at high R ratios, J. Mech. Phys. Solids. 129 (2019) 61–82. doi:https://doi.org/10.1016/j.jmps.2019.04.017.

[87] T.A. Book, M.D. Sangid, Strain localization in Ti-6Al-4V Widmanstätten microstructures produced by additive manufacturing, Mater. Charact. 122 (2016) 104–112. doi:10.1016/j.matchar.2016.10.018.

[88] K. Kapoor, M.D. Sangid, Initializing type-2 residual stresses in crystal plasticity finite element simulations utilizing high-energy diffraction microscopy data, Mater. Sci. Eng. A. 729 (2018) 53–63. doi:10.1016/j.msea.2018.05.031.

[89] K. Kapoor, Y.S.J. Yoo, T.A. Book, J.P. Kacher, M.D. Sangid, Incorporating grain-level residual stresses and validating a crystal plasticity model of a two-phase Ti-6Al-4 V alloy produced via additive manufacturing, J. Mech. Phys. Solids. 121 (2018) 447–462. doi:https://doi.org/10.1016/j.jmps.2018.07.025.

[90] M.A. Cuddihy, A. Stapleton, S. Williams, F.P.E. Dunne, On cold dwell facet fatigue in titanium alloy aero-engine components, Int. J. Fatigue. 97 (2017) 177–189. doi:https://doi.org/10.1016/j.ijfatigue.2016.11.034.

[91] A.A. Salem, J.B. Shaffer, R.A. Kublik, L.A. Wuertemberger, D.P. Satko, Microstructure-Informed Cloud Computing for Interoperability of Materials Databases and Computational Models: Microtextured Regions in Ti Alloys, Integr. Mater. Manuf. Innov. 6 (2017) 111–126. doi:10.1007/s40192-017-0090-7.

[92] A.L. Pilchak, J. Li, S.I. Rokhlin, Quantitative Comparison of Microtexture in Near-Alpha Titanium Measured by Ultrasonic Scattering and Electron Backscatter Diffraction, Metall. Mater. Trans. A. 45 (2014) 4679–4697. doi:10.1007/s11661-014-2367-1.

[93] A.L. Pilchak, J. Shank, J.C. Tucker, S. Srivatsa, P.N. Fagin, S.L. Semiatin, A dataset for the development, verification, and validation of microstructure-sensitive process models for near-alpha titanium alloys, Integr. Mater. Manuf. Innov. 5 (2016) 14. doi:10.1186/s40192-016-0056-1.

[94] B. Woodfield, A. P., Gorman, M. D., Corderman, R. R., Sutliff, J. A., Yamron, Effect of Microstructure on Dwell fatigue Behavior of Ti-6242, in: Titan. '95 Sci. Technol., 1995.

[95] T.J. Turner, P.A. Shade, J. V. Bernier, S.F. Li, J.C. Schuren, J. Lind, U. Lienert, P. Kenesei, R.M. Suter, B. Blank, J. Almer, Combined near- and far-field high-energy diffraction microscopy dataset for Ti-7Al tensile specimen elastically loaded in situ, Integr. Mater. Manuf. Innov. 5 (2016) 5. doi:10.1186/s40192-016-0048-1.

[96] T.B. Britton, F.P.E. Dunne, A.J. Wilkinson, On the mechanistic basis of deformation at the microscale in hexagonal close-packed metals, Proc. R. Soc. A. 471 (2015) 20140881. doi:10.1098/rspa.2014.0881.

[97] S. Suri, G.B. Viswanathan, T. Neeraj, D.-H. Hou, M.J. Mills, Room temperature deformation and mechanisms of slip transmission in oriented single-colony crystals of an α/β titanium alloy, Acta Mater. 47 (1999) 1019–1034. doi:10.1016/S1359-6454(98)00364-4.

[98] K.S. Chan, A micromechanical analysis of the yielding behavior of individual widmanst{ä}tten colonies of an $α$ + $β$ titanium alloy, Metall. Mater. Trans. A. 35 (2004) 3409–3422. doi:10.1007/s11661-004-0177-6.

[99] P.J. Ashton, T.-S. Jun, Z. Zhang, T.B. Britton, A.M. Harte, S.B. Leen, F.P.E. Dunne, The effect of the beta phase on the micromechanical response of dual-phase titanium alloys, Int. J. Fatigue. 100 (2017) 377–387. doi:https://doi.org/10.1016/j.ijfatigue.2017.03.020.

[100] S. Waheed, Z. Zheng, D.S. Balint, F.P.E. Dunne, Microstructural effects on strain rate and dwell sensitivity in dual-phase titanium alloys, Acta Mater. 162 (2019) 136–148. doi:https://doi.org/10.1016/j.actamat.2018.09.035.

[101] R.M. Suter, D. Hennessy, C. Xiao, U. Lienert, Forward modeling method for microstructure reconstruction using x-ray diffraction microscopy: Single-crystal verification, Rev. Sci. Instrum. 77 (2006). doi:10.1063/1.2400017.

[102] S.F. Li, R.M. Suter, Adaptive reconstruction method for three-dimensional orientation imaging, J. Appl. Crystallogr. 46 (2013) 512–524. doi:10.1107/S0021889813005268.

[103] J. Cheng, A. Shahba, S. Ghosh, Stabilized tetrahedral elements for crystal plasticity finite element analysis overcoming volumetric locking, Comput. Mech. 57 (2016) 733–753. doi:10.1007/s00466-016-1258-2.

[104] J.W. Hutchinson, Creep and plasticity of hexagonal polycrystals as related to single crystal slip, Metall. Trans. A. 8 (1977) 1465–1469. doi:10.1007/BF02642860.

[105] R.J. Asaro, A. Needleman, Overview no. 42 Texture development and strain hardening in rate dependent polycrystals, Acta Metall. 33 (1985) 923–953. doi:10.1016/0001-6160(85)90188-9.

[106] C.O. Frederick, P.J. Armstrong, A mathematical representation of the multiaxial Bauschinger effect, Mater. HIGH Temp. 24 (2007) 1–26.

[107] S. Suri, G.B. Viswanathan, T. Neeraj, D.H. Hou, M.J. Mills, Room temperature deformation and mechanisms of slip transmission in oriented single-colony crystals of an α/β titanium alloy, Acta Mater. 47 (1999) 1019–1034. doi:10.1016/S1359-6454(98)00364-4.

[108] J.C. Williams, R.G. Baggerly, N.E. Paton, Deformation behavior of HCP Ti-Al alloy single crystals, Metall. Mater. Trans. A. 33 (2002) 837–850. doi:10.1007/s11661-002-0153-y.

[109] E.S. Fisher, C.J. Renken, Single-Crystal Elastic Moduli and the hcp \ensuremath{\rightarrow} bcc Transformation in Ti, Zr, and Hf, Phys. Rev. 135 (1964) A482–A494. doi:10.1103/PhysRev.135.A482.

[110] T.-S. Jun, D.E.J. Armstrong, T.B. Britton, A nanoindentation investigation of local strain rate sensitivity in dual-phase Ti alloys, J. Alloys Compd. 672 (2016) 282–291. doi:10.1016/j.jallcom.2016.02.146.

[111] A.D. Kammers, S. Daly, Self-Assembled Nanoparticle Surface Patterning for Improved Digital Image Correlation in a Scanning Electron Microscope, Exp. Mech. 53 (2013) 1333–1341. doi:10.1007/s11340-013-9734-5.

[112] J. Esquivel, M.D. Sangid, Digital Image Correlation of Heterogeneous Deformation in Polycrystalline Material with Electron Backscatter Diffraction, Microsc. Microanal. 21 (2015) 1167–1168. doi:10.1017/S1431927615006625.

[113] A.W. Mello, T.A. Book, A. Nicolas, S.E. Otto, C.J. Gilpin, M.D. Sangid, Distortion Correction Protocol for Digital Image Correlation after Scanning Electron Microscopy: Emphasis on Long Duration and Ex-Situ Experiments, Exp. Mech. (2017) 1–15. doi:10.1007/s11340-017-0303-1.

[114] E.O. Hall, The Deformation and Ageing of Mild Steel: III Discussion of Results, Proc. Phys. Soc. Sect. B. 64 (1951) 747. doi:10.1088/0370-1301/64/9/303.

[115] N.J. Petch, The cleavage strength of polycrystals, J. Iron Steel InstInst. 174 (1953) 25–28. doi:10.1007/BF01972547.

[116] J. V. Bernier, J.-S. Park, A.L. Pilchak, M.G. Glavicic, M.P. Miller, Measuring Stress Distributions in Ti-6Al-4V Using Synchrotron X-Ray Diffraction, Metall. Mater. Trans. A. 39 (2008) 3120–3133. doi:10.1007/s11661-008-9639-6.

[117] F.P.E. Dunne, R. Kiwanuka, A.J. Wilkinson, Crystal plasticity analysis of micro-deformation, lattice rotation and geometrically necessary dislocation density, Proc. R. Soc. A. (2012) rspa20120050. doi:10.1098/rspa.2012.0050.

[118] A. Arsenlis, D.M. Parks, Crystallographic aspects of geometrically-necessary and statistically-stored dislocation density, Acta Mater. 47 (1999) 1597–1611. doi:10.1016/S1359-6454(99)00020-8.

[119] W. Pantleon, Resolving the geometrically necessary dislocation content by conventional electron backscattering diffraction, Scr. Mater. 58 (2008) 994–997. doi:10.1016/j.scriptamat.2008.01.050.

[120] M. Calcagnotto, D. Ponge, E. Demir, D. Raabe, Orientation gradients and geometrically necessary dislocations in ultrafine grained dual-phase steels studied by 2D and 3D EBSD, Mater. Sci. Eng. A. 527 (2010) 2738–2746. doi:10.1016/j.msea.2010.01.004.

[121] T.J. Ruggles, D.T. Fullwood, Estimations of bulk geometrically necessary dislocation density using high resolution EBSD, Ultramicroscopy. 133 (2013) 8–15. doi:10.1016/j.ultramic.2013.04.011.

[122] B. Adams, J. Kacher, EBSD-Based Microscopy: Resolution of Dislocation Density, Comput. Mater. Contin. 14 (2009) 185. https://www.researchgate.net/profile/Josh_Kacher/publication/259115939_EBSD-Based_Microscopy_Resolution_of_Dislocation_Density/links/00b7d53306c10ba6d1000000/EBSD-Based-Microscopy-Resolution-of-Dislocation-Density.pdf.

[123] M.A. Groeber, M.A. Jackson, DREAM.3D: A Digital Representation Environment for the Analysis of Microstructure in 3D, Integr. Mater. Manuf. Innov. 3 (2014) 5. doi:10.1186/2193-9772-3-5.

[124] W.G. Burgers, On the process of transition of the cubic-body-centered modification into the hexagonal-close-packed modification of zirconium, Physica. 1 (1934) 561–586. doi:10.1016/S0031-8914(34)80244-3.

[125] Z. Zhang, M.A. Cuddihy, F.P.E. Dunne, On rate-dependent polycrystal deformation: the temperature sensitivity of cold dwell fatigue, Proc. R. Soc. A. 471 (2015) 20150214. doi:10.1098/rspa.2015.0214.

[126] V.V.C. Wan, J. Jiang, D.W. MacLachlan, F.P.E. Dunne, Microstructure-sensitive fatigue crack nucleation in a polycrystalline Ni superalloy, Int. J. Fatigue. 90 (2016) 181–190. doi:10.1016/j.ijfatigue.2016.04.013.

[127] L. Li, L. Shen, G. Proust, A texture-based representative volume element crystal plasticity model for predicting Bauschinger effect during cyclic loading, Mater. Sci. Eng. A. 608 (2014) 174–183. doi:10.1016/j.msea.2014.04.067.

[128] S. Sinha, S. Ghosh, Modeling cyclic ratcheting based fatigue life of HSLA steels using crystal plasticity FEM simulations and experiments, Int. J. Fatigue. 28 (2006) 1690–1704. doi:10.1016/j.ijfatigue.2006.01.008.

[129] A. Guery, F. Hild, F. Latourte, S. Roux, Slip activities in polycrystals determined by coupling DIC measurements with crystal plasticity calculations, Int. J. Plast. 81 (2016) 249–266. doi:10.1016/j.ijplas.2016.01.008.

[130] P.D. Littlewood, A.J. Wilkinson, Geometrically necessary dislocation density distributions in cyclically deformed Ti-6Al-4V, Acta Mater. 60 (2012) 5516–5525. doi:10.1016/j.actamat.2012.07.003.

[131] J. Jiang, T. Benjamin Britton, A.J. Wilkinson, Evolution of intragranular stresses and dislocation densities during cyclic deformation of polycrystalline copper, Acta Mater. 94 (2015) 193–204. doi:10.1016/j.actamat.2015.04.031.

[132] M.H. Yoo, S.R. Agnew, J.R. Morris, K.M. Ho, Non-basal slip systems in HCP metals and alloys: Source mechanisms, Mater. Sci. Eng. A. 319–321 (2001) 87–92. doi:10.1016/S0921-5093(01)01027-9.

[133] M.D. Sangid, The physics of fatigue crack initiation, Int. J. Fatigue. 57 (2013) 58–72. doi:10.1016/j.ijfatigue.2012.10.009.

[134] S.D. Antolovich, R.W. Armstrong, Plastic strain localization in metals: origins and consequences, Prog. Mater. Sci. 59 (2014) 1–160. doi:10.1016/j.pmatsci.2013.06.001.

[135] A.M. Korsunsky, K.E. James, M.R. Daymond, Intergranular stresses in polycrystalline fatigue: diffraction measurement and self-consistent modelling, Eng. Fract. Mech. 71 (2004) 805–812. doi:https://doi.org/10.1016/S0013-7944(03)00018-3.

[136] M.D. Sangid, T.A. Book, D. Naragani, J. Rotella, P. Ravi, A. Finch, P. Kenesei, J.-S. Park, H. Sharma, J. Almer, X. Xiao, Role of heat treatment and build orientation in the microstructure sensitive deformation characteristics of IN718 produced via SLM additive manufacturing, Addit. Manuf. 22 (2018) 479–496. doi:https://doi.org/10.1016/j.addma.2018.04.032.

[137] Ritwik Bandyopadhyay, V. Prithivirajan, M.D. Sangid, Uncertainty quantification in the mechanical response of crystal plasticity simulations, Submitted. (n.d.).

[138] P. Dawson, D. Boyce, S. MacEwen, R. Rogge, Residual strains in HY100 polycrystals: Comparisons of experiments and simulations, Metall. Mater. Trans. A. 31 (2000) 1543–1555. doi:10.1007/s11661-000-0165-4.

[139] V. Venkatesh, S. Tamirisa, J. Sartkulvanich, K. Calvert, I. Dempster, V. Saraf, A.A. Salem, S. Rokhlin, T. Broderick, M.G. Glavicic, T. Morton, R. Shankar, A. Pilchak, Icme of Microtexture Evolution in Dual Phase Titanium Alloys, in: Proc. 13th World Conf. Titan., John Wiley & Sons, Ltd, 2016: pp. 1907–1912. doi:10.1002/9781119296126.ch319.

[140] Abaqus Documentation, 2017.

[141] N.P. Fionn Dunne, Introduction to Computational Plasticity, Oxford University Press, 2005.

[142] J.J. Kearns, Thermal expansion and preferred orientation in Zircaloy (LWBR Development Program)e, (1965).

[143] F.P.E. Dunne, A. Walker, D. Rugg, A systematic study of hcp crystal orientation and morphology effects in polycrystal deformation and fatigue, Proc. R. Soc. A Math. Phys. Eng. Sci. 463 (2007) 1467–1489. doi:10.1098/rspa.2007.1833.

[144] K. Zhang, K. V Yang, A. Huang, X. Wu, C.H.J. Davies, Fatigue crack initiation in as forged Ti–6Al–4V bars with macrozones present, Int. J. Fatigue. 80 (2015) 288–297. doi:https://doi.org/10.1016/j.ijfatigue.2015.05.020.

[145] Z. Zheng, D.S. Balint, F.P.E. Dunne, Discrete dislocation and crystal plasticity analyses of load shedding in polycrystalline titanium alloys, Int. J. Plast. 87 (2016) 15–31. doi:https://doi.org/10.1016/j.ijplas.2016.08.009.

[146] K. Chatterjee, A. Venkataraman, T. Garbaciak, J. Rotella, M.D. Sangid, A.J. Beaudoin, P. Kenesei, J.S. Park, A.L. Pilchak, Study of grain-level deformation and residual stresses in Ti-7Al under combined bending and tension using high energy diffraction microscopy (HEDM), Int. J. Solids Struct. 94–95 (2015) 35–49. doi:10.1016/j.ijsolstr.2016.05.010.

PUBLICATIONS

Kartik Kapoor, Michael D. Sangid, Initializing type-2 residual stresses in crystal plasticity finite element simulations utilizing high-energy diffraction microscopy data, Materials Science and Engineering: A, Volume 729, 2018, Pages 53-63

Kartik Kapoor, Yung Suk Jeremy Yoo, Todd A. Book, Josh P. Kacher, Michael D. Sangid, Incorporating grain-level residual stresses and validating a crystal plasticity model of a two-phase Ti-6Al-4V alloy produced via additive manufacturing, Journal of the Mechanics and Physics of Solids, Volume 121, 2018, Pages 447-462,

Kartik Kapoor, Ryan Noraas, Vasisht Venkatesh, Michael D. Sangid, Modeling strain localization in microtextured regions in a Titanium alloy: Ti-6Al-4V (Submitted)

Kartik Kapoor, Priya Ravi, Ryan Noraas, Jun-Sang Park, Vasisht Venkatesh, Jonathan D. Almer, Michael D. Sangid, Modeling Ti-6Al-4V using a crystal plasticity model, calibrated with multi-scale experiments to understand the effect of the orientation and morphology of the α and β phases on time dependent cyclic loading (In preparation)